IONIC POLYMER-METAL COMPOSITE (IPMC) SENSORS

by

Mohammad Gudarzi

BSc, Amirkabir University of Technology, 2009

MSc, Sharif University of Technology, 2011

Submitted to the Graduate Faculty of

Swanson School of Engineering in partial fulfillment

of the requirements for the degree of

Doctor of Philosophy

University of Pittsburgh

2018

UNIVERSITY OF PITTSBURGH

SWANSON SCHOOL OF ENGINEERING

This dissertation was presented

by

Mohammad Gudarzi

It was defended on

June 28, 2018

and approved by

William Slaughter, Ph.D., Associate Professor

Department of Mechanical Engineering and Materials Science

Guangyong Li, Ph.D., Associate Professor

Department of Electrical and Computer Engineering

Dissertation Co-Advisor: Qing-Ming Wang, PhD., Professor

Department of Mechanical Engineering and Materials Science

Dissertation Co-Advisor: Patrick Smolinski, Ph.D., Associate Professor

Department of Mechanical Engineering and Materials Science

IONIC POLYMER-METAL COMPOSITE (IPMC) SENSORS

Mohammad Gudarzi, PhD

University of Pittsburgh, 2018

Ionic polymer-metal composites (IPMCs) which are fabricated from an ionomeric membrane, infused with mobile counterions and sandwiched between two thin noble metal electrodes, offer an outstanding capability to transform electrical energy into mechanical energy and vice versa which makes them an appropriate candidate for actuators and sensors. The purpose of this dissertation is to characterize and model IPMCs in sensory mode, develop a new fabrication procedure to improve their flexibility and humidity dependence and take advantage of IPMCs' exceptional properties in the fabrication of several biomedical instruments to measure some physiological signals such as plantar pressure distribution, blood pulse and tactile forces. For this aim, some IPMC dynamic pressure sensors in bending, compression and shear modes of deformation are designed based on streaming potential hypothesis, fabricated utilizing direct assembly process (DAP) and calibrated in a standard shock pressure tube which provides a broad evaluation of the linearity, sensitivity and reliability of IPMC sensors. Also, to develop a reliable model of applicable sensors that could be used for real-time purposes, three explicit, dynamic, physics-based, rational transfer functions are derived by solving IPMC governing partial differential equation (PDE) in Laplace domain for compression, shear and bending modes. Derived models not only have terms of fundamental material parameters and sensor dimensions but also offer simplicity. Next, to resolve the fragility of electrodes and strong humidity dependence, IPMCs with highly flexible electrodes using sputtered gold thin film and coated with a waterproof acrylic material are fabricated. Conducting some experiments over a period of time shows the improved reliability evidently. In order to develop a self-powered flexible insole, eight circular IPMC pressure sensors are fabricated and fixed on the measuring insole at some specific anatomic areas. The fabricated smart insole is utilized for the real-time plantar pressure distribution analysis of a subject during static stance and gait cycle during walking and running. Produced colormaps

based on measured signals are realistic and show a good agreement with those from commercial smart insoles. Finally, IPMCs are developed for monitoring blood pulse wave and as a flexible touch sensor and recorded signals are discussed.

TABLE OF CONTENTS

LIST OF TABLES

LIST OF FIGURES

PREFACE

I would like to express my sincere appreciation to my advisors, Professors Qing-Ming Wang and Patrick Smolinski for their support and guidance through the course of my graduate studies. I would like to thank the members of my doctoral committee, Professors William Slaughter and Guangyong Li.

I am indebted to my colleagues and friends whom I had the pleasure to work with at one point or another during my time at the University of Pittsburgh: Dr. Hongfei Zu, Dr. Huiyan Wu, Mr. Rongjie Liang, Ms. Qiuyan Li, Mr. Saleh Alghamdi, Ms. Zhimin Sun, Mr. Pei Yuan Hsiao. My deepest gratitude goes to my parents Hossein and Soraya; for their love and support. I dedicate this thesis to them.

1.0 INTRODUCTION

This chapter addresses fundamental properties and sensing and actuation mechanisms of ionic polymer-metal composite (IPMC) materials as well as historical background and chronological development of these materials according to published literature. Latterly, research objectives which emphasize the significance of this PhD research are delineated.

1.1 FUNDAMENTALS

All polymers offer some common inherent properties such as mechanical flexibility, light weight and easy processing. Furthermore, some polymers, which are called electroactive polymers (EAPs), exhibit huge property changes in response to electrical stimulation which significantly improves their intrinsic benefits for potential applications. EAPs' mechanical response to electrical stimulation leads to significant shape and size change. EAPs are mainly classified into two major categories based on the activation mechanism: field-activated or electronic EAPs and ionic EAPs. Electronic polymers require large activation voltage but are well controlled. Electronic EAPs which include electrostrictive, electrostatic, piezoelectric and ferroelectric materials are driven by Coulomb forces. Usually this type of EAPs has a greater mechanical energy density and can be made to hold the induced deformation while activated under DC supply. On the other hand, ionic EAPs which consist of two electrode layers and electrolyte involve mobility or diffusion of ions.

A relatively low voltage can activate ionic EAP and generally leads to bending deformation but it is difficult to maintain a constant position. As actuators, they are characterized by being able to undergo a large amount of deformation when they are stimulated. Similarly, when they exhibit the inverse effect, they can be used as sensors. Ionic polymer gels, ionic polymer-metal composites, conductive polymers and carbon nanotubes are some of the examples of ionic EAPs [1].

Ionic polymer-metal composites (IPMCs), sometimes referred to as soft actuators-sensors or artificial muscles, are an important class of EAPs with natural actuation and sensing abilities. A typical IPMC consists of a polyelectrolyte membrane (usually Nafion® or Flemion®) plated on both faces by a noble metal and is neutralized with certain counter-ions that balance the electrical charge of the anions covalently fixed to the back-bone membrane. Transport of hydrated cations within an IPMC segment under the applied voltage and associated electrostatic interactions lead to bending of it, Figure 1.1. When an IPMC in the solvated (i.e., hydrated) state is stimulated with a suddenly applied voltage, both the fixed anions and mobile counter-ions are subjected to an electric field, but the counter-ions are able to diffuse toward one of the electrodes. Consequently, the composite experiences an initial fast bending deformation followed by a slow relaxation. This relaxation could be either in the same or in the opposite direction of initial bending, depending on the composition of the backbone ionomers and the nature of the counter-ion. The magnitude and speed of the initial fast deflection also depend on the same factors, as well as on the structure of the electrodes and the time-variation of the imposed voltage. IPMCs that are made from Nafion and are neutralized with alkali metals or with alkylammonium cations, regularly first bend towards the anode under a step direct current (DC), and then relax towards the cathode, while the applied voltage is being maintained, often moving beyond their starting position. In this case, the motion towards the anode can be eliminated by slowly increasing the applied voltage at a suitable rate.

Conversely, both initial fast bending and the subsequent relaxation are towards the anode in Flemion-based IPMCs and for all counter-ions that are being utilized. When an IPMC membrane is suddenly bent, a small voltage of the order of millivolts is produced across its faces. Therefore, IPMCs can serve as both soft actuators and sensors.

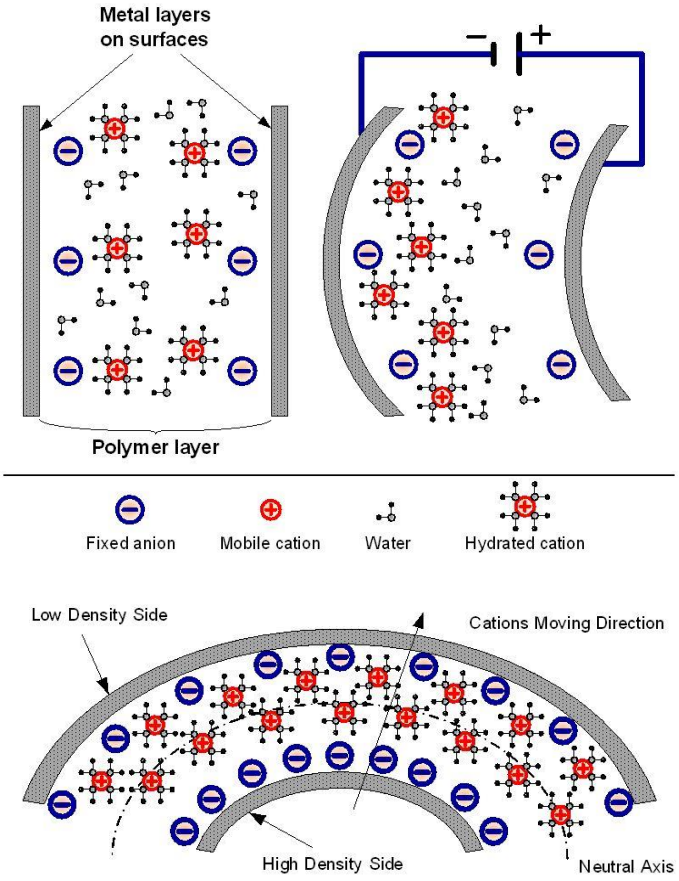

Figure 1.1. Operating principle of IPMCs as (a) actuator and (b) sensor [2]

IPMC materials, due to lack of moving parts and working with modest operating voltages for actuation, may offer advantages over conventional mechanical, hydraulic or pneumatic actuators in certain applications. Recent investigations into the mechanism of IPMC actuation and sensing have led to development of actuators that generate greater displacement magnitudes and forces, and sensors that are more sensitive to imposed deformations. And, researchers seek to

exploit these materials in a number of applications including medical, space, robotic, soft microelectronic machine (MEMS) and entertainment devices [3, 4].

1.2 BACKGROUND AND LITERATURE REVIEW

Investigation on active polymer materials started with some experiments on rubber bands in 1880. However, the effort that led to EAPs did not happen until discovering chemically stimulated polymers in 1949. Since the discovery of EAPs, they have been the subject of many studies. The main reason for this attention is that EAPs could be appropriate alternatives to the conventional actuator and sensor materials due to their small electrical energy consumption, light weight and compliant properties, biocompatibility, ability to operate in air and aquatic media, insensitivity to magnetic fields and simple fabrication procedures [1].

Since the 1960s ionic polymers have been used in fuel cells, but in 1992, the EAP characteristics and the electromechanical coupling of ion-exchange polymer-metal composites (IPMC) were discovered by three groups of researchers in Japan and in the United States [5-7]. Consequently, researchers developed IPMCs for various actuation applications such as biomedical devices [8], grippers and manipulation systems [9] and biomimetic robotics [10], [11]. Alternatively, IPMCs have inherent sensing properties and an applied force or deformation on an IPMC yields a detectable electrical signal, typically open-circuit voltage or short-circuit current, across the electrodes. These exceptional sensing capabilities make them applicable in the measurement of force, pressure, displacement and shear loading, structural health monitoring, and energy harvesting [12-16]. While there is a wide range of studies on IPMC actuation, the number of research considering IPMC electromechanical sensory properties is small. However, during

recent decades, more researchers have focused their investigations on the electromechanical transduction properties of IPMCs.

Studying IPMC electromechanical sensory properties began with testing of a bunch platinized circular Nafion membranes under different pressure ratios by Sadeghipour et al. [7]. Later, it was reported that there is a linear relationship between the output voltage and an imposed quasi-static tip displacement of an IPMC cantilever beam transducer and the short circuit current is proportional to the transducer tip velocity which suggests [17, 18]. An experiment conducted by Bonomo et al. showed that the output voltage signal of a cantilevered IPMC was influenced by hydration level, diluent, counter-ion, temperature and electrode material [19]. In 2009, Gao and Weiland modeled the electromechanical responses of IPMCs in bending mode based on streaming potential hypothesis [20]. This physics-based model assumes that net relative motion of this electrolyte with respect to the electrode results in a streaming potential. Later this streaming potential model was developed for current prediction in IPMCs subjected to shear deformation [13]. Bahramzadeh and Shahinpoor characterized IPMC sensors for curvature measurement of structures and showed that there is a linear relationship between the curvature of the IPMC sensor strip and the output voltage [14]. The role of electrode morphology in both bending and shear mode ionic polymer transducers was studied experimentally by Kocer and Weiland and related parameters were added to the streaming potential model [21, 22]. Later, some IPMC beam sensors were investigated in a vortex shedding flow-meter by Pasquale et al. [23]. Dominik et al. developed displacement sensors based on IPMCs for high frequencies [24]. Volpini et al. developed a model based on the continuum theory to predict the dynamic sensing response of IPMCs subject to a time-varying compression [25]. Electrochemical and morphological characteristics of IPMCs were investigated by Hong et al. and they demonstrated the dependence of electrochemical properties

on conductive network composite (CNC) nanostructure as well as the electromechanical performance of IPMC sensors as a function of CNC morphology [26].

A critical concern in the practical use of IPMCs in sensory applications is their strong humidity dependence in both air and other working environments (such as sea water, acid solution, gasoline) which could affect the uniformity of IPMC properties and even cause them fail to work [27, 28]. Hence, characterizing the influence of humidity on IPMCs has been interesting and some studies on that have been conducted. Bauer et al. studied the effect of humidity on the mechanical properties of a Nafion 117 film [29]. Shoji and Hirayama experimentally characterized the humidity effect on the performance of IPMC actuators [30]. Brunetto et al. statistically investigated sensing signals in typical working conditions using a linear model and characterized the humidity influence on IPMC sensors [27, 31]. Characterization of the solvent evaporation effect on IPMC sensors using a circuit model was conducted by Park [32]. And, the voltage response and the effects of various cations of IPMC sensors at multiple fixed levels of ambient humidity were investigated by Zhu et al. [33-35].

To tackle the humidity effect on IPMCs, a few encapsulation processes have been reported. Shahinpoor et al. and Akle and Leo proposed the encapsulation of IPMCs using Saran plastic membrane which is a high stiffness material and increases the IPMC Young's modulus considerably [16, 36]. Later, Barramba et al. proposed dielectric gel materials for encapsulation which showed a very low stiffness and a high dielectric constant [37]. Kim et al. coated IPMCs with isotactic polypropylene, silicone rubber and parylene and found that parylene was the most effective coating material to suppress water leakage [38]. And, Lei et al. coated IPMC sensors with thick parylene C coating and compared the performance of the encapsulated sensors to the typical naked ones [39].

Another attractive topic on IPMCs is modeling their electromechanical response. Comparing to the extensive work on modeling of IPMC actuators, research on IPMC sensing models has been relatively limited. First of all, Kanno et al. suggested a model in which parameters are determined empirically from curve fits of measured data [40, 41]. Later, using an analogy to piezoelectric materials, Newbury and Leo presented geometrically scalable 'grey-box' empirical models for IPMC actuators and sensors [17]. The advantage of the approach is that sensing and actuation could be modeled with a single scalable representation which is suitable for the design and development of IPMC devices and active material systems.

Even though empirical modeling techniques are suitable for engineering design, they do not include the fundamental physics associated with the charge sensing properties generated by ionic polymers. A static physics-based model of IPMC based on the concept of irreversible thermodynamics was proposed by de Gennes et al. [42]. This model considers electric field, current, pressure gradient, water flux, electric conductivity, hydraulic permeability and a cross-coupling term that models transduction between water flow and the flow of charge as the state variables and parameters. Tadokoro et al. proposed another model of IPMCs based on ionic motion in which electromechanical transduction is attributed to the forces imposed on the ions as they migrate through the polymer due to the imposition of an electric field and electrostatic interactions are also modeled [43]. Gao and Weiland modeled the electromechanical responses of IPMCs in bending mode based on streaming potential hypothesis which assumes that net relative motion of this electrolyte with respect to the electrode results in a streaming potential [19]. This physics-based model conceptually explained the sensing mechanism in bent IPMCs. Then, the streaming potential model was developed for current prediction in IPMCs subjected to shear deformation [12]. The role of electrode morphology in both bending and shear mode ionic polymer transducers

was studied experimentally by Kocer and Weiland and related parameters were added to the streaming potential model [20, 21].

A different model has been developed by Nemat-Nasser and Li using a field approach based on the micromechanics of ionic polymer materials and in this approach, actuation occurs due to the uptake of water at the interface between the polymer and the metal electrode [44, 45]. Unlike physics-based models, this model does not explicitly include water motion and hydraulic pressure gradients. The voltage sensing properties are modeled as the product of an effective dipole moment induced by mechanical deformation of the polymer. Later, Farinholt and Leo developed this model for the charge sensing response for a cantilevered IPMC beam under a step change based on a linear, one-dimensional partial differential equation [46]. The key assumption is that the initial charge density at the boundary is proportional to the applied deformation. Consequently, Chen et al. derived a dynamic model for IPMC sensors by solving the physics-governing PDE analytically in the Laplace domain which leads to a compact, explicit, transfer-function representation of the physics-based model [47].

1.3 RESEARCH OBJECTIVES

The main goal of this research is to fill some gaps in the previous studies on IPMC sensors and develop these materials for more practical applications. In detail, most studies on IPMC sensors have been devoted to fundamental sensing concepts using basic loads, not for specific electromechanical applications; developed IPMC sensor models are only useful for basic loads which are not quantitative accurate ones for specific applications; and while there have been many studies on characterizing the humidity effect, there is a lack of a comprehensive study on the effect

of a thin flexible waterproof coating on IPMCs' dynamic sensation. Accordingly, the significance of this PhD research could be summarized as follows:

1.3.1 Design, fabrication and calibration of IPMC dynamic pressure sensors in bending, compression and shear modes

This study takes advantage of appropriate properties of IPMCs such as relatively fast response, low cost, wide linear dynamic range, ease of preparation and exceptional mechanical flexibility [48] to design, fabricate and calibrate the IPMC dynamic pressure sensors in bending, compression and shear modes. The streaming potential hypothesis is hired to model the IPMC sensors and an equivalent RC circuit for the IPMC sensor, together with an interface signal conditioner is used to calculate the low and high cutoff frequencies and amplifying gain. Next, the direct assembly process (DAP) is utilized for fabrication and the calibration procedure is done in a standard pressure shock tube. Lastly, the time responses of 3 similar fabricated pressure sensors of each type subjected to different pressures are presented and consistency, linearity and sensitivity of the proposed pressure sensors will be discussed and three proposed sensor types will be compared.

1.3.2 Developing an explicit, dynamic, physics-based, rational transfer function for IPMC pressure sensors for real-time applications

The goal of this part of this research is to develop an explicit, dynamic, physics-based, rational transfer function for IPMC pressure sensors in compression, shear and bending modes that could be used in for real-time applications. The main advantage of this model is being a combination of physics-based models and simple models. As a physical model, it provides a valuable insight into

the sensing mechanism of IPMCs; and as a transfer function is suitable for analysis and design of system-theoretic tools. This work extends previous studies in two main aspects: it solves the problem due to an external pressure stimulation that makes the model appropriate for pressure sensors; unlike the previous studies, compression, shear and bending modes for arbitrary geometries are considered for IPMCs. Some experiments are done to validate the proposed dynamic model for IPMC pressure sensors. Direct assembly process (DAP) is hired for the fabrication process of the proposed IPMC pressure sensors and impulse stimulation is applied by utilizing a standard shock pressure tube setup. Finally, the time and frequency responses of three types of fabricated pressure sensors subjected to different pressures are presented and compared to results obtained from derived transfer functions.

1.3.3 Fabrication and characterization of highly flexible acrylic coated IPMCs

This part of study includes presenting the fabrication process of the proposed waterproof highly flexible IPMCs using gold sputter coating, acrylic spraying and the designed frames to stimulate fabricated IPMC segments in compression, bending and shear modes followed by the procedure of measuring impulse responses using a standard shock tube. Moreover, this comprehensive study on the effect of a thin flexible waterproof coating on IPMCs' dynamic sensation investigates compression and shear mode sensors offering a greater mechanical isolation from base. Finally, a couple of impulse excitation tests at several external pressures for both fabricated acrylic coated and uncoated IPMCs in different modes of deformation are conducted to verify how this waterproof coating suppresses the diluent permeation and maintains the IPMC sensing performance over time. Linearity, sensitivity and reliability of the fabricated IPMCs is discussed as well.

1.3.4 Fabrication and characterization of wearable IPMC sensors for real-time foot pressure mapping and gait analysis

This part of research takes advantage of the proposed highly flexible acrylic coated IPMCs in the fabrication of a self-powered smart flexible wearable insole for plantar pressure distribution measurement. For this aim, the basic mechanism of charge generation in IPMCs based on streaming potential theory and signal conditioning using a non-inverting amplifier are explained qualitatively, first. Eight circular highly flexible and acrylic coated IPMC pressure sensors are fabricated and fixed at some specific anatomic areas of a commercial cushioning gel insole which is fabricated from an advanced polymer gel that allows applied pressure to be converted into structural deformation which is then delivered to IPMC pressure sensors. Of course, each sensor is connected to a distinct signal conditioner with two insulated wires for data acquisition purposes. Afterward, the fabricated smart insole is employed for the real-time plantar pressure distribution analysis of a subject during static stance and gait cycles during walking and running. Resulted colormaps, representing pressure distribution, based on measured signals from IPMC sensors are quite reasonable for different phases of gait and show a good agreement with those from a commercial smart insole presented in the literature, which proves the reliability of the proposed self-powered flexible smart insole.

1.3.5 Fabrication and characterization of IPMC sensors for monitoring physiological and tactile signals

The purpose of this part of research is to develop IPMC sensors for monitoring blood pulse wave which is an important physiological signal as well as a flexible touch sensor taking advantage of

that these sensors can generate sensing signals without the requirement of additional power supply, in comparison with resistive and capacitive ones. For real-time monitoring of human blood pulse wave, a flexible IPMC rectangular segment is attached to the wrist directly upon the radial artery. Each pulse bit produces dynamic deformation of IPMC segment, and signals are generated due to positive ionic mobility inside the IPMC sensor. This work introduces the concept of a novel pulse bits rhythm sensing device and finally, the amplitude, frequency and shape of the pulse wave which is visualized will be discussed. Similarly, for developing a self-powered soft touch sensor, a flexible IPMC disk is located on a solid cylinder filled with silicone rubber and protected by a layer of polyamide. A non-inverting voltage amplifier is utilized to amplify the generated voltage while it eliminates the effect of internal resistance on amplification. Then, the effect of exciting frequency and the magnitude of applied touch force on the sensitivity of the sensor are investigated. Also, the touch device is pressed at a wide range of forces and signals to study its capability to produce various types of electrical signals. Results show an appropriate frequency independency and linearity for applied touch forces. The developed touch sensor is connected to an on-off switch circuit based on piezoelectricity to investigate its repeatability and stability. Finally, the 3D printing is hired to fabricate a designed flexible cap in order to limit the deformation of the IPMC segment and the generated voltage in a specific range and enhance the effectiveness of the proposed touch sensor for on-off switches.

2.0 IONIC POLYMER-METAL COMPOSITE (IPMC) PRESSURE SENSORS

As can be seen in the first chapter, most studies on IPMC sensors have been focused on the fundamental sensing concepts using basic loads and simple device configuration. Development of IPMC sensors for specific electromechanical applications is relatively rare. Moreover, no applicable compression and shear mode IPMC sensors have been developed until now while nowadays piezoelectric compression and shear mode sensors are more popular due to a greater mechanical isolation from base bending. This chapter takes advantage of dynamic properties of IPMCs such as relatively fast response, low cost, wide linear dynamic range, ease of preparation and exceptional mechanical flexibility [48] to design, investigate and calibrate the IPMC dynamic pressure sensors in bending, compression and shear modes in a shock pressure tube. For this aim, the streaming potential hypothesis is hired to model the IPMC sensors and an equivalent RC circuit for the IPMC sensor, together with an interface signal conditioner is used to calculate the low and high cutoff frequencies and amplifying gain. The fabrication process of the proposed IPMC pressure sensors using direct assembly process (DAP) is presented and the calibration procedure using shock tube is explained. It is worth noting that standard dynamic calibration of pressure sensors requires a source with a known amplitude of the pressure and a small raise time of the order of 1 ns, that can be easily obtained by utilizing shock pressure tubes [49]. Finally, the time responses of 3 similar fabricated pressure sensors of each type subjected to different pressures are

presented and consistency, linearity and sensitivity of the proposed pressure sensors will be discussed and three proposed sensor types will be compared.

2.1 CHARGE GENERATION MECHANISM AND EQUIVALENT CIRCUIT

According to the streaming potential hypothesis for IPMC sensing predictions, in the electrode regions where the metallic particulates come into contact with the electrolyte, which includes unpaired cations and diluent, an electric double layer (EDL) is evolved as observed in the experiment [50, 51]. Consequently, the relative motion of the electrolyte with respect to the electrode due to the IPMC deformation results in a streaming potential which is the distribution of the EDL formed at the electrode surface. In other words, according to this hypothesis, the sensing signal develops totally in the electrode region. The sensing signal development concepts in IPMCs for bending, compression and shear modes are explained in the following.

2.1.1 Bending mode

Then, for bending scenario, a pressure driven flow of electrolyte will cause the relative motion of the electrolyte with respect to the electrode, which is shown in Figure 2.1

As the electrolyte flows in the channels oriented in different directions, the EDL formed on the metallic phase of the electrode is disturbed, Figure 2.1. Therefore, a streaming potential is expected to develop while a streaming current occurs when the electrodes are shorted. Moreover, the sensing signal evolves exclusively in the electrode region where the EDL forms and metal

particulates communicate with each other. Then, the streaming current generated in each circular cylindrical nano-channel with radius $r_{channel}$ could be determined by [52],

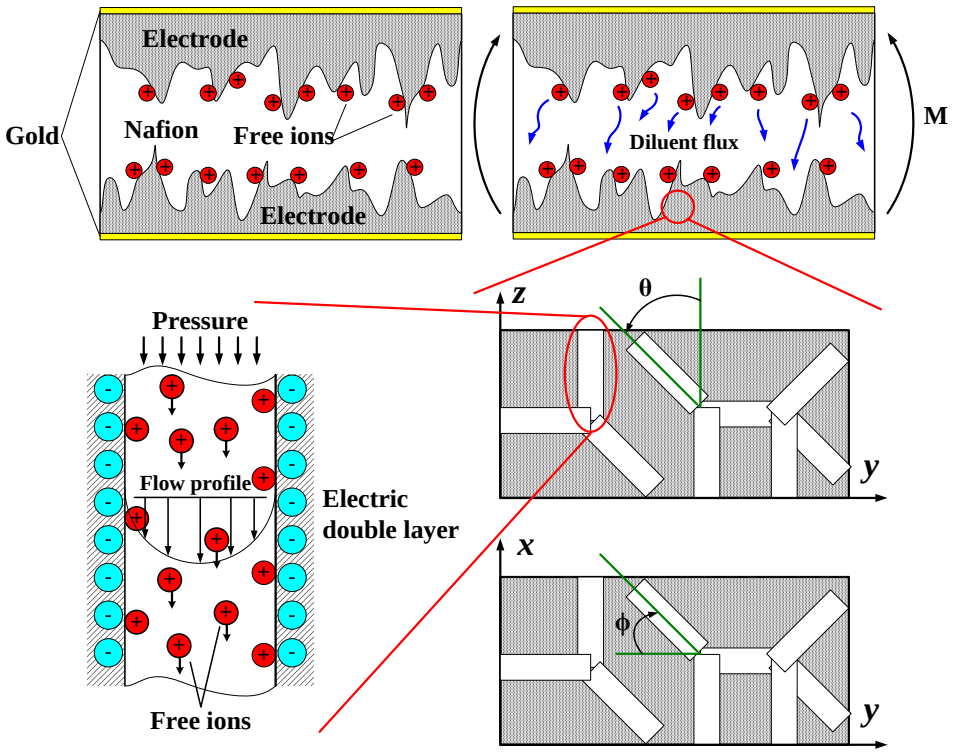

Figure 2.1. Schematic illustration of the evolution of streaming potential within the electrode region of an IPMC under bending

$$I_s = 2\pi \int_0^{r_{channel}} \rho(r_c) v(r_c) r_c dr_c, \tag{2.1}$$

where r_c is the distance from the channel center, $\rho(r_c)$ is charge density of unpaired counter-ions and $v(r_c)$ is flow velocity. It can be argued that a fluid velocity relative to the electrode evolves for any mode of deformation [50]. But here because of the structure of pressure sensor, the case of an IPMC in bending is developed. An expression for the velocity profile for a pressure driven flow within a circular channel, such as Poiseuille flow depicted in Figure 2.1, is expressed as

$$v(r_c) = \frac{\Delta P(r_{channel}^2 - r_c^2)}{4\mu l_{channel}}, \tag{2.2}$$

where ΔP is the pressure difference between the two ends of the nanochannel caused by bending, μ is the viscosity of the electrolyte, and $l_{channel}$ is the length of the channel. Bending an IPMC will result in a pressure gradient between the compressed and the expanded electrodes, i.e., a pressure difference between the two ends of the nanochannel. The instantaneous pressure gradient in a nanochannel can be estimated from the stress difference between the two sides of the membrane.

In this hypothesis, the extremely small size of the channel makes the electric double layers in the channel overlap and the charge density in the flow becomes a uniform magnitude ρ_e. Then the streaming current in a single channel is given as

$$I_s = \frac{\pi \rho_e r_{channel}^4}{8\mu l_{channel}} \Delta P(r), \tag{2.3}$$

where r is the distance of the channel from the IPMC center. The average pressure difference for IPMC's two surfaces can be obtained as

$$\Delta P_{ave} = \frac{\oint_{A_{IPT}} \Delta P(r)}{A_{IPT}}, \tag{2.4}$$

where A_{IPT} is the surface area of IPMC sensor and ΔP_{ave} can be used as a constant pressure difference for all nanochannels located at any radius of IPMC.

Equation (2.3) gives the streaming current for a perfectly aligned channel, which is in the direction of the IPMC thickness. Nevertheless, channels in the electrode region are randomly oriented. To take this effect into account, I_s should be multiplied by transformation function $T(\theta, \phi)$ which transforms I_s from the perfectly aligned direction to an arbitrary direction, where, θ and ϕ are the rotation angles about of x and z axis, respectively.

In order to estimate the current from the entire sensor, a summation over all channels is required. The total current that can be obtained from an IPMC due to compression is then calculated by adding channel streaming currents of all nano-channels in the electrode layer, as,

$$I_t = \sum_{i=1}^{N_{channels}} T(\theta_i, \phi_i) \frac{\pi \rho_e r_{channel}^4}{8\mu t_{IPMC}} \Delta P_{ave}. \quad (2.5)$$

As can be seen, ΔP_{ave} is not a function of channel's alignment and then could be taken out of the summation. Equation (2.5), due to lack of accurate quantities of IPMC's properties, cannot be used for precise predictions, but it clearly shows a linear relationship between the applied pressure and generated electrical current in the IPMC bended.

2.1.2 Compression mode

For compression scenario, when a deflection is imposed in the direction of the IPMC thickness, diluent infused in the hydrophilic regions tends to move and transport the free ions as well. This phenomenon has been previously proposed by Weiland and Akle [53] and illustrated in Figure 2.2.

Again, the streaming current generated in each circular cylindrical nano-channel is the same as (2.1) and the electrolyte flow profile will be as (2.2). For the pressure sensor, the stress, σ, seen by the global IPMC is actually the external pressure, P_0. Consequently, the portion of the stress seen by a single nano-channel is estimated to determine the pressure difference between the ends of a channel by applying the Voigt approach, where the strain is the same in all channels of the model. The pressure difference leading to electrolyte flow is then determined by,

$$\Delta P(r) = \Delta P = P_0 \frac{l_{channel}}{t_{IPMC}}, \quad (2.6)$$

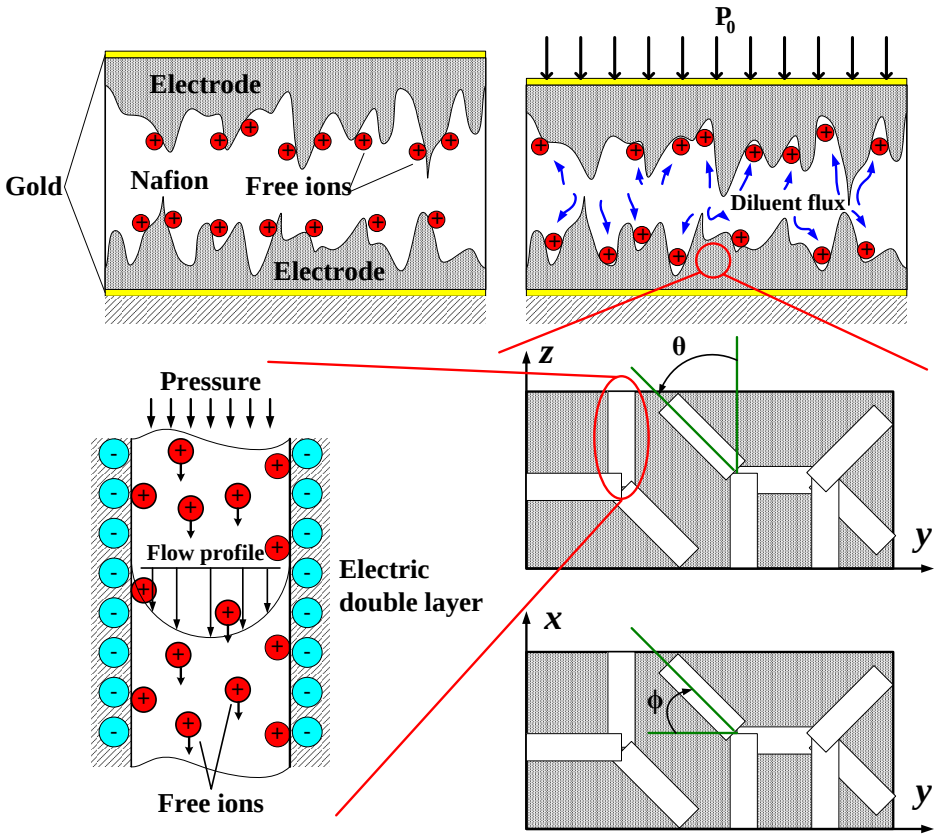

Figure 2.2. Schematic illustration of the evolution of streaming potential within the electrode region of an IPMC under compression

where t_{IPMC} is the IPMC sensor thickness. Knowing the pressure difference, the velocity profile throughout the cross-section of the nano-channel is calculated using (2.2). Then, the instantaneous pressure gradient for different radiuses can be substituted in the streaming potential hypotheses as a function of the applied pressure which is supposed to be measured by the pressure sensor. In the literature, it has previously been proposed that the charge density of the electrolyte has a constant value for a nano-channel existing in the IPMC [51]. In an IPMC, the EDLs of the adjacent walls of a channel overlap since the channel radius is smaller than the Debye length that is beyond the EDL effective zone and has zero charge density. Therefore, the charge density of the electrolyte

in nano-channels becomes a unipolar solution of counter-ions at a uniform concentration of ρ_e that neutralizes the surface charge of the channel. Then the streaming current in a single channel is

$$I_s = \frac{\pi \rho_e r_{channel}^4}{8\mu t_{IPMC}} P_0. \tag{2.7}$$

Equation (2.7) gives the streaming current for a perfectly aligned channel, which is in the direction of the applied displacement. Nevertheless, channels in the electrode region are randomly oriented. To take this effect into account, I_s should be multiplied by transformation function $T(\theta, \phi)$ which transforms I_s from the perfectly aligned direction to an arbitrary direction, where, θ and ϕ are the rotation angles about of x and z axis, respectively.

In order to estimate the current from the entire sensor, a summation over all channels is required. The total current that can be obtained from an IPMC due to compression is then calculated by adding channel streaming currents of all nano-channels in the electrode layer, as,

$$I_t = \sum_{i=1}^{N_{channels}} T(\theta_i, \phi_i) \frac{\pi \rho_e r_{channel}^4}{8\mu t_{IPMC}} P_0. \tag{2.8}$$

As can be seen, P_0 is not a function of channel's alignment and then could be taken out of the summation. Equation (2.8), due to lack of accurate quantities of IPMC's properties, cannot be used for precise predictions, but it clearly shows a linear relationship between the applied pressure and generated electrical current in the IPMC under compression which is vital in sensor applications.

2.1.3 Shear mode

A schematic interpretation of the development of the streaming potential due to IPMC shear deformation is illustrated in Figure 2.3. Of the modes of IPMC sensing deformation, the pure shear

mode due to the absence of a hydrostatic component of loading is probably the most difficult one and this complicates strategies for estimating the nature of the diluent flow. In shear sensing modeling, similar to other modes, the diluent flow through the nano-channels which is formed in the electrode layers due to the shear stress that is applied to the walls of a single channel should be estimated first. Unlike compression mode scenario, square cross-section channels are considered for the shearing mode case to make the calculation of diluent flow due to shear deformation through the channel more reasonable.

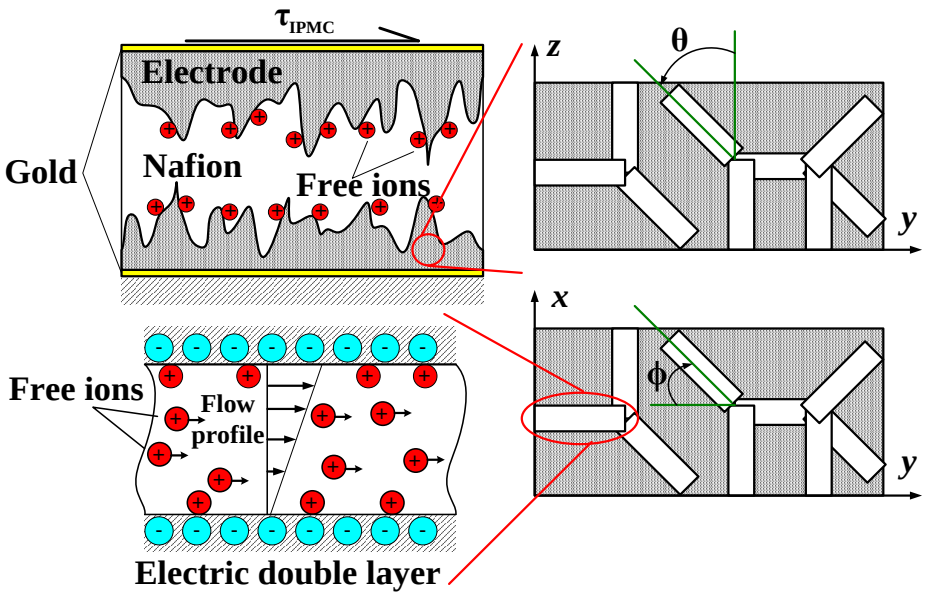

Figure 2.3. Schematic illustration of the evolution of streaming potential within the electrode region of an IPMC under shear

Again, assuming that the electrode double layers of the channel wall are expected to overlap and the diluent may be treated as a unipolar solution, the streaming current generated in each square cross section nano-channel with width of w and height of h and for flow charge density ρ_e, is determined by [52],

$$I_s = \rho_e w \int_0^h v(y)dy, \tag{2.9}$$

where y is the distance from the lower wall of the channel and $v(y)$ is the velocity of the diluent within the nano-channel. Turning to the elementary definition of viscosity where the fluid is suspended between two infinite plates, it is understood that motion of one of these plates relative to the other will result in a shear stress and subsequent flow in the fluid with a flow profile described by

$$\tau = \mu \frac{v(y)}{dy}. \tag{2.10}$$

A small value of wall shear stress is estimated and imposed to generate a flow in the channel where the channel walls are assumed to be solid without pores. Using the Voigt approach in order to relate the shear load applied to the sensor, τ_{IPMC}, to the shear load observed by the channel's wall, τ, one will get,

$$\tau = \tau_{IPMC} \frac{l_{channel}}{l_{IPMC}}, \tag{2.11}$$

where $l_{channel}$ is the length of the nano-channel and l_{IPMC} is the length of IPMC sensor in the direction of applied shear force. Using shear stress observed by the channel's wall in (2.11) and substituting the velocity profile in (2.10), the streaming current in a single channel is

$$I_s = \frac{\rho_e w h^2 l_{channel}}{2\mu l_{IPMC}} \tau_{IPMC}. \tag{2.12}$$

While in real structures the diluent flow paths within the electrode region are necessarily oriented randomly as shown in Figure 2.3, (2.12) gives the streaming current for a perfectly aligned channel, which is in the direction of the applied shear force. Like what developed for compression mode, the streaming current developed in a nano-channel for a given orientation is obtained by

multiplying I_s by transformation function $T(\theta, \phi)$, where, θ and ϕ are the rotation angles about of x and z axis, respectively.

In order to estimate the total current generated by the sensor under applied shear force, a summation over all channels is required. The overall current that can be obtained from an IPMC due to applied τ_{IPMC} shear is then calculated by adding channel streaming currents of all nano-channels in the electrode layer, as,

$$I_t = \sum_{i=1}^{N_{channels}} T(\theta_i, \phi_i) \frac{\rho_e w h^2 l_{channel}}{2\mu l_{IPMC}} \tau_{IPMC}. \quad (2.13)$$

Equation (2.13) due to lack of accurate quantities of IPMC properties, cannot be used for precise predictions, but, because τ_{IPMC} is a constant that is not a function of channel's alignment, it shows a linear relationship between the applied shear force and generated electrical current in the IPMC which is so important in sensor applications.

2.1.4 Equivalent circuit

According to the developed model, IPMC pressure sensor, such as piezoelectric materials, generates an electrical charge that is proportional to the applied pressure. If a reciprocating force is applied, an AC voltage is seen across the terminals of the device. But it is not suited for static or DC applications because the electrical charge produced decays with time due to the internal impedance of the sensor. An IPMC sensor could be modeled as a charge source with a shunt capacitor and resistor which is shown in Figure 2.4 [54]. As shown in the previous section, the charge produced depends on diluent, electrode structure and the geometry of sensor and equivalent resistance and capacitance can be obtained experimentally using impedance analyzer.

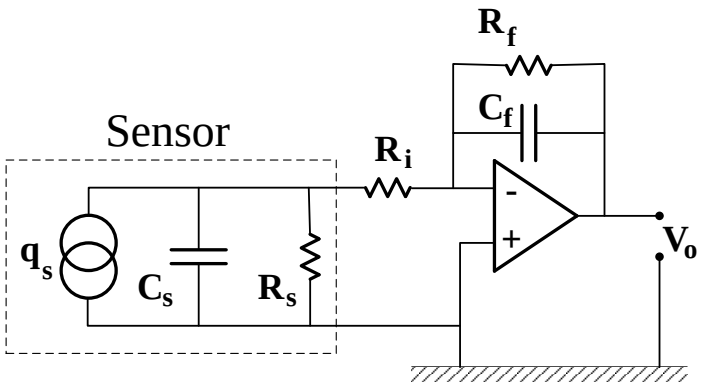

Figure 2.4. Sensor's equivalent circuit and signal conditioner

Normal output voltages from IPMCs can vary from microvolts to hundreds of volts, and signal conditioning circuitry requirements vary substantially. Main objectives to consider when designing an amplifier include frequency of operation, signal amplitude and input impedance [54]. The charge amplifier, which is shown in Figure 2.4, balances the charge injected into the negative input by charging feedback capacitor C_f. Resistor R_f bleeds the charge off capacitor C_f at a low rate to prevent the amplifier from drifting into saturation. The value of R_f and C_f set the low cutoff frequency of the amplifier, while R_s, R_i and C_s play a role in high cutoff frequency.

According to Figure 2.4, the equivalent impedance for input and feedback parts will be as

$$Z_1 = \frac{R_s}{R_s s C_s + 1} + R_i,$$
$$Z_2 = \frac{R_f}{R_f s C_f + 1}, \tag{2.14}$$

where s is the complex variable of s-domain. Then the transfer function for the whole circuit is

$$H(s) = -\frac{Z_2}{Z_1} = -\frac{R_f(R_s s C_s + 1)}{(R_f s C_f + 1)[R_s + R_i(R_s s C_s + 1)]}. \tag{2.15}$$

Two poles can be identified for this transfer function that gives low and high cutoff frequencies,

$$f_L = \frac{1}{2\pi R_f C_f}, \qquad f_H = \frac{R_s + R_i}{2\pi R_s R_i C_s}. \tag{2.16}$$

Moreover, by solving the current equation for the circuit, the output voltage with the following equation is related to the generated charge,

$$V_o = -\frac{q_s}{C_f}. \tag{2.17}$$

2.2 FABRICATION PROCESS AND EXPERIMENTAL SETUP

The purpose of the IPMC fabrication approach is to maximize the sensing signal. The DAP was selected for IPMC fabrication because it enables the usage of any type of ionomer, diluent, and conducting powder. It also allows direct control over the electrode thickness and composition [55]. EmI-Tf, a type of ionic liquid, was chosen as the diluent because it is stable in air and therefore eliminates dehydration effects [56]. The ionomer and the counter-ion are selected, Nafion 117 and lithium respectively. The specific procedure employed to fabricate the ionic polymer pressure sensors could be summarized as:

1. The Nafion membrane is boiled in sulfuric acid (H_2SO_4) 1 M solution for half an hour (Essentially cleaning).

2. The cleaned membrane is boiled in metal salt (for example; LiCl) solution for two hours to exchange protons (H^+) with metal cations (for example; Li^+) and then rinsed with deionized (DI) water to remove excess metal salt precipitates.

3. The ion exchanged membrane is boiled in DI water for two hours to be cleaned, and then dried in a 150 °C oven for 12 hours to remove unbound water in the ionomer to the extent practicable.

4. The dried Nafion is soaked in the ionic liquid, EmI-Tf, in a 150 °C oven for two hours for diluent uptake. (This step is conducted before application of the electrodes to avoid swelling-induced cracking, especially in the thin gold layer. And this is which we call direct assembly process with solvated membranes.)

5. The electrode solution mainly consists of high surface area ruthenium dioxide (RuO_2) conductive metallic powder and 5% Nafion polymer solution. In the preparation of the electrode mixture, first, RuO_2 and Nafion solution are mixed, 42% and 58% by volume, respectively. Second, the ionic liquid is added to the metallic powder-polymer solution mixture so as to weigh 58% of the polymer solution. Furthermore, DI water and isopropyl alcohol are added to increase the dispersion while they will evaporate during the subsequent steps. To assure uniformity of the electrode solution, the mixture is stirred with a magnetic stirring bar for 20 min, then sonicated for 100 min, and then stirred again for 20 min. The mixture is painted as several layers on each surface of the Nafion.

6. Finally, the electrode painted membrane is sandwiched between gold sheets to melt press two layers of gold (50 nm thick) on the outer surfaces of the sample to increase conductivity on the surfaces of the transducer.

The structure of the bending mode sensor which has a circular shape is shown in Figure 2.5(a). The sensor includes Nafion 117 layer at the middle, electrode layers on Nafion's both surfaces and layers of gold sheets on outer surfaces of electrodes to improve the conductivity. Then all these layers are mounted between two rings of plastic as the frame and output wires are connected to electrodes. The structure of the compression mode sensor is almost the same as bending mode one but the IPMC is located on a plastic frame which is supported by a metal substrate that prevents it from bending on one surface, and the other surface is exposed to external pressure, Figure 2.5(b). Besides, the structure of the shear mode pressure sensor is depicted in Figure 2.5(c). A rectangular IPMC layer, made of the same layers as compression mode one, is sandwiched between a solid core cylinder that transfers the applied pressure to IPMC and a fixed cylindrical hole which acts as a frame for the sensor.

The time responses of fabricated pressure sensors were obtained using a shock pressure tube test setup. As shown in Figure 2.6, shock tube consists of two sections: the high-pressure chamber connected to an air reservoir with the chamber pressure controlled by a dual stage air regulator; and a low-pressure chamber which is connected to the atmosphere at one end. Two sections are coupled with bolts on flanges and an elastic membrane sandwiched between the flanges divides the two sections. Six sensor-mounts are welded oppositely on the driven tube. Hence, for each test, fabricated IPMC sensor and standard pressure sensor can be placed on the same cross-section of the tube to measure the comparable pressure value. Both sample and commercial pressure sensor are connected to the oscilloscope (Agilent DSOX4024A Oscilloscope) for sensor output signal monitoring.

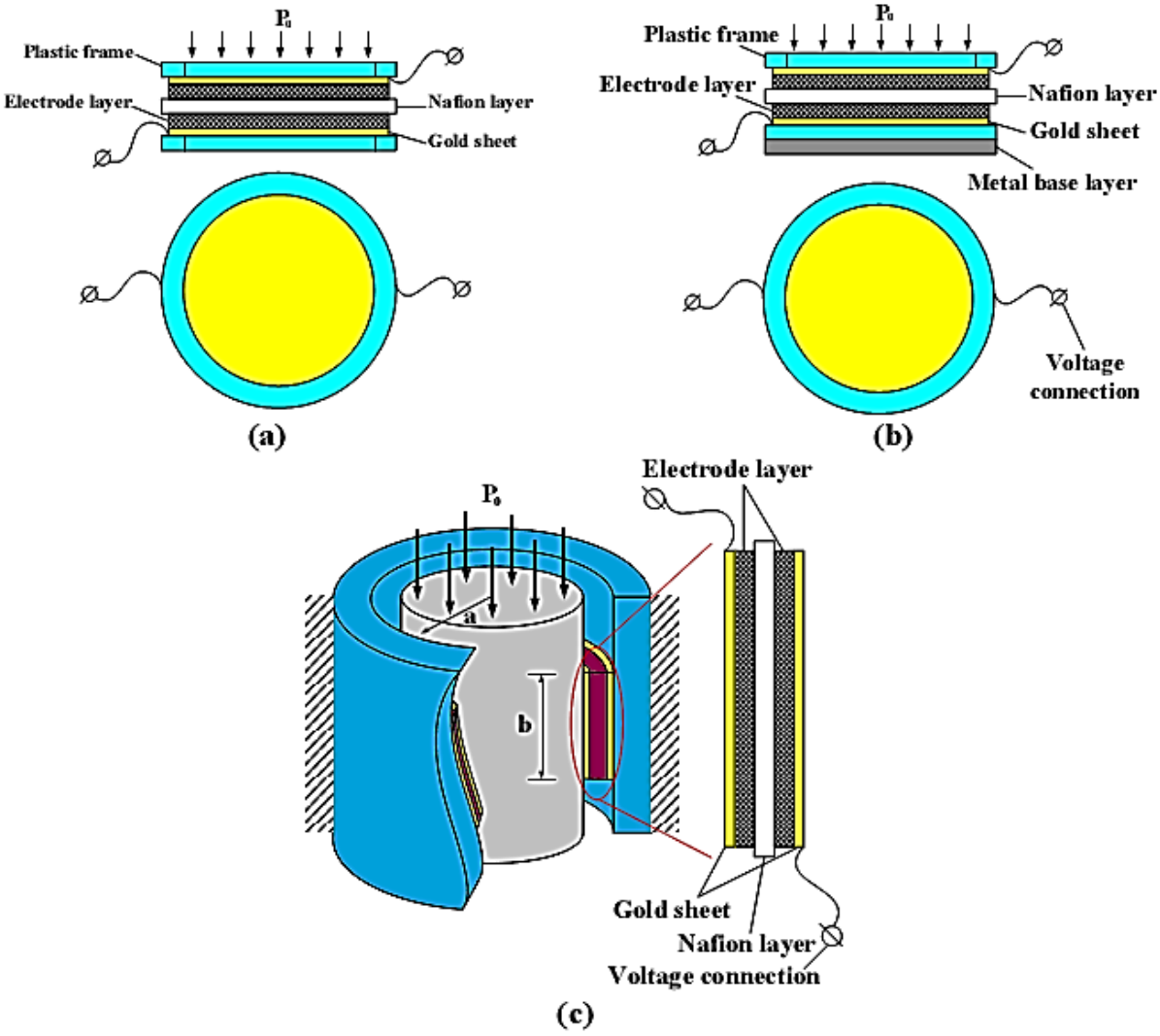

Figure 2.5. Pressure sensors' structure

Operation steps for this setup are as following [57]:

1) IPMC pressure sensor and standard sensor are installed on two holes of the shock tube at the same cross section.

2) A specific membrane is placed between high pressure and low-pressure chambers and these two parts are fixed with bolt connection. In order to calibrate the sensitivity of the fabricated

sensor, different blast pressure should be obtained. Thus, various membranes with different materials and layer are used.

3) The valve of air reservoir is released and the high-pressure chamber starts filling with high-pressure air.

4) By increasing the pressure in the high-pressure chamber, the membrane will finally get ruptured, and a blast pressure wave which propagates along in the low-pressure tube is produced. The same pressure is applied to both the IPMC and standard sensors and electrical signals are generated and monitored by the oscilloscope. Therefore, the peak value of the signal is related to the applied pressure on the sensor.

5) Changing membrane materials and the number of layers lead to different pressure waves and by comparing the data between two sensors, the fabricated pressure sensors can be calibrated.

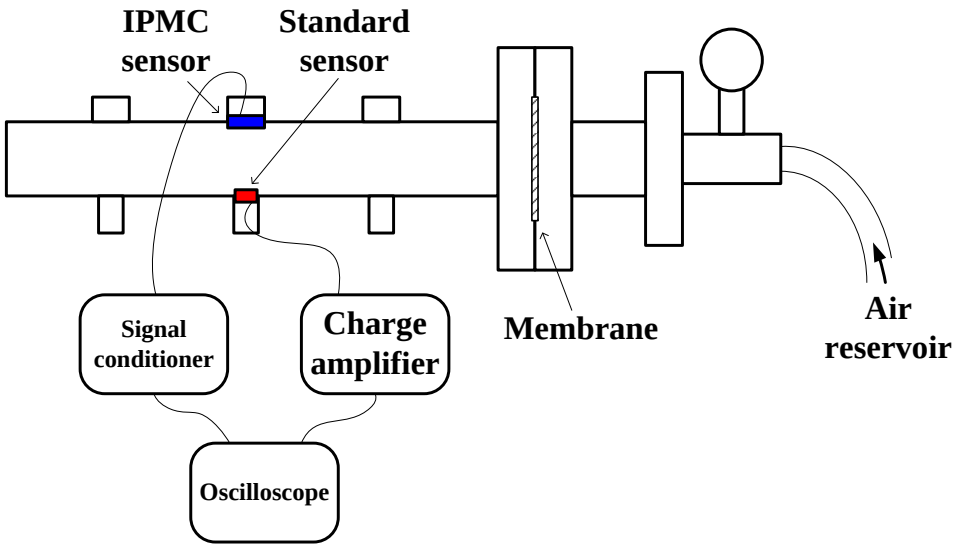

Figure 2.6. Schematic view of the experimental setup

Sensor housing was designed and fabricated using 3D printed polymer. The frames were connected using cyanoacrylates.

2.3 RESULTS AND DISCUSSIONS

For each type of sensation, bending, compression and shear, three IPMC pressure sensors with identical electrode material were fabricated. In the utilized electrode material, RuO_2 and Nafion solution are mixed 42% and 58% by volume, respectively, and the thickness of the electrode mixture is 15 μm on each side of the Nafion 117 membrane. The surface resistance of IPMCs, before melt pressing 50 nm gold sheet on it, is 75 Ω/cm which reduces to 1.5 Ω/cm after being sandwiched between gold layers. The radius of the fabricated bending and compression mode samples are 10 mm but a circle of radius 6.5 mm of them is exposed to the applied pressure and one of each fabricated samples is depicted in Figure 2.7(a) and Figure 2.7(b), respectively. The IPMC layer which is used in shear mode samples is a 3.5×41 mm rectangle which is wrapped around a 6.5 mm diameter circular cylinder, Figure 2.7(c). Using these dimensions makes surfaces to which the pressure is applied and effective areas of IPMCs equal for both type of sensors and then the comparison of sensitivities which are only functions of deformation is meaningful.

In order to obtain equivalent capacitance and resistance of fabricated sensors Agilent 4294A precision impedance analyzer is used and the parallel resistance and capacitance response for three fabricated samples of each sensor type in the frequency domain are given in Figure 2.8, Figure 2.9 and Figure 2.10, respectively. Moreover, the magnitude of equivalent capacitance and resistance for each IPMC pressure sensor of each type is given in Table 2.1.

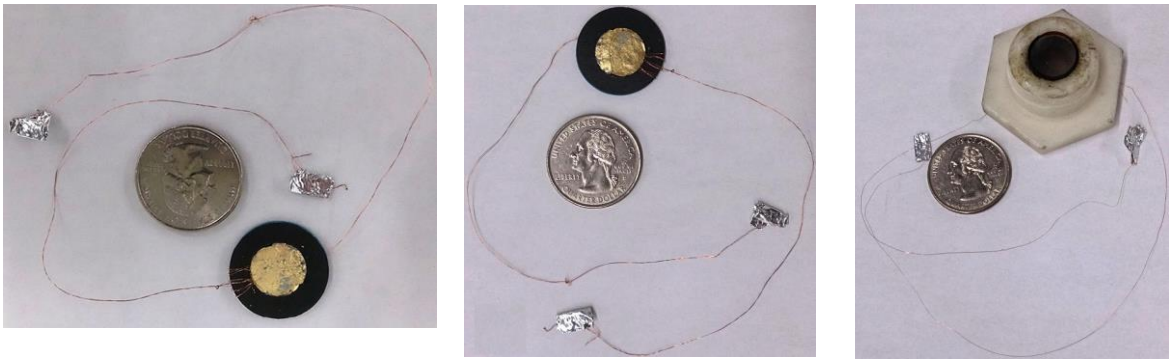

(a) **(b)** **(c)**

Figure 2.7. Fabricated IPMC pressure sensors using DAP

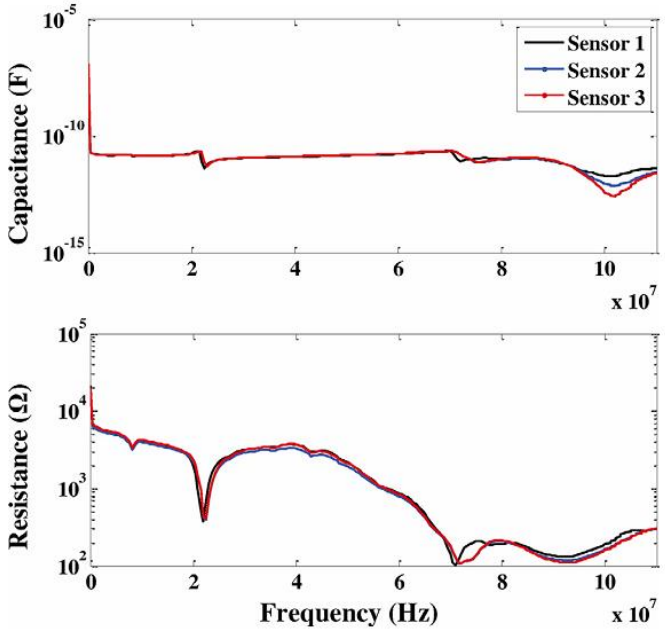

Figure 2.8. Parallel resistance and capacitance response of fabricated bending mode sensors

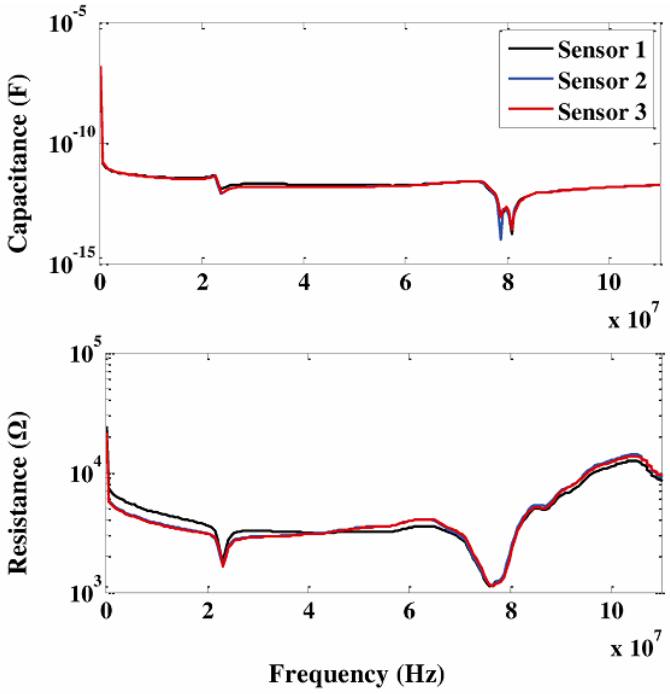

Figure 2.9. Parallel resistance and capacitance response of fabricated compression mode sensors

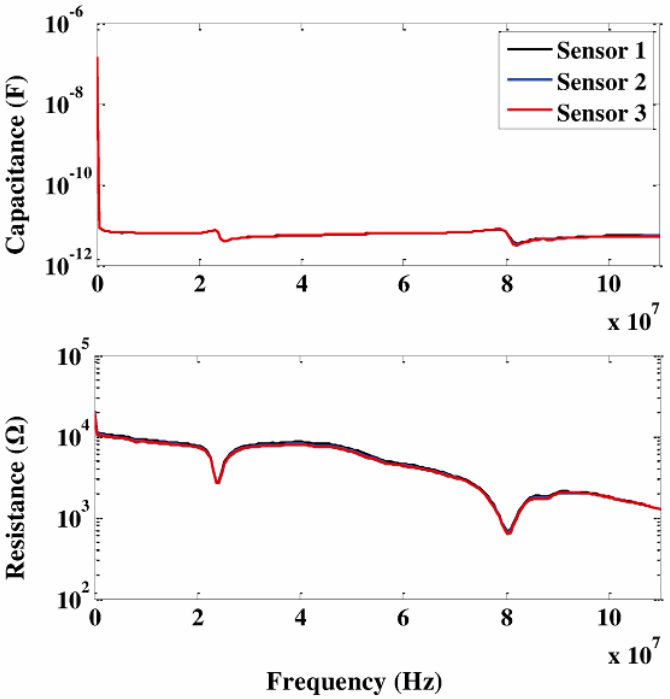

Figure 2.10. Parallel resistance and capacitance response of fabricated shear mode sensors

Table 2.1. Equivalent capacitance and resistance of fabricated sensors

Sensor type	Sensor #	Equivalent capacitance (nF)	Equivalent resistance (kΩ)
Bending	1	122	21.2
	2	125	17.8
	3	195	19.5
Compression	1	115	24.0
	2	148	20.0
	3	154	21.4
Shear	1	132	20.6
	2	137	19.9
	3	142	19.4

According to Table 2.1, the average value for equivalent capacitance and resistance of three bending mode sensors are 147.3 nF and 19.5 kΩ, respectively. The average value for equivalent capacitance and resistance of three compression mode sensors are 139 nF and 21.8 kΩ, respectively, and these quantities for shear mode sensors are 137 nF and 19.97 kΩ, respectively. By setting the signal conditioner elements as $R_f = 100\ k\Omega$, $C_f = 1\mu F$ and $R_i = 10\ \Omega$, the system low and high cutoff frequencies for bending mode sensors will be $f_L = 1.59\ Hz$ and $f_H = 108.1\ kHz$, respectively, for compression mode sensors will be around $f_L = 1.59\ Hz$ and $f_H = 114.5\ kHz$, respectively, and for shear mode sensors will be around $f_L = 1.59\ Hz$ and $f_H = 116.2\ kHz$, respectively. And the amplification is $1000000\ V/C$ for all sensors. Meanwhile, OP177 which is fed by 9V batteries has been used as the operational amplifier.

Each IPMC pressure sensor sample and the standard pressure sensor, PCB116B02, are mounted on the shock tube, 54 mm diameter, at the middle holes, 310 mm distance from the membrane. Three different membranes including single layer Mylar, Aluminum sheet and double layer Mylar have been used in order to produce different shock pressures. The response of each sensor has been captured 3 times for each membrane and this procedure was done for 3 similar

fabricated sensors of each type. The photo of the experimental test rig utilized is shown in Figure 1.1.

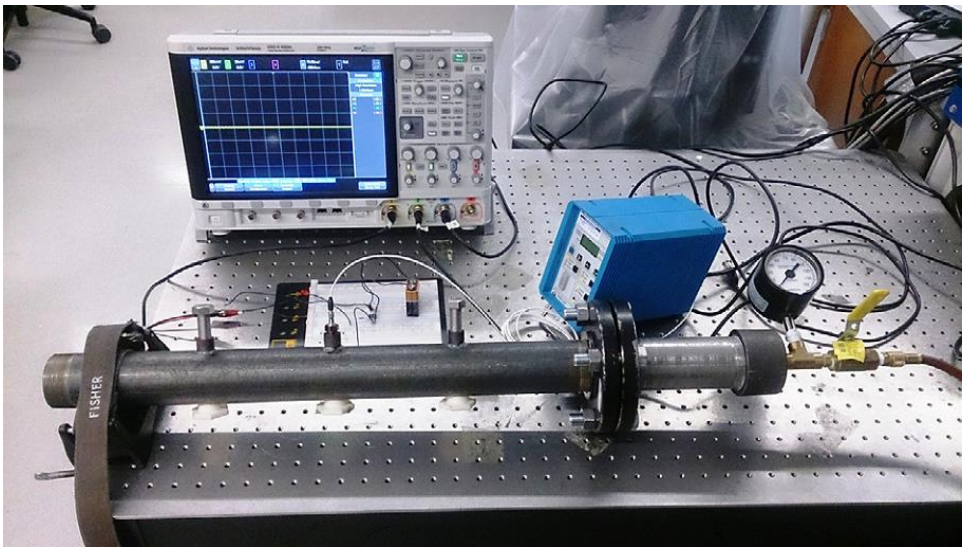

Figure 2.11. Photo of the shock pressure tube and measurement setup

Time responses for bending, compression mode and shear mode sensors are depicted in Figure 2.12 through Figure 2.20, respectively, and compared with the standard commercial pressure sensor response. By comparing the peak values of each sensor's output to the standard pressure sensor's signal, calibration curves can be drawn. The peak pressure data for all tests of bending mode, compression mode and shear mode sensors are given in Table 2.2, Table 2.3 and Table 2.4, respectively. These tables contain amplitude of shock wave and corresponding generated charge in IPMC sensors as well as measured output sensors' voltages for different IPMC sensors and membrane layers.

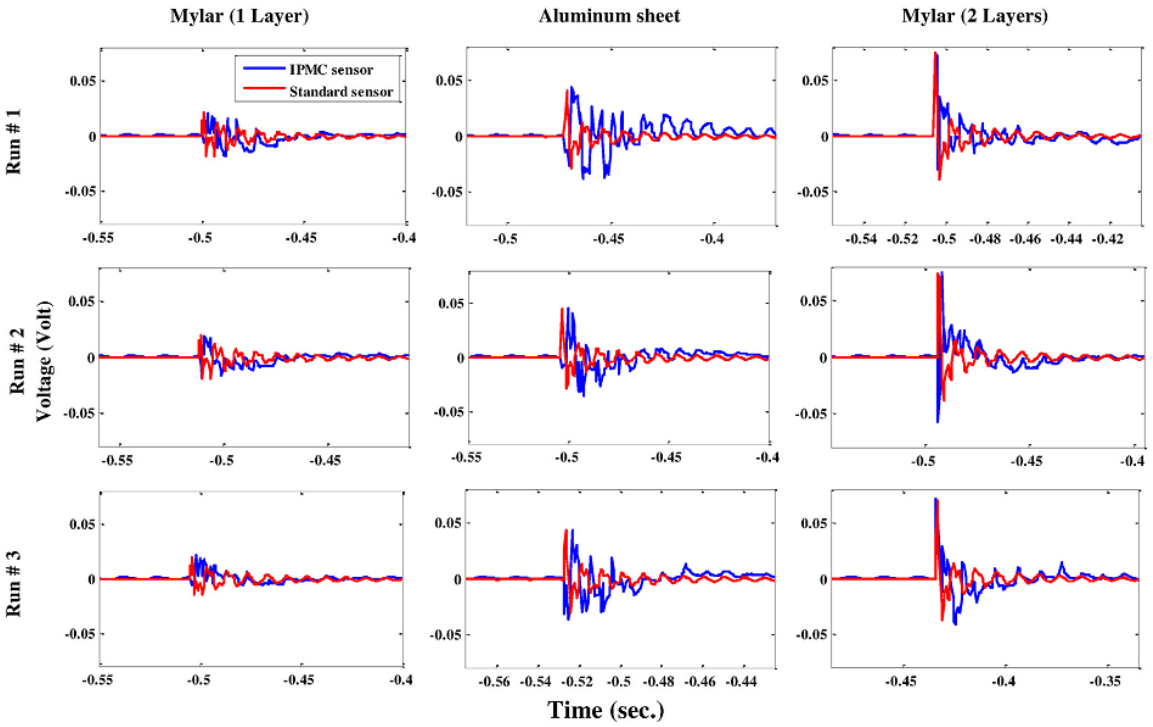

Figure 2.12. Time responses for bending mode sensor 1

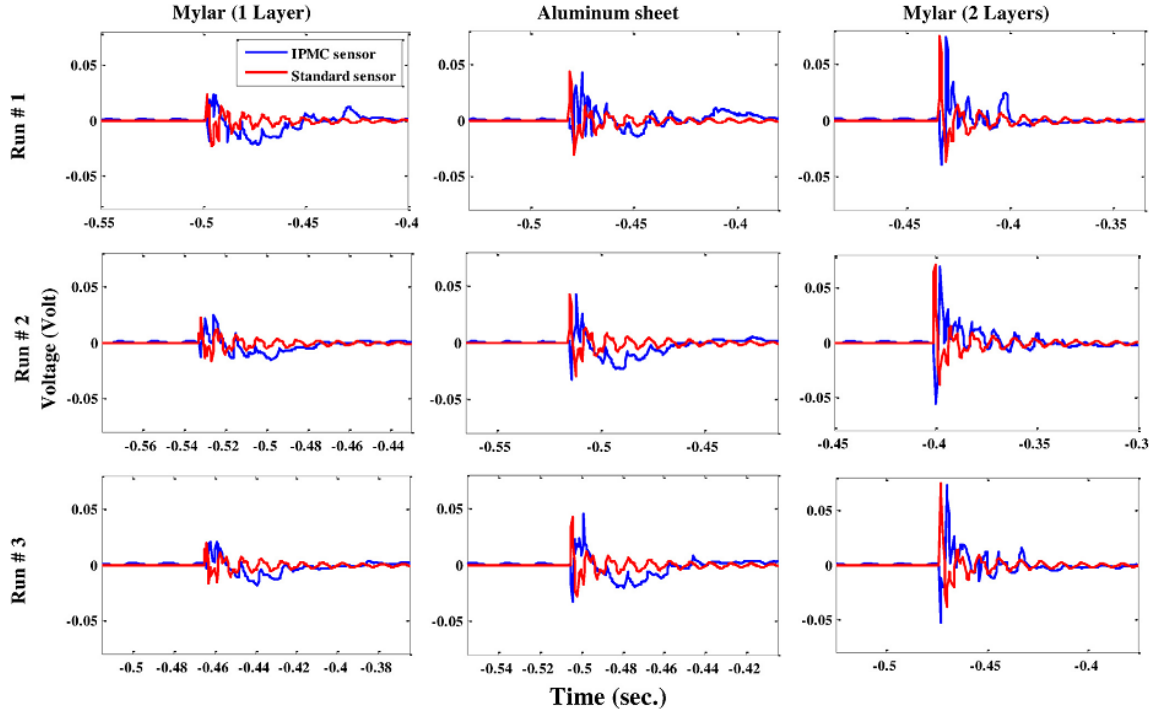

Figure 2.13. Time responses for bending mode sensor 2

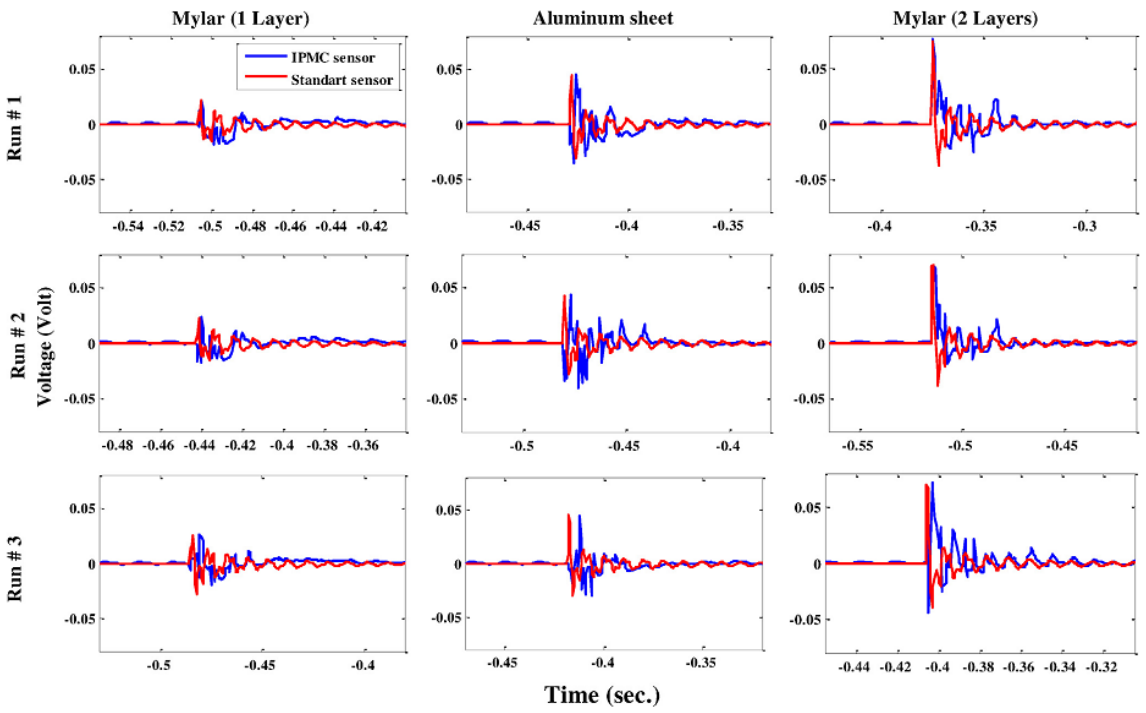

Figure 2.14. Time responses for bending mode sensor 3

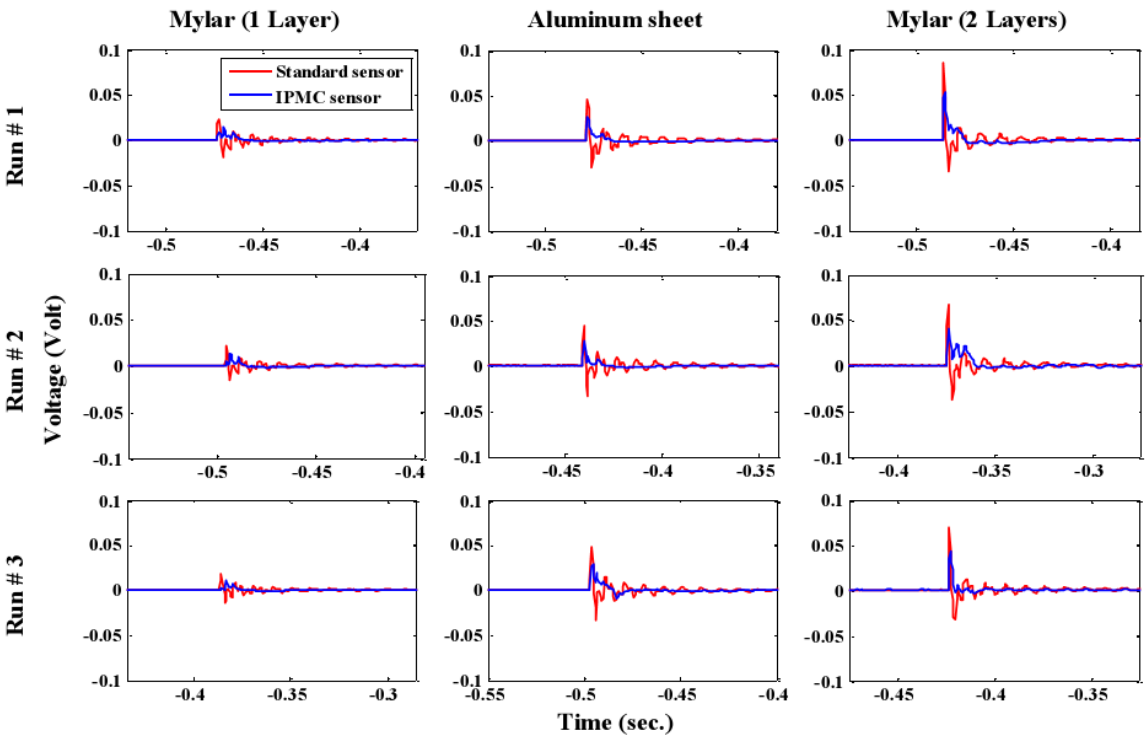

Figure 2.15. Time responses for compression mode sensor 1

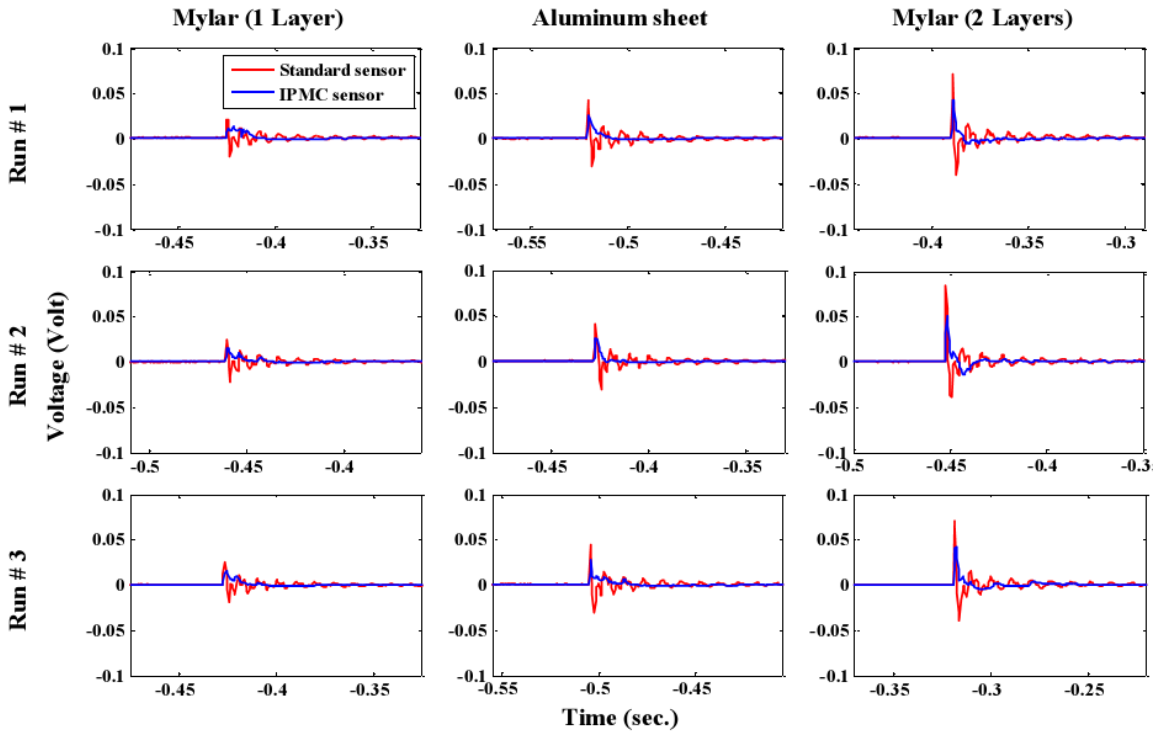

Figure 2.16. Time responses for compression mode sensor 2

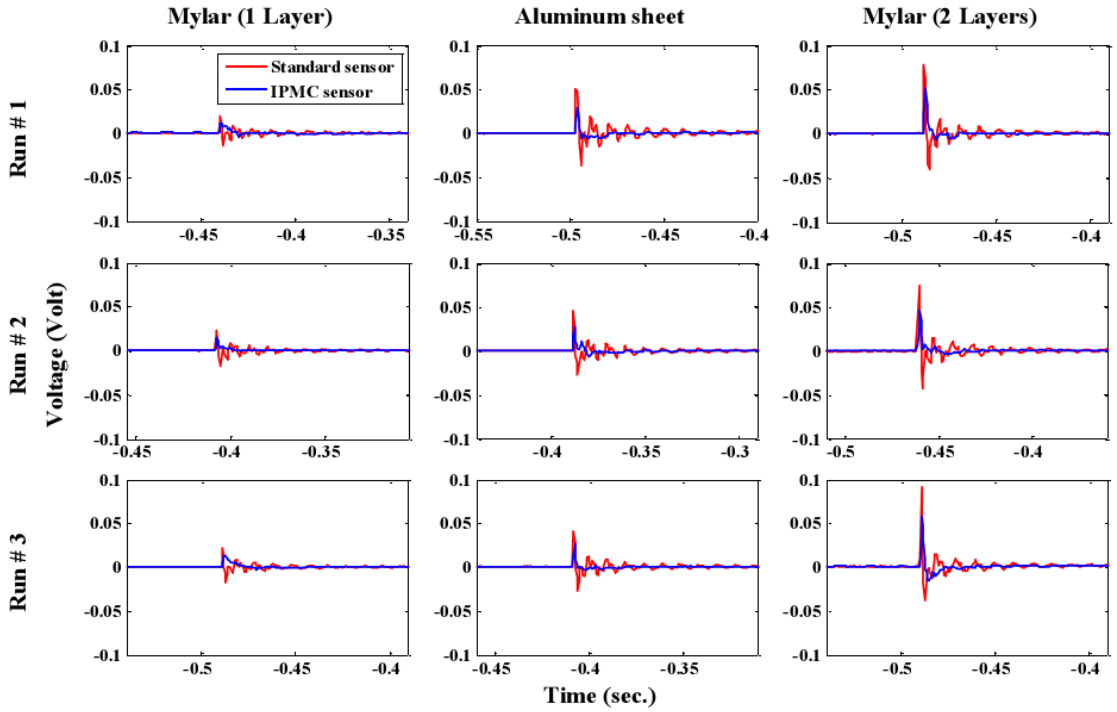

Figure 2.17. Time responses for compression mode sensor 3

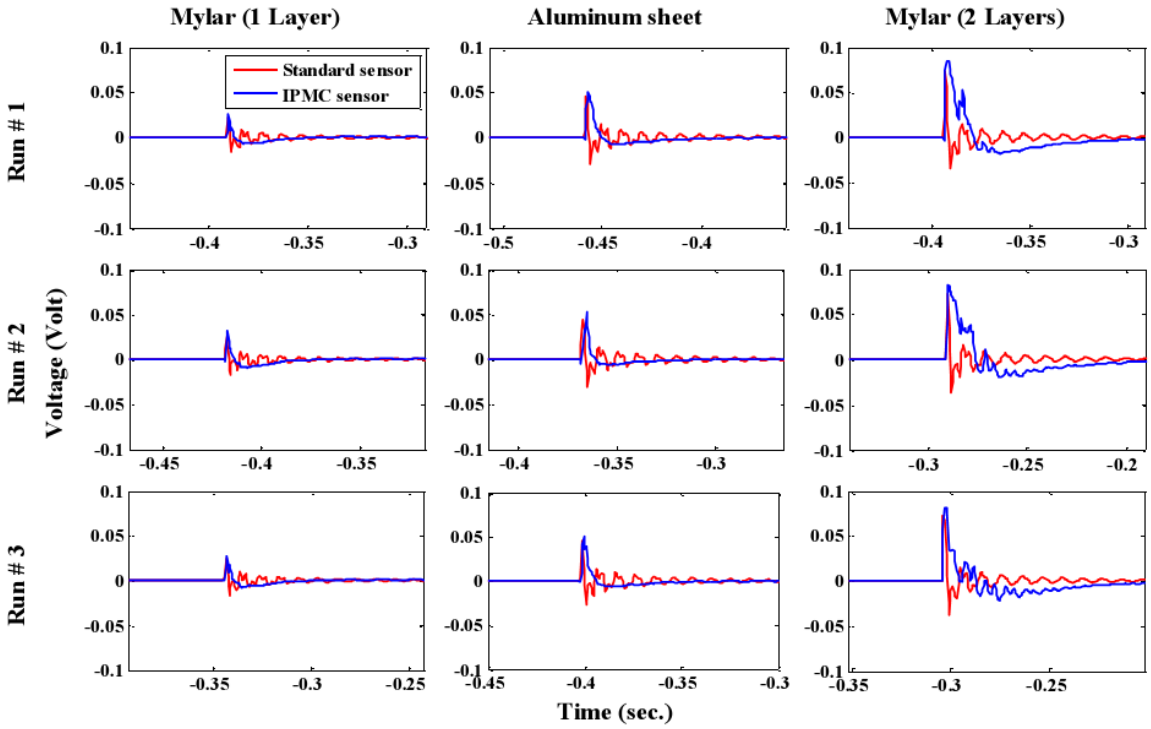

Figure 2.18. Time responses for shear mode sensor 1

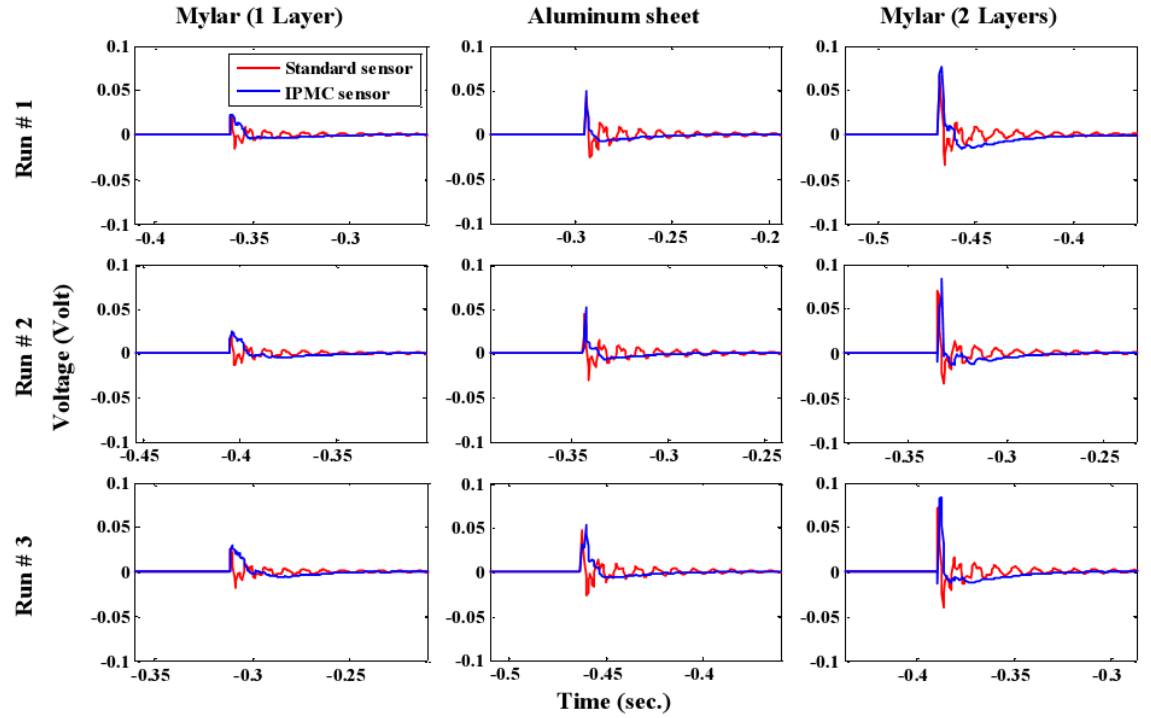

Figure 2.19. Time responses for shear mode sensor 2

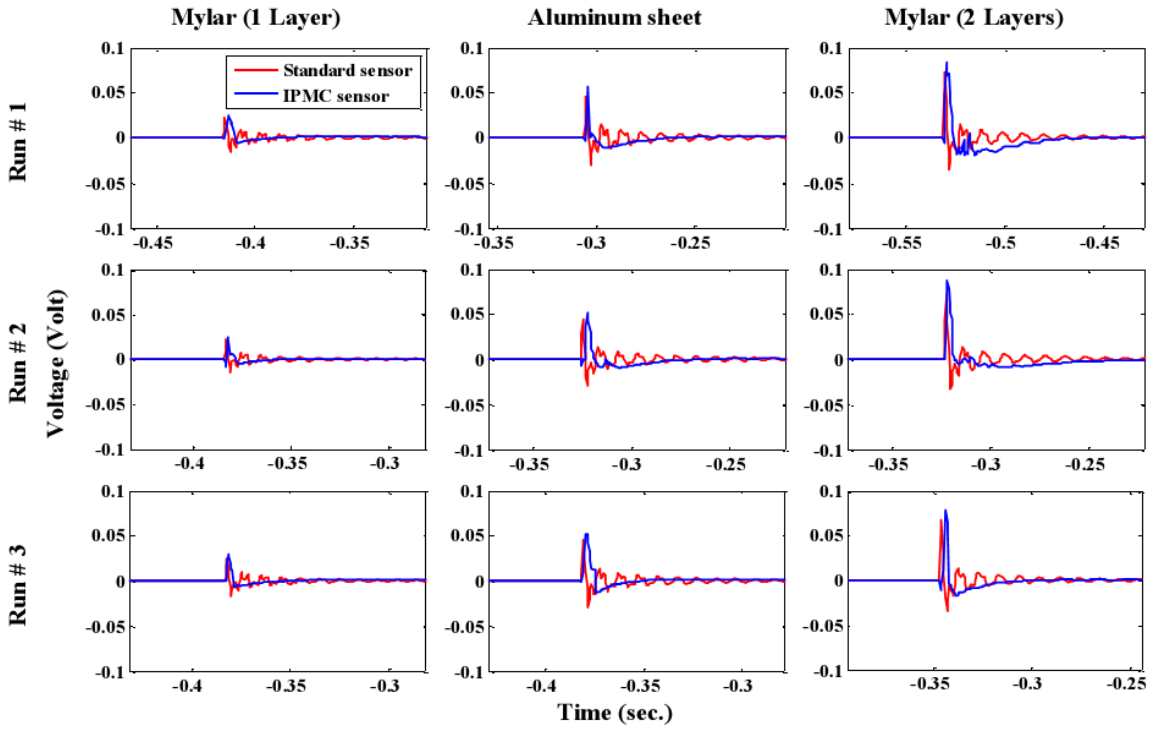

Figure 2.20. Time responses for shear mode sensor 3

Table 2.2. Bending mode's peak pressure data

Sensor #	Membrane/Layer(s)	IPMC sensor voltage (mV)	Standard sensor voltage (mV)	Pressure (kPa)	IPMC's generated charge (nC)
Sensor 1	Maylar/1	20.1	21.3	21.3	20.1
		18.5	19.5	19.5	18.5
		21.2	19.8	19.8	21.2
	Aluminum sheet	43.6	40.5	40.5	43.6
		45.1	44.6	44.6	45.1
		43.8	43.1	43.1	43.8
	Maylar/2	74.0	74.4	74.4	74.0
		75.0	74.2	74.2	75.0
		71.5	69.6	69.6	71.5
Sensor 2	Maylar/1	23.4	23.3	23.3	23.4
		24.2	22.7	22.7	24.2
		20.2	19.7	19.7	20.2
	Aluminum sheet	42.3	43.8	43.8	42.3
		42.5	42.5	42.5	42.5
		45.1	42.4	42.4	45.1
	Maylar/2	74.2	75.1	75.1	74.2
		69.9	70.5	70.5	69.9
		73.2	74.5	74.5	73.2
Sensor 3	Maylar/1	21.5	21.3	21.3	21.5
		26.2	25.5	25.5	26.2
		23.0	22.4	22.4	23.0
	Aluminum sheet	45.3	44.3	44.3	45.3
		42.9	42.4	42.4	42.9
		44.1	45.5	45.5	44.1
	Maylar/2	76.8	74.4	74.4	76.8
		69.0	70.0	70.0	69.0
		71.8	69.6	69.6	71.8

Table 2.3. Compression mode's peak pressure data

Sensor #	Membrane/Layer(s)	IPMC sensor voltage (mV)	Standard sensor voltage (mV)	Pressure (kPa)	IPMC's generated charge (nC)
Sensor 1	Maylar/1	13.91	22.91	22.91	13.91
		13.15	21.61	21.61	13.15
		11.18	18.52	18.52	11.18
	Aluminum sheet	26.63	45.77	45.77	26.63
		27.75	43.93	43.93	27.75
		28.24	47.73	47.73	28.24
	Maylar/2	52.67	85.11	85.11	52.67
		40.29	66.53	66.53	40.29
		43.68	70.38	70.38	43.68
Sensor 2	Maylar/1	10.71	20.70	20.70	10.71
		14.58	23.73	23.73	14.58
		15.24	25.27	25.27	15.24
	Aluminum sheet	25.45	42.29	42.29	25.45
		25.13	40.57	40.57	25.13
		27.35	44.71	44.71	27.35
	Maylar/2	42.21	70.88	70.88	42.21
		50.34	83.28	83.28	50.34
		42.19	70.56	70.56	42.19
Sensor 3	Maylar/1	10.67	19.55	19.55	10.67
		14.24	23.11	23.11	14.24
		12.97	22.03	22.03	12.97
	Aluminum sheet	28.82	50.02	50.02	28.82
		27.04	44.93	44.93	27.04
		26.92	40.87	40.87	26.92
	Maylar/2	51.82	78.42	78.42	51.82
		45.08	73.92	73.92	45.08
		57.36	91.01	91.01	57.36

Table 2.4. Shear mode's peak pressure data

Sensor #	Membrane/Layer(s)	IPMC sensor voltage (mV)	Standard sensor voltage (mV)	Pressure (kPa)	IPMC's generated charge (nC)
Sensor 1	Maylar/1	25.22	19.16	19.16	25.22
		31.61	26.38	26.38	31.61
		27.20	24.26	24.26	27.20
	Aluminum sheet	50.48	45.13	45.13	50.48
		52.34	44.25	44.25	52.34
		50.53	45.47	45.47	50.53
	Maylar/2	85.01	74.73	74.73	85.01
		81.90	71.84	71.84	81.90
		81.11	71.89	71.89	81.11
Sensor 2	Maylar/1	21.91	20.71	20.71	21.91
		24.16	21.35	21.35	24.16
		29.21	26.14	26.14	29.21
	Aluminum sheet	49.18	43.17	43.17	49.18
		51.64	44.71	44.71	51.64
		53.32	46.43	46.43	53.32
	Maylar/2	76.23	65.91	65.91	76.23
		84.41	69.84	69.84	84.41
		83.50	72.13	72.13	83.50
Sensor 3	Maylar/1	25.18	22.17	22.17	25.18
		29.14	24.20	24.20	29.14
		38.23	21.86	21.86	38.23
	Aluminum sheet	55.91	45.81	45.81	55.91
		51.92	43.80	43.80	51.92
		51.37	45.06	45.06	51.37
	Maylar/2	84.42	71.91	71.91	84.42
		86.83	72.40	72.40	86.83
		78.10	67.04	67.04	78.10

Sensitivity calibration curve shows generated charge magnitudes with respect to reference pressures for all tests, measured by the standard sensor (PCB116B02 with the sensitivity of 0.7978 pC/kPa) which is connected to Kistler 5010B charge amplifier with a total amplification 1000 kPa/V in the performed experiments. Figure 2.21, Figure 2.22 and Figure 2.23 illustrate the calibration curves for fabricated bending mode, compression mode and shear mode sensors, respectively.

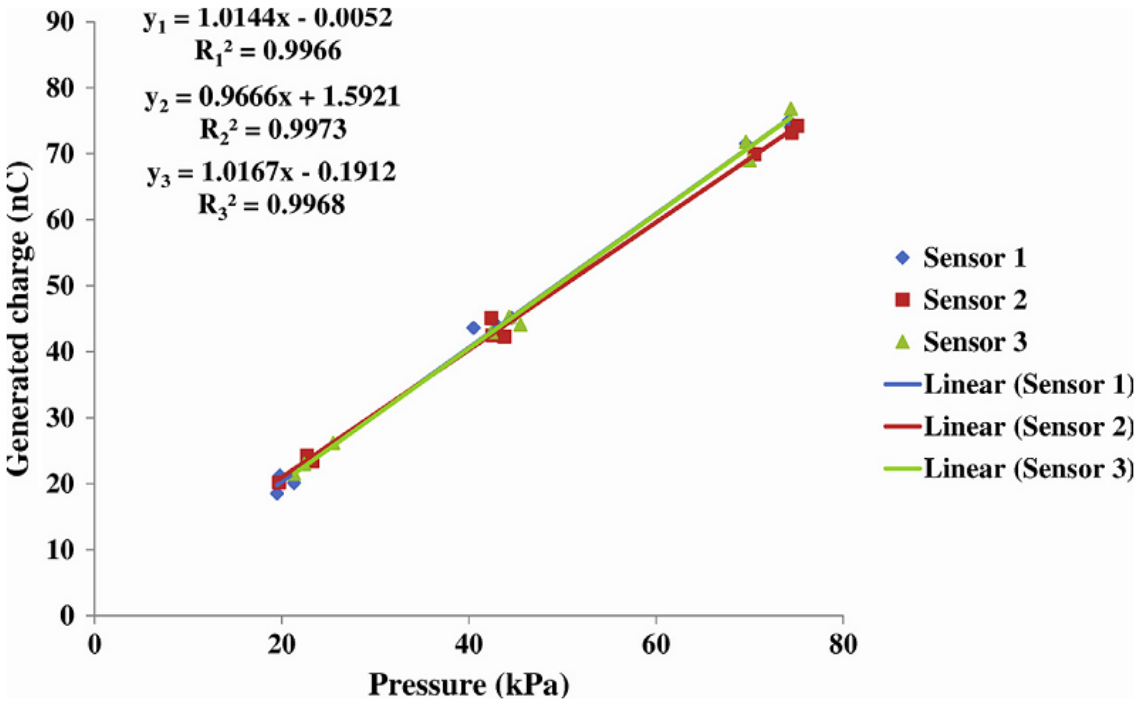

Figure 2.21. Calibration curves of three IPMC bending mode sensors and linear fitting equations

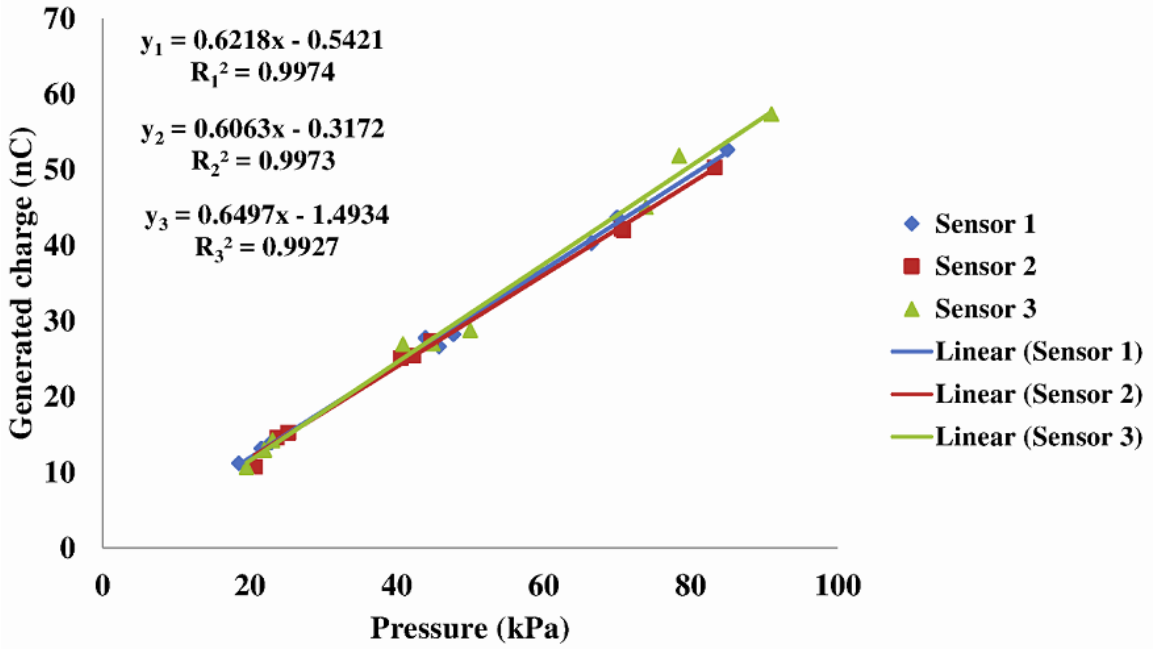

Figure 2.22. Calibration curves of three IPMC compression mode sensors and linear fitting equations

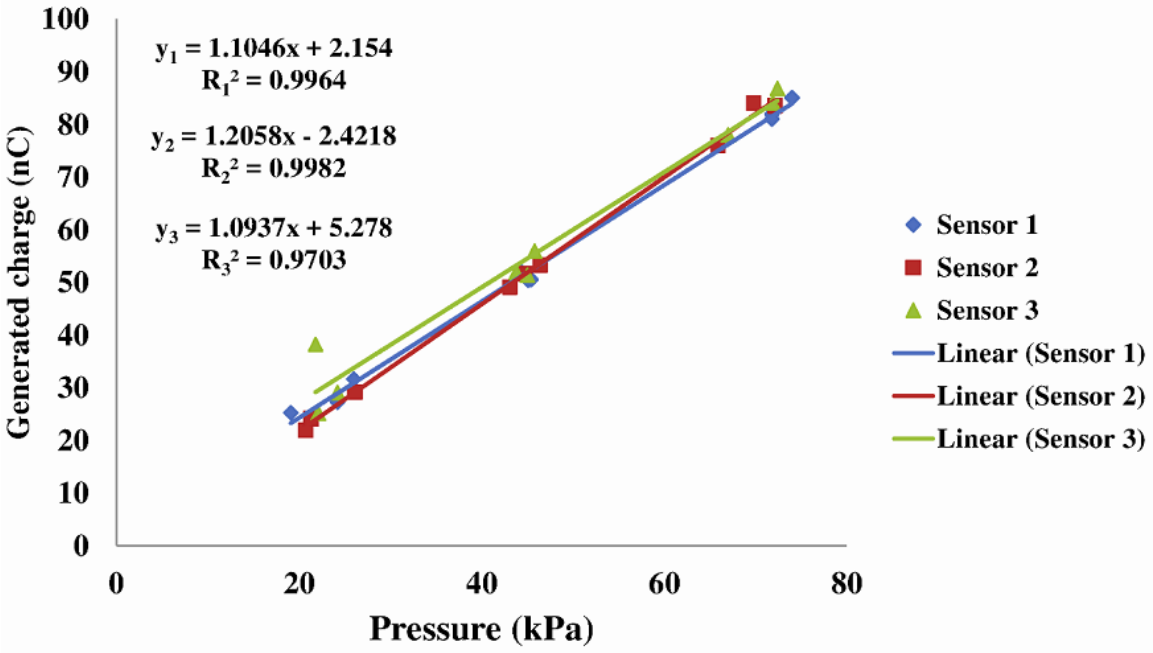

Figure 2.23. Calibration curves of three IPMC shear mode sensors and linear fitting equations

The most important features that should be investigated about a new sensor design are linearity, sensitivity and reliability of the sensor and consistency of the fabrication process. For a sensor, having a linear response is favorable and the set of collected peaks is expected to have a linear correlation, then for each sensor a linear regression model was fitted using the least squares approach to get the slope between generated charge (C) and applied pressure (kPa) which is actually defined as the sensitivity of each pressure sensor. As can be seen in Figure 2.21, Figure 2.22 and Figure 2.23, all correlation coefficients R_1, R_2 and R_3 for each sensor type are close enough to 1 to be able to consider the responses as linear ones with a high accuracy in the measured range.

Furthermore, the sensitivities of three tested bending mode pressure sensors are 1.01 nC/kPa, 0.97 nC/kPa and 1.02 nC/kPa, respectively, that are more than 1000 times higher than the commercial pressure sensor (PCB116B02 with the sensitivity of 0.7978 pC/kPa) which was used

for comparison purpose. Likewise, the sensitivities of three tested compression mode pressure sensors are 0.622 nC/kPa, 0.606 nC/kPa and 0.650 nC/kPa, respectively, that are around 800 times higher than the utilized commercial pressure sensor, and the sensitivities of three tested shear mode pressure sensors are 1.105 nC/kPa, 1.206 nC/kPa and 1.094 nC/kPa, respectively, which are around 1300 times higher than PCB116B02. Different pressure areas and higher sensitivity of IPMC than piezoelectric materials are two main reasons can justify these huge differences. Next observation to point out is that IPMC sensors have a higher sensitivity in shear mode than in bending mode by a factor of 1.3 and they have a higher sensitivity in bending mode than in compression mode by a factor of 1.25. Note that the pressure areas for three designs are the same and IPMCs have the same surfaces, then for similar membranes almost equal forces are applied on IPMCs and different sensitivities are only originated from different modes of deformation. In other words, although shear mode design is more complicated than the bending and compression mode ones it offers a higher sensitivity and a greater mechanical isolation from base bending.

Reliability is one of the key challenges and priorities in sensor technology. In the performed experiment, each sensor has been exposed to the pressure wave of each membrane, which leads to close pressure waves, three times. As can be seen in the measured data, generated charges for close pressures are close that shows the reliability of IPMC pressure sensors. Finally, the slopes of fitted linear regressions illustrate that sensitivities are precisely the same for all three sensors of each type. This observation shows that DAP is a consistent fabrication process for IPMC transducers in different modes and can be hired to make several consistent samples [58, 59].

3.0 IONIC POLYMER-METAL COMPOSITE (IPMC) PRESSURE SENSOR MODELING

According to the literature review, although a couple of models have been developed for IPMC sensors which are useful for basic loads there is a gap for quantitative accurate models that are derived for specific applications. The aim of this chapter is to develop an explicit, dynamic, physics-based, rational transfer function for IPMC pressure sensors in compression, shear and bending modes that could be used in for real-time applications. The main advantage of this model is being a combination of physics-based models and simple models. As a physical model, it provides a valuable insight into the sensing mechanism of IPMCs; and as a transfer function is suitable for analysis and design of system-theoretic tools. This work extends previous studies in two main aspects: it solves the problem due to an external pressure stimulation that makes the model appropriate for pressure sensors; unlike the previous studies, compression, shear and bending modes for arbitrary geometries are considered for IPMCs. Some experiments are done to validate the proposed dynamic model for IPMC pressure sensors. Direct assembly process (DAP) is hired for the fabrication process of the proposed IPMC pressure sensors and impulse stimulation is applied by utilizing a standard shock pressure tube setup. Finally, the time responses of three types of fabricated pressure sensors subjected to different pressures are presented and compared to results obtained from derived transfer functions and the frequency response of transfer functions

are discussed. The results show a good agreement between the measured sensing responses and the model predictions.

3.1 MODEL DEVELOPMENT

Following the procedure which is presented in [44], it is assumed that the charge density at the boundary is proportional to the induced stress field ($\boldsymbol{\sigma}$) within an IPMC membrane,

$$\begin{aligned} \boldsymbol{\sigma} &= -k_0 \rho \mathbf{1}, \\ \rho &= (C^+ - C^-)F, \end{aligned} \tag{3.1}$$

where k_0 is a constant, $\mathbf{1}$ is the identity tensor, ρ is the charge density, C^+ and C^- are the positive and negative ion densities (mol/m^3), respectively, and F is Faraday's constant. There are following relations among **D**, **E**, and ϕ which are the electric displacement, the electric field, and the electric potential, respectively,

$$\begin{aligned} \mathbf{E} &= \frac{\mathbf{D}}{\kappa_e} = -\nabla\phi, \\ \nabla.\mathbf{D} &= \rho = F(C^+ - C^-), \end{aligned} \tag{3.2}$$

where κ_e is the effective dielectric constant of the polymer. The continuity expression that relates the ion flux vector **J** to C^+ is

$$\nabla.\mathbf{J} = -\frac{\partial C^+}{\partial t}. \tag{3.3}$$

The thickness of an IPMC is much smaller than the other dimensions, then it can be assumed that **D**, **E** and **J** are all functions of the thickness (z −direction). Therefore, the boldface notation for these variables could be dropped, and the ion flux includes diffusion, migration and convection terms,

$$J = -d\left(\nabla C^{+} + \frac{C^{+}F}{RT}\nabla\phi + \frac{C^{+}\Delta V}{RT}\nabla p\right) + C^{+}v, \tag{3.4}$$

where d is the ionic diffusivity, R is the gas constant, T is the absolute temperature, p is the fluid pressure, v the free solvent velocity field and

$$\Delta V = M^{+}\left(\frac{V^{+}}{M^{+}} - \frac{V^{w}}{M^{w}}\right), \tag{3.5}$$

in which V^{+} and V^{w} are partial molar volumes of the cation and diluent, respectively, and M^{+} and M^{w} are the corresponding molar weights. From the second equation of (3.1), C^{+} can be written as

$$C^{+} = \frac{1}{F}\rho + C^{-}, \tag{3.6}$$

where C^{-} is homogeneous in space and time-invariant since anions are fixed to the polymer backbone. Taking the gradient with respect to z on both sides of (3.6) and using (3.2), results in,

$$\nabla C^{+} = \frac{\kappa_e}{F}\nabla^2 E. \tag{3.7}$$

Applying Darcy's Law to relate the fluid velocity v to the pressure gradient ∇p [60], results in

$$v = k'(C^{-}FE - \nabla p), \tag{3.8}$$

where k' is the hydraulic permeability coefficient. Neglecting the convection term [46], $v = 0$, leads to

$$\nabla p = C^{-}FE. \tag{3.9}$$

Substituting (3.7), (3.8) and (3.9) into the original ion flux equation (3.4) and using $\nabla\phi = -E$, J could be written as

$$J = -d\left(\frac{\kappa_e}{F}\nabla^2 E - \frac{\kappa_e(1 - C^{-}\Delta V)}{RT}\nabla E.E - \frac{FC^{-}(1 - C^{-}\Delta V)}{RT}E\right). \tag{3.10}$$

Assuming $\kappa_e \nabla E \ll C^- F$, the nonlinear term involving $\nabla E.E$ in (3.10) is dropped [42], resulting in

$$J = -d\left(\frac{\kappa_e}{F}\nabla^2 E - \frac{FC^-}{RT}(1 - C^-\Delta V)E\right). \tag{3.11}$$

And,

$$\frac{\partial C^+}{\partial t} = \frac{1}{F}\frac{\partial \rho}{\partial t} = \frac{\kappa_e}{F}\frac{\partial(\nabla E)}{\partial t} = \frac{\kappa_e}{F}\frac{\partial^2 E}{\partial z \partial t}, \tag{3.12}$$

and using (3.3), the following equation which is involving E is obtained,

$$\frac{\kappa_e}{F}\frac{\partial^2 E}{\partial z \partial t} = d\left(\frac{\kappa_e}{F}\frac{\partial^3 E}{\partial z^3} - \frac{FC^-}{RT}(1 - C^-\Delta V)\frac{\partial E}{\partial z}\right), \tag{3.13}$$

and also, can be expressed in terms of $\rho = \kappa_e \nabla E = \kappa_e \frac{\partial E}{\partial z}$:

$$\frac{\partial \rho}{\partial t} - d\frac{\partial^2 \rho}{\partial z^2} + \frac{F^2 dC^-}{\kappa_e RT}(1 - C^-\Delta V)\rho = 0, \tag{3.14}$$

which is the governing PDE for the charge density ρ inside the polymer. Note that a key assumption in this approach is the proportionality of the initial charge density at any point on the IPMC surface to the induced stress at the same point [46, 47]. This assumption, which is being utilized as an initial/boundary condition for (3.14), is made based upon the similar assumption used in modeling the actuation response of IPMCs [44], and that IPMCs demonstrate reciprocity between sensing and actuation [17].

The objective of this paper is to derive a sensing model for IPMC pressure sensors in compression, shear and bending modes. The model is based on the exact solution to (3.14) subject to appropriate boundary conditions, which is made possible by converting it to the Laplace domain. Note that only small deflections of the IPMCs are considered in this paper, where one can ignore the nonlinearity of stress profile as well as the surface resistance variation due to deformation [61].

In the following three sub-sections transfer functions for circular, rectangular and circular IPMCs in compression, shear and bending modes will be developed, respectively. The response of theses transfer functions, after reduction, could be compared to the ones from fabricated IPMC pressure sensors.

3.1.1 Compression mode

Consider Figure 3.1, where the circular IPMC is located on a rigid substrate and is subject to an external uniformly distributed pressure $P_0(t)$. The mid-surface of the membrane is denoted by $z = 0$, and the upper and lower surfaces are denoted by $z = h/2$ and $z = -h/2$, respectively. To ease the presentation, define the aggregated constant

$$K = \frac{F^2 dC^-}{\kappa_e RT}(1 - C^-\Delta V). \tag{3.15}$$

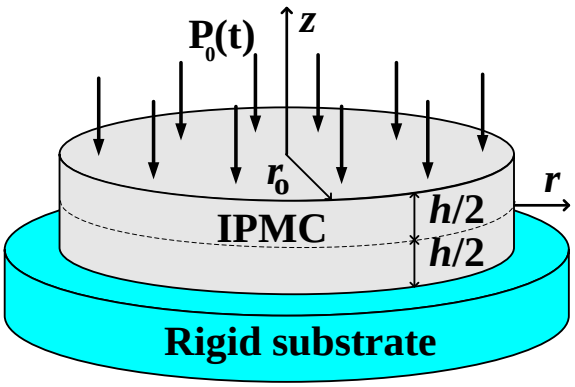

Figure 3.1. Schematic view of circular IPMC under compression.

Performing a Laplace transform for the time variable of $\rho(z,t)$ and rearranging, (3.14) is converted into,

$$\frac{\partial^2 \rho(z,s)}{\partial z^2} = \frac{(s+K)}{d}\rho(z,s), \tag{3.16}$$

where s is the Laplace variable. By defining $\beta(s)$ such that $\beta^2(s) = \frac{s+K}{d}$, a generic solution to (3.16) is obtained as

$$\rho(z,s) = c_1^c(s)e^{-\beta(s)z} + c_2^c(s)e^{\beta(s)z}, \tag{3.17}$$

for some appropriate functions $c_1^c(s)$ and $c_2^c(s)$. An assumption, analogous to the one in [46], will be made to determine $c_1^c(s)$ and $c_2^c(s)$. In particular, it is assumed that top and bottom surfaces are only experiencing compression, then by multiplying both sides of first equation of (3.1) by $[1 \quad 0 \quad 0]$ and $[1 \quad 0 \quad 0]^{\mathrm{T}}$ from left and right sides, respectively,

$$\sigma(\pm h/2, s) = k_0^c \rho(\pm h/2, s), \tag{3.18}$$

where k_0^c is the charge-stress coupling constant for compression mode. From $\sigma(h/2,s) = \sigma(-h/2,s)$, one gets

$$\rho(h/2,s) = \rho(-h/2,s), \tag{3.19}$$

which implies $c_1^c(s) = c_2^c(s)$ and thus

$$\rho(z,s) = 2c_1^c(s)\cosh(\beta(s)z), \tag{3.20}$$

where $\rho(h/2,s) = P_0(s)/k_0^c$. And, $c_1^c(s)$ will be as,

$$c_1^c(s) = \frac{P_0(s)}{2k_0^c \cosh\left(\frac{\beta(s)h}{2}\right)}. \tag{3.21}$$

Using (3.17) and the field equations (3.2), one can derive the expressions for the electric field E and then for the electric potential ϕ in the Laplace domain:

$$\begin{aligned} E(z,s) &= 2c_1^c(s)\frac{\sinh(\beta(s)z)}{\kappa_e \beta(s)} + a_1^c(s), \\ \phi(z,s) &= -2c_1^c(s)\frac{\cosh(\beta(s)z)}{\kappa_e \beta^2(s)} - a_1^c(s)z + a_2^c(s), \end{aligned} \tag{3.22}$$

where $a_1^c(s)$ and $a_2^c(s)$ are appropriate functions to be determined based on boundary conditions on ϕ. In the short-circuit current (or charge) sensing mode, the electric potential is uniform across both surfaces $z = \pm h/2$, and without loss of generality, the potential is set to be zero:

$$\phi(h/2, s) = \phi(-h/2, s) = 0. \tag{3.23}$$

Combining (3.22) with (3.23), one can solve for $a_1^c(s)$ and $a_2^c(s)$:

$$a_1^c(s) = 0,$$
$$a_2^c(s) = 2c_1^c(s)\frac{\cosh\left(\frac{\beta(s)h}{2}\right)}{\kappa_e \beta^2(s)}. \tag{3.24}$$

The total induced sensing charge is obtained by integrating the electrical displacement D on the boundary $z = \pm h/2$:

$$Q_c(s) = \int_{A_s} D(\pm h/2, s)dA = \int_{A_s} \kappa_e E(\pm h/2, s)dA. \tag{3.25}$$

Combining (3.21), (3.22), (3.24) and (3.25), $Q_c(s)$, which is linear with respect to the external pressure $P_0(s)$, could be derived,

$$Q_c(s) = \frac{\pi r_o^2 \beta(s)\tanh(\beta(s)h/2)}{k_0^c \beta^2(s)} P_0(s). \tag{3.26}$$

The transfer function from the applied pressure $P_0(s)$ to the sensing output $Q_c(s)$ for an IPMC under compression is

$$H_c(s) = \frac{\pi r_o^2 \beta(s)\tanh(\beta(s)h/2)}{k_0^c \beta^2(s)}. \tag{3.27}$$

3.1.2 Shear mode

Consider Figure 3.2, where a rectangular IPMC is subject to an external uniformly distributed shear stress which is equal to pressure $P_0(t)$. The mid-surface of the membrane is denoted by $z = 0$, and the upper and lower surfaces are denoted by $x = h/2$ and $x = -h/2$, respectively. Using constant K which is defined in (3.15), performing a Laplace transform and rearranging, (3.14) becomes

$$\frac{\partial^2 \rho(z,s)}{\partial z^2} = \frac{(s+K)}{d}\rho(z,s), \tag{3.28}$$

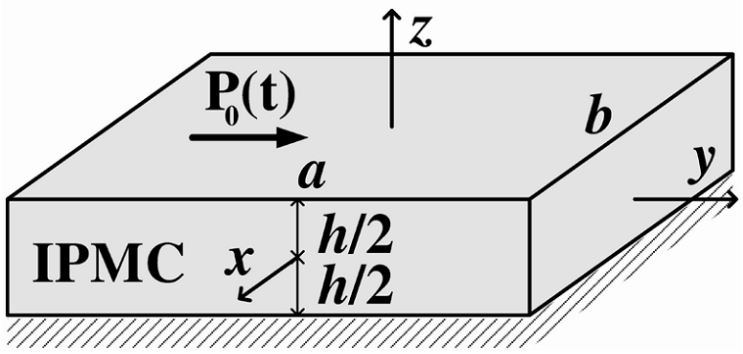

Figure 3.2. Schematic view of rectangular IPMC under shear.

with the solution as

$$\rho(z,s) = c_1^s(s)e^{-\beta(s)z} + c_2^s(s)e^{\beta(s)z}, \tag{3.29}$$

for some appropriate functions $c_1^s(s)$ and $c_2^s(s)$. In particular, it is assumed that top and bottom surfaces are experiencing only shear stresses, then by calculating Eigen stress matrix and multiplying both sides of (3.1) by $[1 \quad 0 \quad 0]$ and $[1 \quad 0 \quad 0]^{\mathrm{T}}$ from left and right, respectively, one will get

$$\sigma(\pm h/2, s) = k_0^s \rho(\pm h/2, s), \tag{3.30}$$

where k_0^s is the charge-stress coupling constant for shear mode. From $\sigma(h/2, s) = \sigma(-h/2, s)$, one gets

$$\rho(h/2, s) = \rho(-h/2, s), \tag{3.31}$$

which implies $c_1^s(s) = c_2^s(s)$ and thus

$$\rho(z, s) = 2c_1^s(s)\cosh(\beta(s)z), \tag{3.32}$$

where $\rho(h/2, s) = P_0(s)/k_0^s$. And then $c_1^s(s)$ will be as

$$c_1^s(s) = \frac{P_0(s)}{2k_0^s \cosh\left(\frac{\beta(s)h}{2}\right)}. \tag{3.33}$$

Using (3.29) and the field equations (3.2), the expressions for the electric field E and the electric potential ϕ in the Laplace domain will be:

$$\begin{aligned} E(z, s) &= 2c_1^s(s)\frac{\sinh(\beta(s)z)}{\kappa_e \beta(s)} + a_1^s(s), \\ \phi(z, s) &= -2c_1^s(s)\frac{\cosh(\beta(s)z)}{\kappa_e \beta^2(s)} - a_1^s(s)z + a_2^s(s), \end{aligned} \tag{3.34}$$

where $a_1^s(s)$ and $a_2^s(s)$ are appropriate functions to be determined based on boundary conditions on ϕ. By setting the electric potential equal zero for both surfaces $z = \pm h/2$,

$$\phi(h/2, s) = \phi(-h/2, s) = 0, \tag{3.35}$$

and combining (3.34) with (3.35), $a_1^s(s)$ and $a_2^s(s)$ are obtained as:

$$\begin{aligned} a_1^s(s) &= 0, \\ a_2^s(s) &= 2c_1^s(s)\frac{\cosh\left(\frac{\beta(s)h}{2}\right)}{\kappa_e \beta^2(s)}. \end{aligned} \tag{3.36}$$

The total induced sensing charge is obtained by integrating the electrical displacement D on the boundary $z = \pm h/2$:

$$Q_s(s) = \int_{A_s} D(\pm h/2, s)dA = \int_{A_s} \kappa_e E(\pm h/2, s)dA. \tag{3.37}$$

Combining (3.33), (3.34), (3.36) and (3.37), one can derive $Q_c(s)$, which is linear with respect to the external pressure $P_0(s)$:

$$Q_s(s) = \frac{ab\beta(s)\tanh(\beta(s)h/2)}{k_0^s\beta^2(s)}P_0(s). \tag{3.38}$$

The transfer function from the applied pressure $P_0(s)$ to the sensing output $Q_s(s)$ for shear mode IPMC is then derived as

$$H_s(s) = \frac{ab\beta(s)\tanh(\beta(s)h/2)}{k_0^s\beta^2(s)}. \tag{3.39}$$

3.1.3 Bending mode

Consider Figure 3.3, where the circular IPMC sensor under the external pressure $P_0(t)$ can be considered as a uniformly loaded plate with clamped edge with radius r_o and thickness h. The clamped edge boundary conditions can be defined as,

$$\begin{aligned}
&\sigma_z(r, z = -h/2) = 0,\\
&\sigma_z(r, z = h/2) = -P_0,\\
&\tau_{rz}(r, z = \pm h/2) = 0,\\
&u(r = r_o, z = 0) = v(r = r_o, z = 0) = \frac{\partial w(r = r_o, z = 0)}{\partial r} = 0,
\end{aligned} \tag{3.40}$$

where σ_z and τ_{rz} are normal and shear stresses, respectively, u, v and w are the displacements in $x-$, $y-$ and $z-$directions, respectively.

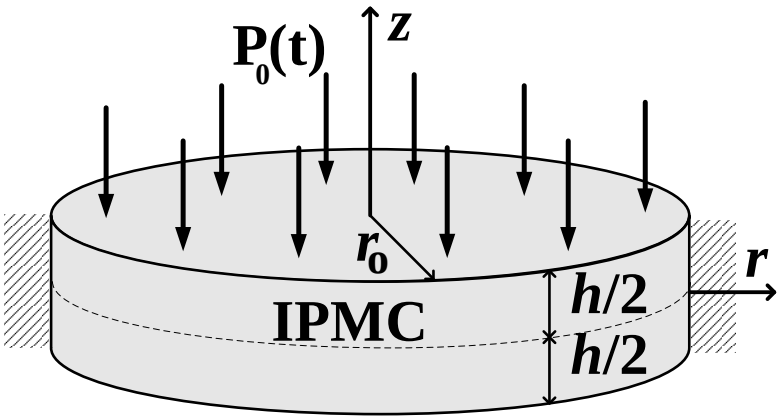

Figure 3.3. Schematic view of circular IPMC under bending.

By solving the problem, the expressions of stress components will be as [62]

$$\sigma_z(r,z) = P_0\left(-2\frac{z^3}{h^3}+\frac{3}{2}\frac{b^2 z}{h^3}-\frac{1}{2}\right),$$

$$\tau_{rz}(r,z) = 3P_0\frac{r}{h}\left(\frac{z^2}{h^2}-\frac{1}{4}\right),$$

$$\sigma_r(r,z) = P_0\left\{(2+\nu)\frac{z^3}{h^3}-\frac{3}{4}(3+\nu)\frac{zr^2}{h^3}+\frac{3}{4}\left[(1+\nu)\frac{r_o^2}{h^3}-\frac{2}{(1-\nu)}\frac{1}{h}\right]z - \frac{\nu}{2(1-\nu)}\right\}, \tag{3.41}$$

$$\sigma_\theta(r,z) = P_0\left\{(2+\nu)\frac{z^3}{h^3}-\frac{3}{4}(1+3\nu)\frac{zr^2}{h^3}+\frac{3}{4}\left[(1+\nu)\frac{r_o^2}{h^3}-\frac{2}{(1-\nu)}\frac{1}{h}\right]z - \frac{\nu}{2(1-\nu)}\right\},$$

where ν is Poisson's ratio.

For IPMC's top and bottom surfaces ($z = \pm\frac{h}{2}$) τ_{rz} vanishes and we are only left with σ_r, σ_θ and σ_z stress components. Again, using constant K which is defined in (3.15), performing a Laplace transform and rearranging, (3.14) becomes

$$\frac{\partial^2 \rho(r,z,s)}{\partial z^2} = \frac{(s+K)}{d}\rho(r,z,s). \tag{3.42}$$

Define $\beta(s)$ such that $\beta^2(s) = \frac{s+K}{d}$. A generic solution to (3.42) is obtained as

$$\rho(r,z,s) = c_1^b(r,s)e^{-\beta(s)z} + c_2^b(r,s)e^{\beta(s)z}, \tag{3.43}$$

for some appropriate functions $c_1^b(r,s)$ and $c_2^b(r,s)$. In particular then by multiplying both sides of (3.1) by $[1 \quad 1 \quad 1]$ and $[1 \quad 1 \quad 1]^{\mathrm{T}}$ from left and right, respectively, one will get

$$\sigma_r(r,\pm h/2,s) + \sigma_\theta(r,\pm h/2,s) + \sigma_z(r,\pm h/2,s) = 3k_0^b\rho(r,\pm h/2,s), \tag{3.44}$$

where k_0^b is the charge-stress coupling constant for bending mode. From this fact that the upper surface is under compression and lower surface is experiencing, one gets

$$\rho(r,h/2,s) = -\rho(r,-h/2,s), \tag{3.45}$$

which implies $c_1^b(r,s) = -c_2^b(r,s)$ and thus

$$\rho(r,z,s) = -2c_1^b(r,s)\sinh(\beta(s)z), \tag{3.46}$$

where

$$\rho(r,h/2,s)=P_0(s)\left[\left(-\frac{\nu}{2(1-\nu)}+\frac{2+\nu}{8}-\frac{3(2+\nu)r^2}{8h^2}\right.\right.$$
$$\left.+\frac{3}{8}h\left(-\frac{2}{h(1-\nu)}+\frac{(1+\nu)r_o^2}{h^3}\right)\right)$$
$$+\left(-\frac{\nu}{2(1-\nu)}+\frac{2+\nu}{8}-\frac{3(1+3\nu)r^2}{8h^2}\right. \tag{3.47}$$
$$\left.\left.+\frac{3}{8}h\left(-\frac{2}{h(1-\nu)}+\frac{(1+\nu)r_o^2}{h^3}\right)\right)+\left(-\frac{3}{4}+\frac{3r_o^2}{4h^2}\right)\right]/3.$$

And then $c_1^b(r,s)$ will be as

$$c_1^b(r,s)=-\frac{\rho(r,h/2,s)}{2k_0^b\sinh\left(\frac{\beta(s)h}{2}\right)}. \tag{3.48}$$

Using (3.43) and the field equations (3.2), one can derive the expressions for the electric field E and then for the electric potential ϕ in the Laplace domain:

$$E(r,z,s)=-2c_1^b(r,s)\frac{\cosh(\beta(s)z)}{\kappa_e\beta(s)}+a_1^b(r,s),$$
$$\phi(r,z,s)=2c_1^b(r,s)\frac{\sinh(\beta(s)z)}{\kappa_e\beta^2(s)}-a_1^b(r,s)z+a_2^b(r,s), \tag{3.49}$$

where $a_1^b(r,s)$ and $a_2^b(r,s)$ are appropriate functions to be determined based on boundary conditions on ϕ. Again, by setting the electric potential of both surfaces, $z=\pm h/2$, equal to zero,

$$\phi(r,h/2,s)=\phi(r,-h/2,s)=0, \tag{3.50}$$

and combining (3.49) with (3.50), $a_1^b(r,s)$ and $a_2^b(r,s)$ are:

$$a_1^b(r,s)=4c_1^b(r,s)\frac{\sinh\left(\frac{\beta(s)h}{2}\right)}{h\kappa_e\beta^2(s)}, \tag{3.51}$$
$$a_2^b(r,s)=0.$$

The total induced sensing charge is obtained by integrating the electrical displacement D on the boundaries $z = \pm h/2$:

$$Q_c(s) = \int_{A_s} D(r, \pm h/2, s) dA = \int_{A_s} \kappa_e E(r, \pm h/2, s) dA. \tag{3.52}$$

Combining (3.48), (3.49), (3.51) and (3.52), one can derive $Q_c(s)$, which is linear with respect to the external pressure $P_0(s)$:

$$Q_b(s) = \frac{\pi r_o^2 (h^2(7 + \nu(2 + \nu)) + 3(\nu - 1) r_o^2)(\beta(s) h \coth(\beta(s) h/2) - 2)}{12 k_0^b h^3 \beta^2(s)(\nu - 1)} P_0(s). \tag{3.53}$$

The transfer function from the applied pressure $P_0(s)$ to the sensing output $Q_c(s)$ for bending mode IPMC is then as

$$H_b(s) = \frac{\pi r_o^2 (h^2(7 + \nu(2 + \nu)) + 3(\nu - 1) r_o^2)(\beta(s) h \coth(\beta(s) h/2) - 2)}{12 k_0^b h^3 \beta^2(s)(\nu - 1)}. \tag{3.54}$$

3.1.4 Model reduction

The main reason to develop transfer functions for these types of sensor is their potential use for real-time feedback control. In the case of feedback control, knowing the sensor dynamics is essential to the controller design [63]. And, for pure sensing applications, the knowledge of sensor dynamics allows us to correctly reconstruct the original mechanical stimulus $P_0(s)$ based on the sensor output $Q(s)$, either online or offline.

For practical implementations, the model $H(s)$ needs to be finite dimensional, i.e. being a rational function of s. However, the sensing models derived earlier, $H_c(s)$, $H_s(s)$ and $H_b(s)$, are infinite-dimensional since they involve non-rational functions including $\sinh(\cdot)$, $\cosh(\cdot)$, $\sqrt{\cdot}$, etc. In the following, a simple method for reducing the IPMC sensing models by exploiting specific

properties of hyperbolic functions and knowledge about the range of physical parameters will be discussed. This approach leads to a more compact formula that is valid within the considered frequency range.

Based on the physical parameters (see Table 3.2 in section 3.3), the composite constant $\frac{K}{d}$ is of the order of 10^{12} which implies

$$|\beta(s)| = \left|\frac{s+K}{d}\right| > 10^6, \tag{3.55}$$

for $s = j\,\omega$,where ω denotes the angular frequency of any sinusoidal input. Since the thickness h of an IPMC is typically bigger than $10^{-4}\ m$, it can be seen that

$$|\beta(s)h/2| \gg 10, \tag{3.56}$$

which allows one to make the approximation

$$\tanh(\beta(s)h/2) \approx \coth(\beta(s)h/2) \approx 1. \tag{3.57}$$

One can further approximate $\sqrt{s+K}$ by its Taylor series about $s = 0$. For instance, considering up to the second-order terms results in the following approximation:

$$\sqrt{s+K} = \sqrt{K}\left(1 + \frac{s}{2K} - \frac{s^2}{8K^2}\right). \tag{3.58}$$

Substituting approximated terms in $H_c(s)$, $H_s(s)$ and $H_b(s)$ will result in,

$$\widehat{H}_c(s) = \frac{\pi r_o^2\sqrt{d}\sqrt{K}\left(1 + \frac{s}{2K} - \frac{s^2}{8K^2}\right)}{k_0^c(s+K)},$$

$$\widehat{H}_s(s) = \frac{ab\sqrt{d}\sqrt{K}\left(1 + \frac{s}{2K} - \frac{s^2}{8K^2}\right)}{k_0^s(s+K)}, \tag{3.59}$$

$$\widehat{H}_b(s) = \frac{\pi r_o^2(h^2(7+\nu(2+\nu)) + 3(\nu-1)r_o^2)\left(h\sqrt{d}\sqrt{K}\left(1 + \frac{s}{2K} - \frac{s^2}{8K^2}\right) - 2d\right)}{12k_0^b h^3(\nu-1)(s+K)}.$$

Although $\widehat{H}_c(s)$, $\widehat{H}_s(s)$ and $\widehat{H}_b(s)$ are improper rational functions, the numerator is of a higher order than the denominator, because the inverse dynamics (3.59) will be proper it is not a concern for feedback or sensing applications. Note that reduced models are still physical models and described in terms of fundamental physical parameters and are thus geometrically scalable. This shows the main difference from other low-order, black box models, in which the parameters have no physical meanings and the parameters should get re-identified empirically for every sensor.

3.2 EXPERIMENTAL PROCEDURE

The fabrication process of compression, shear and bending mode IPMC pressure sensors using DAP and collecting their impulse responses using shock tube are the same as presented in section 2.2.

3.3 RESULTS AND DISCUSSIONS

In this section, impulse responses of fabricated compression, shear and bending mode IPMC pressure sensors are obtained experimentally using a standard pressure tube. The obtained results, after calibration with a standard commercial pressure sensor (PCB116B02 with the sensitivity of $0.7978\ pC/kPa$) which is connected to Kistler 5010B charge amplifier with a total amplification $1000\ kPa/V$, are compared to impulse responses of derived rational transfer functions of IPMC pressure sensors in different modes.

For each type of sensation, compression, shear and bending, one IPMC pressure sensor was fabricated. All three sensors have identical electrode material in which RuO_2 and Nafion solution are mixed 42% and 58% by volume, respectively, and the thickness of the electrode mixture is 15 μm on each side of the Nafion 117 membrane. The radius of the fabricated compression mode and bending mode samples are 10 mm but a circle of radius 6.5 mm of them is exposed to the applied pressure and one of the fabricated samples is depicted in Figure 3.4(a) and Figure 3.4(c), respectively. The IPMC layer which is used in shear mode sample is a 3.5×41 mm rectangular which is wrapped around a 6.5 mm diameter circular cylinder, Figure 3.4(b).

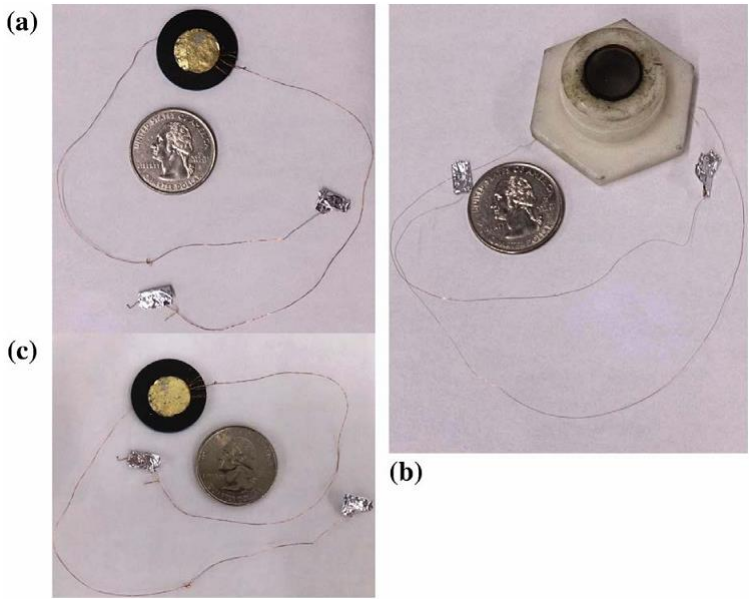

Figure 3.4. Fabricated (a) IPMC compression mode pressure sensor, (b) IPMC shear mode pressure sensor and (c) IPMC bendinf mode pressure sensor using DAP.

Using these dimensions makes surfaces to which the pressure is applied and effective areas of IPMCs equal for three types of sensor and then the comparison of sensitivities which are only functions of deformation is meaningful.

By setting the signal conditioner elements as $R_f = 100\,k\Omega$, $C_f = 1\mu F$, $R_i = 10\,\Omega$ and OP177 which is fed by 9V batteries as the operational amplifier, the amplification magnitude will be 1000 V/C. Each IPMC pressure sensor sample and the standard pressure sensor, PCB116B02, are mounted on the shock tube, 54 mm diameter, at the middle holes, 310 mm distance from the membrane. Three different membranes including single layer Mylar, Aluminum sheet and double layer Mylar have been used in order to produce different shock pressures.

Time responses of three fabricated sensors are depicted in Figure 3.5 and are compared to the standard commercial pressure sensor responses. The peak pressure data for all tests of compression, shear and bending mode sensors are given in Table 3.1. This table contains amplitude of shock wave and corresponding generated charge in IPMC sensors as well as measured output sensors' voltages for different IPMC sensors and membrane layers.

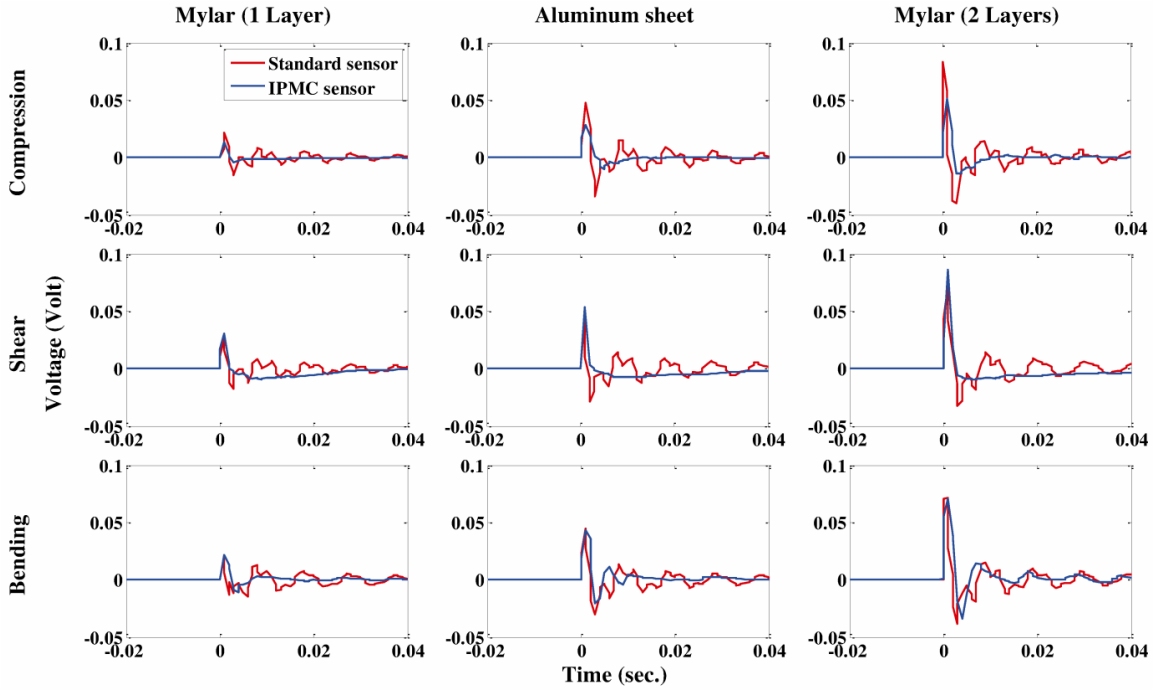

Figure 3.5. Time responses for fabricated compression, shear and bending mode IPMC pressure sensors and standard pressure sensor.

In developed transfer functions, physical parameters of IPMC layers are applied as those given in Table 3.2 [7, 47].

Table 3.1. Peak pressure data

Sensor type	Membrane/Layer(s)	IPMC sensor voltage (mV)	Standard sensor voltage (mV)	Pressure (kPa)	IPMC's generated charge (nC)
Compression	Maylar/1	13.3	21.6	21.6	13.3
	Aluminum sheet	28.6	47.7	47.7	28.6
	Maylar/2	51.1	83.3	83.3	51.1
Shear	Maylar/1	30.8	26.0	26.0	30.8
	Aluminum sheet	53.3	45.1	45.1	53.3
	Maylar/2	86.6	72.4	72.4	86.6
Bending	Maylar/1	21.4	22.0	22.0	21.4
	Aluminum sheet	43.1	45.0	45.0	43.1
	Maylar/2	70.5	71.4	71.4	70.5

Table 3.2. IPMC's physical parameters

Parameter	Magnitude	Dimension
F	96487	$C\ mol^{-1}$
R	8.3143	$mol^{-1}K^{-1}$
T	300	K
Y	5.71×10^{8}	Pa
ν	0.487	$-$
h	200	μm
d	3.32×10^{-11}	$m^2 s^{-1}$
C^-	1091	$mol\ m^{-3}$
κ_e	1.88×10^{-3}	$F\ m^{-3}$

To obtain impulse response of developed transfer functions, the inverse Laplace transforms of transfer functions are calculated by making frequent use of Durbin's numerical inversion formula in the interval [0; 2T] [64, 65]:

$$H(t) = \frac{2e^{\mu t}}{T_0}\left[\frac{1}{2}Re\big(H(\mu)\big) + \sum_{k=1}^{N}\left\{Re\left(H\left(\mu + ik\frac{2\pi}{T_0}\right)\right).\cos\left(kt\frac{2\pi}{T_0}\right) - Im\left(H\left(\mu + ik\frac{2\pi}{T_0}\right)\right).\sin\left(kt\frac{2\pi}{T_0}\right)\right\}\right], \quad (3.60)$$

where μ is an arbitrary real number greater than all the real parts of the singularities of $H(s)$, N is the truncation constant. Furthermore, to obtain stable and convergent results in all cases considered, one may select $N = 500$, $\mu T_o = 7$ with $T_0 = 2t_{max}$, where t_{max} is the maximum calculation time [66].

In dynamic sensing models, some parameters are physical constants and could be substituted in the relation from Table 3.2. But k_0^c, k_0^s and k_0^b need to be identified to get an appropriate magnitude in time response. Comparing time responses of developed transfer functions considering both surfaces to ones measured from fabricated samples, k_0^c, k_0^s and k_0^b are estimated as 725, 375 and 600, respectively. Substituting these parameters in developed transfer functions and applying measured pressures of experiment tests lead to responses which are given in Figure 3.6. This figure compares generated charges for both experimental test and developed model for several shock pressures. As can be seen in Figure 3.6, the developed model predicts the first peak of responses for different modes of deformation subject to different pressures appropriately. While, after the first peak, which is the most important one and from which the applied pressure is estimated, there are some oscillations in experimental measurements, especially for bending mode. The most reasonable explanation for these fluctuations could be the structures' response to applied pressure which is not considered in the model. In other words, each IPMC sensor starts vibrating due to the applied impulse pressure which leads to dynamic stresses on both surfaces and finally

fluctuating response. This dynamic property of sensor's structure is not considered in the developed model [67].

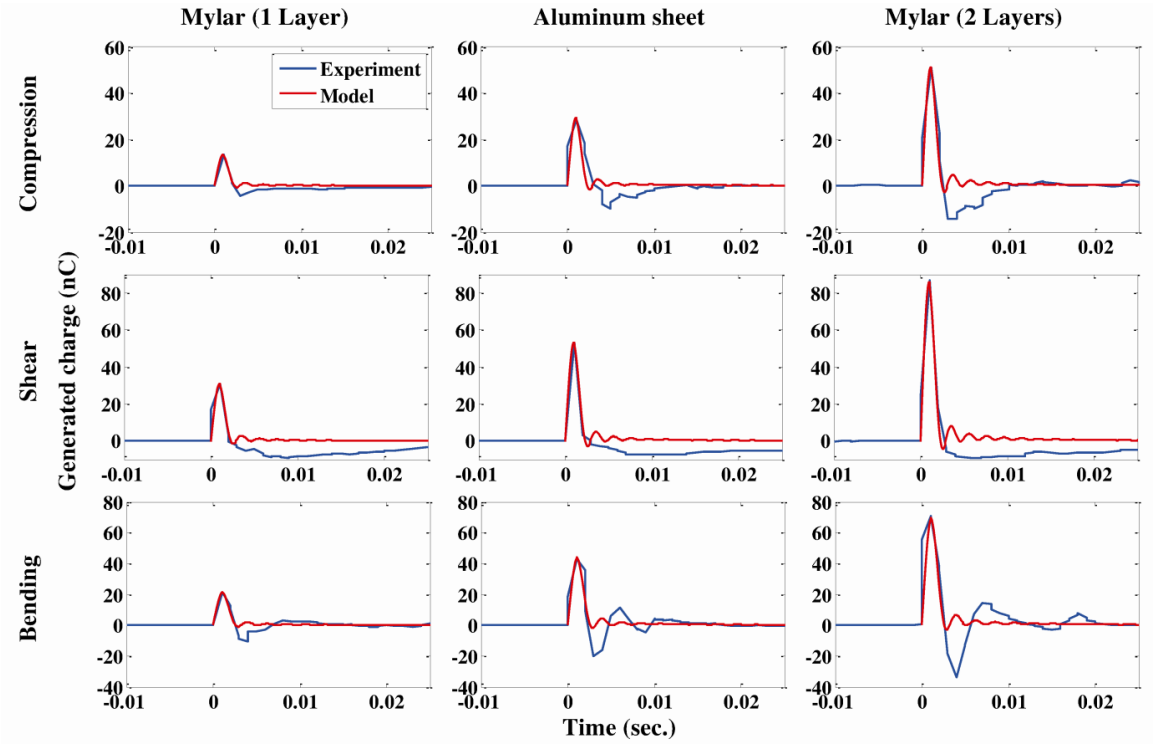

Figure 3.6. Time responses for generated charge of developed models and experimental tests.

Another point to note is that k_0^c, k_0^s and k_0^b have different values which mean that for different modes of deformation different micro-channels are activated in the IPMC and these different mechanisms of charge generations lead to dissimilar sensitivities.

Bode plots of three developed transfer functions for compression, shear and bending mode IPMC pressure sensors are depicted in Figure 3.7, Figure 3.8 and Figure 3.9, respectively, and compared to those obtained from experimental results using fast Fourier transform (FFT). Matlab built-in function of fft(.) has been utilized to calculate the complex frequency response and the

corresponding frequency vector of sensors' time responses. Each frequency response has obtained by averaging each type of sensor's response at different applying pressures and, as it can be seen in Figure 3.7, Figure 3.8 and Figure 3.9, shows a good agreement with the ones from developed transfer functions for both magnitude and phase. Comparing the frequency responses of the proposed model to ones from experiment shows the accuracy of the model not only in the time domain but also in the frequency domain. From the frequency responses, as can be expected, all of them are high-pass filters. In other words, these frequency responses prove experimental observations according to which IPMCs are not useful for static purposes although they are appropriate for being used as dynamical sensors.

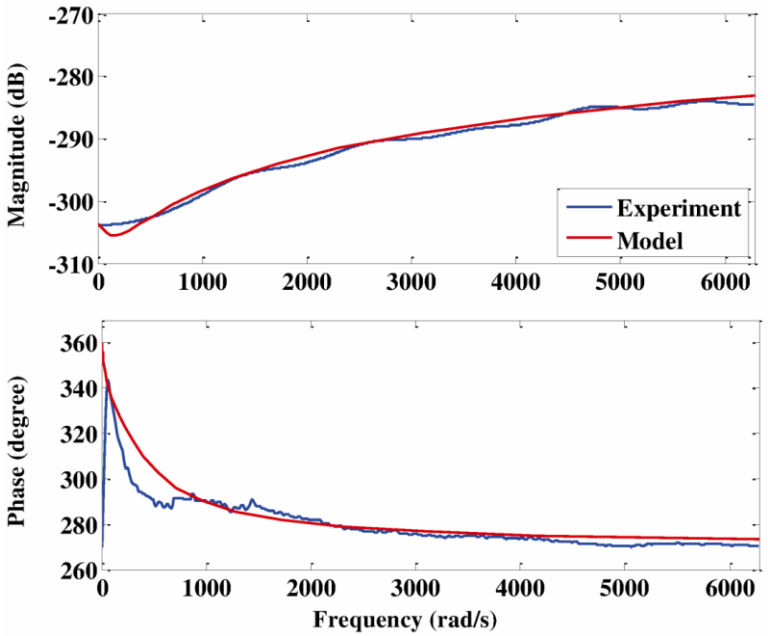

Figure 3.7. Bode plot of the developed transfer function and FFT of the experimental impulse response of compression mode IPMC pressure sensor.

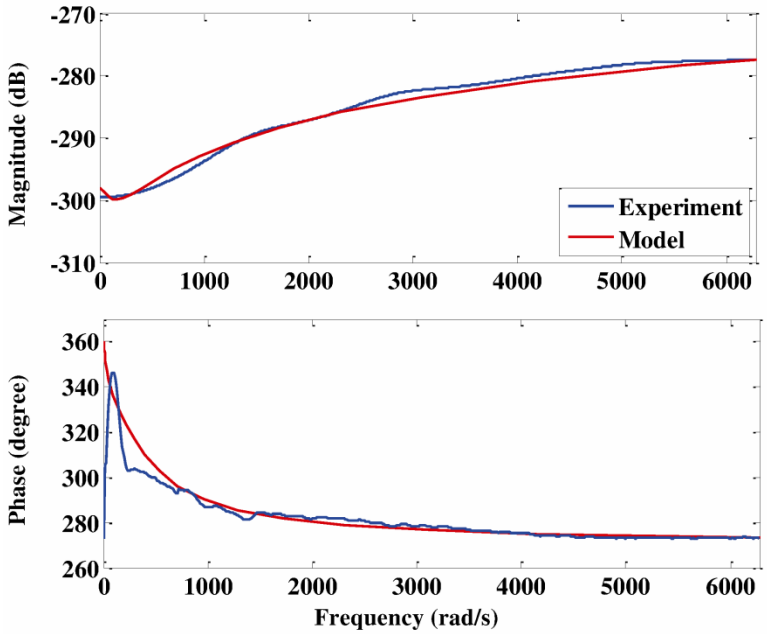

Figure 3.8. Bode plot of the developed transfer function and FFT of the experimental impulse response of shear mode IPMC pressure sensor.

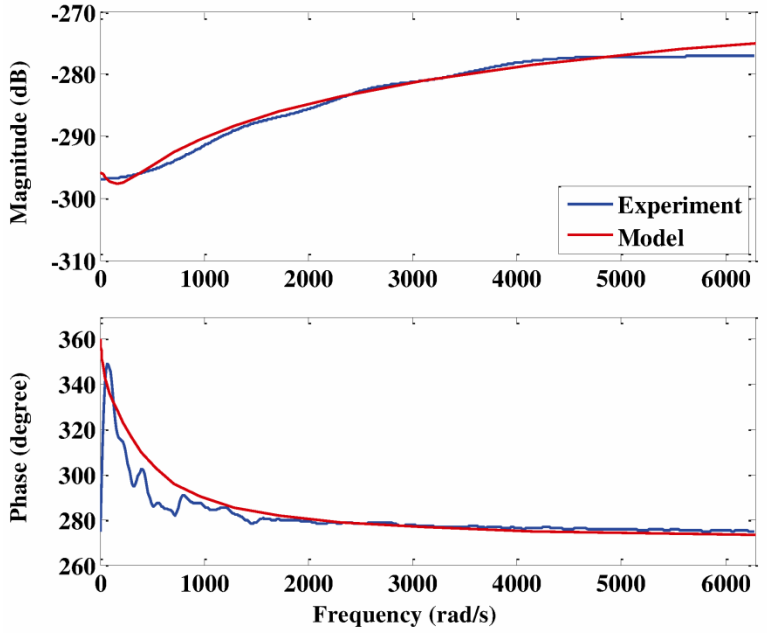

Figure 3.9. Bode plot of the developed transfer function and FFT of the experimental impulse response of bending mode IPMC pressure sensor.

4.0 HIGHLY FLEXIBLE ACRYLIC COATED IONIC POLYMER-METAL COMPOSITES (IPMCS)

Based on the literature review, while there have been many studies on fundamental concepts of IPMC sensors and characterizing the humidity effect, there is a lack of a comprehensive study on the effect of a thin flexible waterproof coating on IPMCs' dynamic sensation. Moreover, some IPMCs' advantages which make them appropriate for being used as dynamical sensors, and popularity of compression and shear mode sensors due to a greater mechanical isolation from base show the importance of a comparative experimental study on the effect of a practical flexible waterproof coating on the dynamic response of IPMCs in all modes of deformation. For this aim, the fabrication process of the proposed waterproof highly flexible IPMC using gold sputter coating and acrylic spraying is presented and the designed frames to stimulate fabricated IPMC segments in compression, bending and shear modes and the procedure of measuring impulse responses using shock tube are explained.

It is worth noting that impulse excitation of IPMC sensors requires a source with a known amplitude of the pressure and a small raise time of the order of 1 ns, that can be easily obtained by utilizing shock pressure tubes. Finally, a couple of impulse excitation tests at several external pressures for both fabricated acrylic coated and uncoated IPMCs in different modes of deformation are conducted to verify how this waterproof coating suppresses the diluent permeation and

maintains the IPMC sensing performance over time. Linearity, sensitivity and reliability of the proposed IPMC sensors will be discussed as well.

4.1 CHARGE GENERATION MECHANISM AND EQUIVALENT CIRCUIT

The streaming potential hypothesis could be hired to explain charge generation mechanisms for compression, bending and shear modes of deformation. These mechanisms are the same as presented in section 2.1.

Again, an IPMC in sensory mode could be modeled as a charge source with a shunt capacitor and resistor and its equivalent resistance and capacitance can be obtained experimentally using an impedance analyzer. A charge amplifier is used to have control on the frequency of operation, signal amplitude and the input impedance of the IPMC sensor. All details are the same as section 2.1.

4.2 FABRICATION PROCESS AND EXPERIMENTAL SETUP

The impregnation reduction technique which is an electroless chemical plating procedure is a commonly used IPMC fabrication method. This approach is popular because it results in effective transduction, but it offers limited control over electrode architecture. Direct assembly process (DAP) is another IPMC fabrication process and although it is able to use any type of ionomer, diluent, conducting powder and to have direct control over the electrode thickness and composition [55], it has several intrinsic drawbacks due to its electrode painting process including low

flexibility and fragility of electrodes. In addition, the main disadvantage of almost all IPMCs is being extremely sensitive to humidity which makes them not appropriate for applicable daily usage.

To tackle the aforementioned problems, gold sputter coating is hired for electrode coating and IPMC segments are acrylic coated to reduce the humidity effect on the IPMC properties. Sputter coating is a sputter deposition process to cover a specimen with a thin layer of conducting material and the advantage is that materials with very high melting points are easily sputtered while evaporation of these materials in a resistance evaporator is problematic or even impossible. Sputtered films typically have a better adhesion on the substrate than painted films which makes the resulted IPMC layer extremely more flexible than the ones made using DAP. For acrylic coating process, commercial Sprayon EL 2000 Clear Acrylic Sealer, applicable for sealing electrical and electronic parts, which dries to a crystal clear flexible and waterproof film, is applied. Due to stability in air and therefore reducing dehydration effects, an ionic liquid, EmI-Tf, was chosen as the diluent [56]. Nafion-117 and lithium are selected as ionomer and counter-ion, respectively. The specific procedure employed to fabricate IPMC pressure sensors could be summarized through following steps:

1. The Nafion membrane is boiled in sulfuric acid (H_2SO_4) 1 M solution for half an hour for cleaning purposes.

2. The cleaned membrane is boiled in metal salt (for example; LiCl) solution for two hours to exchange protons (H^+) with metal cations (for example; Li^+) and then rinsed with deionized (DI) water to remove excess metal salt precipitates.

3. The ion exchanged membrane is boiled in DI water for two hours to be cleaned, and then dried in a 150 °C oven for 12 hours to remove unbound water in the ionomer.

4. The dried Nafion is coated with thin gold electrodes (80-120 nm) using DC sputtering in a sputter coater.

5. The gold electrode coated Nafion is soaked in the ionic liquid, EmI-Tf, for diluent uptake.

6. Finally, a thin film layer of Sprayon EL 2000 Clear Acrylic Sealer is sprayed on the dried electrode-sputtered IPMC membrane.

Capturing impulse responses of fabricated IPMCs are the same as pressure sensors which are presented in section 2.3.

4.3 RESULTS AND DISCUSSIONS

Nafion 117 membrane with the thickness of 170 μm is utilized as the ionic polymer layer. A layer of gold is sputtered on each side of the Nafion after cleaning, proton exchange and drying process using DC sputtering in a sputter coater (Cressington Sputter Coater 108auto). Checking the surface of the gold sputtered polymer using Tencor Alpha-Step IQ surface profiler shows that the thickness of the gold electrode layer is about 100 μm. And, the surface resistance of fabricated IPMC is 0.9 Ω/cm on each surface.

Next, for diluent uptake, the gold electrode coated Nafion is soaked in EmI-Tf. Figure 4.1 shows the experimental results for the diluent uptake process for three gold sputtered IPMC pieces submerged in EmI-Tf baths under 22 °C, 30 °C and 40 °C, respectively. The value of the EmI-Tf content is obtained by weighing each IPMC segment before and after soaking. It can be seen that all three IPMC segments are saturated in the same weight percentage of diluent uptake and increasing the temperature only accelerates this process. The other point to remark is that using

EmI-Tf bath with higher temperatures will lead to delamination of gold layers due to different thermal expansion coefficients of polymer and metal.

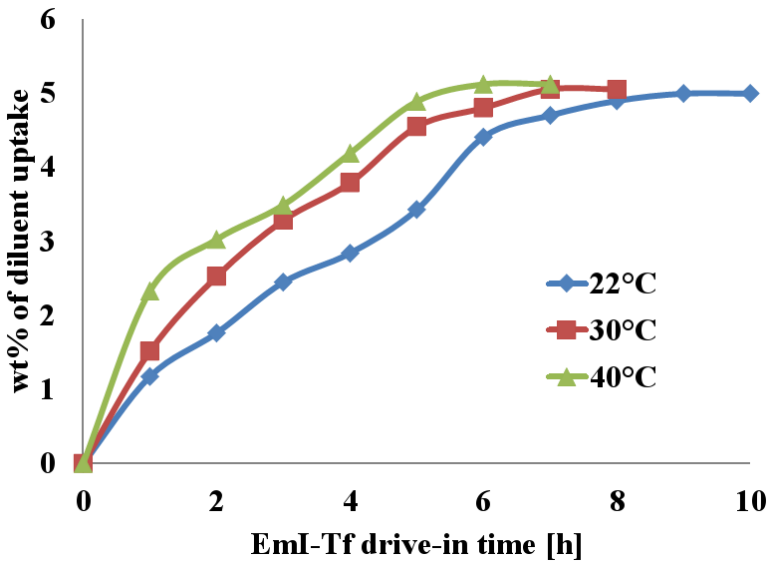

Figure 4.1. Diluent uptake process for gold sputtered IPMC pieces submerged in EmI-Tf baths at different temperatures

For each type of deformation, compression, bending and shear, two IPMC segments with identical electrode materials and thicknesses were fabricated. Compression and bending mode segments are circular with a radius of 10 mm but a circle of radius 6.5 mm of them is exposed to the external pressure from pressure tube. The IPMC layer which is used in shear mode excitations is a 3.5×41 mm rectangle which is wrapped around a 13 mm diameter circular cylinder. Using these dimensions makes surfaces to which the pressure is applied and effective areas of IPMCs equal for all types of sensory mode and accordingly, the comparison of sensitivities which are only functions of deformation becomes meaningful. In order to investigate the effect of acrylic coating, one of the fabricated segments for each mode of deformation is sprayed by Sprayon EL 2000 Clear

Acrylic Sealer which makes them waterproof, and the other one is left naked. Again, using Tencor Alpha-Step IQ surface profiler shows that the thickness of the acrylic coat on the gold sputtered IPMC is about 150 nm. Fabricated IPMC segments before and after mounting on their corresponding frames are depicted in Figure 4.2(a) and Figure 4.2(b), respectively. To study the effect of acrylic coating, impulse response experiments are conducted just after fabrication, 3 days after fabrication and 6 days after fabrication of IPMCs for both groups of acrylic coated and naked segments using the standard shock tube. The laboratory's controlled temperature and humidity for all experiments were 22 °C and 50%, respectively.

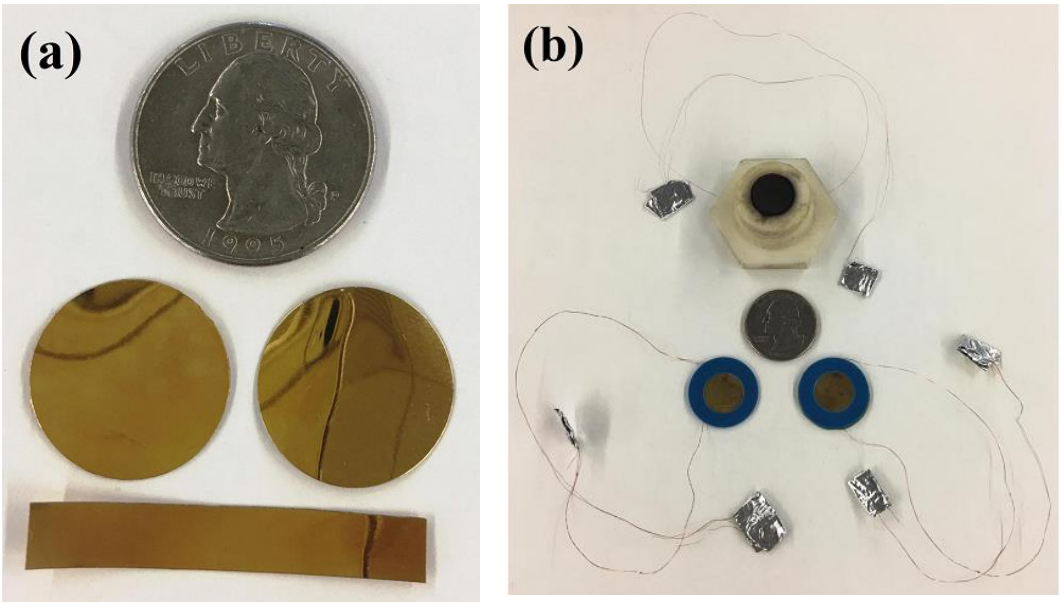

Figure 4.2. Fabricated IPMC segments (a) before and (b) after mounting on their compression, bending and shear frames

In order to obtain equivalent capacitance and resistance of fabricated IPMC sensors, Agilent 4294A precision impedance analyzer is used and the frequency domain parallel resistance and capacitance responses for all fabricated segments used in compression, bending and shear

modes at the times of conducting the experiments are given in Figure 4.3, Figure 4.4 and Figure 4.5, respectively. Moreover, the magnitude of equivalent capacitance and resistance for each IPMC of each type is given in Table 4.1. As it can be seen in Figure 4.3, Figure 4.4, Figure 4.5 and Table 4.1, both acrylic coated and naked segments of each mode of deformation have similar frequency domain responses for parallel resistance and capacitance. But, elapsing time leads to an increase in the resistance and a decrease in the capacitance of naked IPMCs while these parameters remain almost constant for acrylic coated segments. The best way to explain the reason is that evaporating the diluent by the time changes the properties of the fabricated IPMC which happens in the acrylic coated ones with a lower rate.

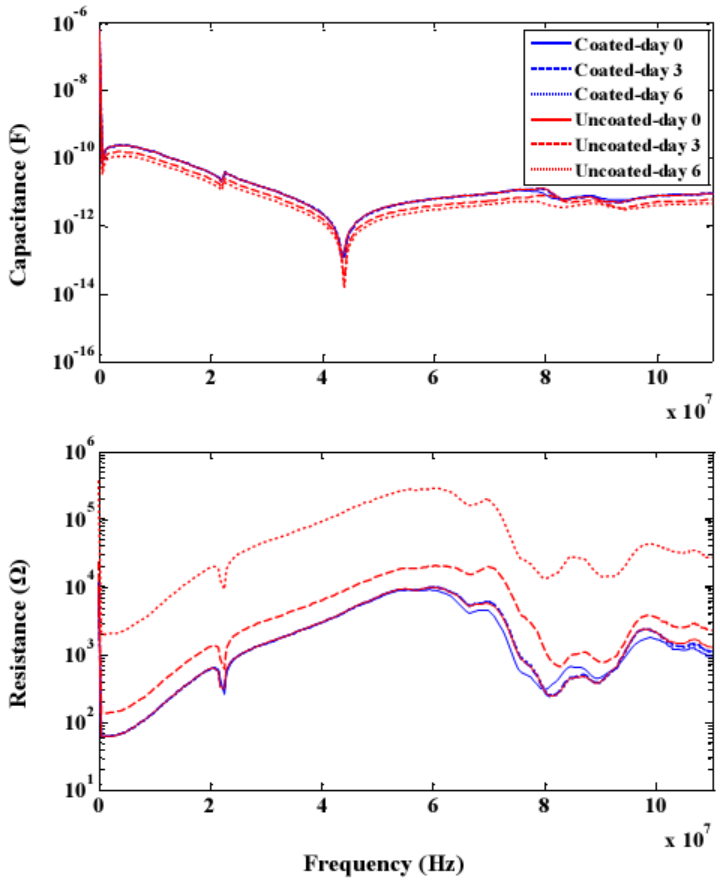

Figure 4.3. The frequency domain parallel resistance and capacitance responses of all fabricated IPMC segments used in compression mode over time

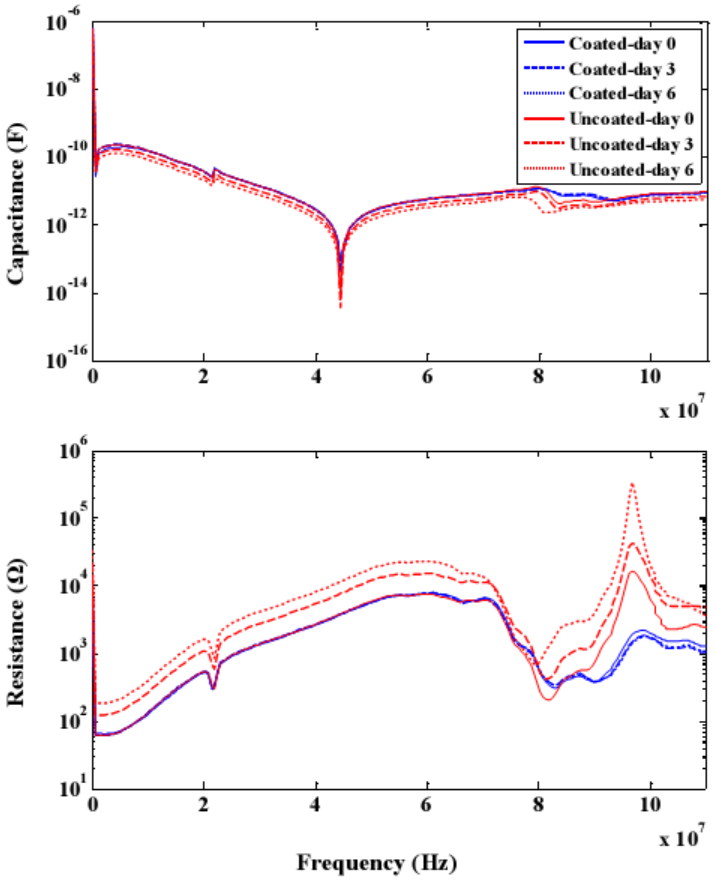

Figure 4.4. The frequency domain parallel resistance and capacitance responses of all fabricated IPMC segments used in bending mode over time

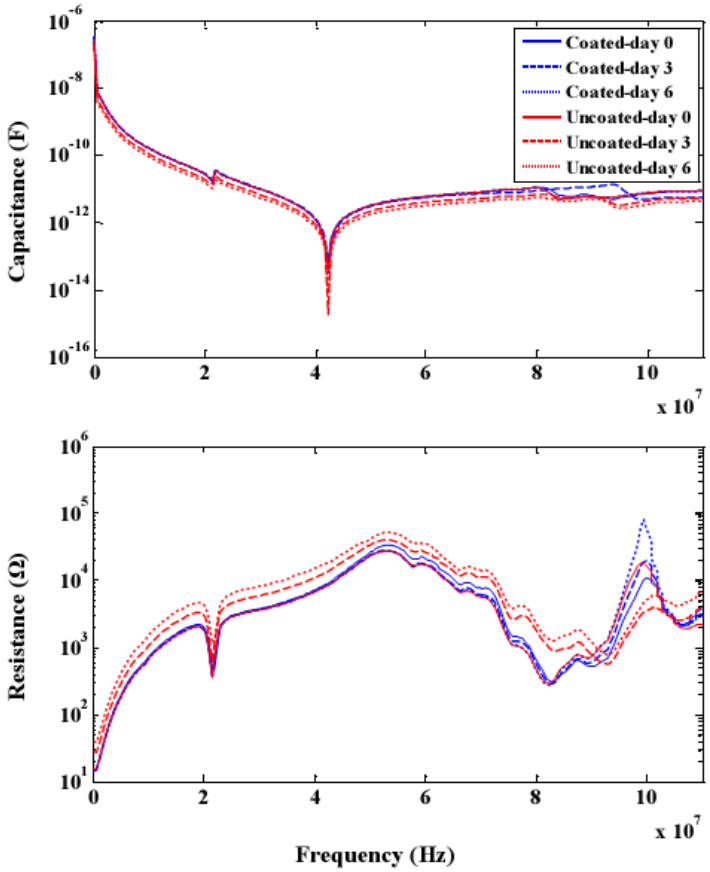

Figure 4.5. The frequency domain parallel resistance and capacitance responses of all fabricated IPMC segments used in shear mode over time

Table 4.1. Equivalent capacitance and resistance of fabricated sensors over time

Mode	Day(s) after fabrication	Equivalent capacitance (nF)		Equivalent resistance (kΩ)	
		Acrylic coated	Uncoated	Acrylic coated	Uncoated
Compression	0	588	607	11.4	10.3
	3	607	396	10.8	23.3
	6	590	295	11.3	36.2
Bending	0	583	603	11.2	10.5
	3	629	430	9.42	21.2
	6	616	327	9.92	32.7
Shear	0	256	285	14.4	15.3
	3	352	204	14.6	28.4
	6	322	163	15.3	40.1

According to Table 4.1, the highest values for equivalent capacitance and resistance of two compression mode IPMC segments in all experiments are 607 nF and 36.2 kΩ, respectively, these quantities for bending mode segments are 629 nF and 32.7 kΩ, respectively, and these quantities for shear mode ones are 352 nF and 40.1 kΩ, respectively. By setting the signal conditioner elements as $R_f = 100\ k\Omega$, $C_f = 1\mu F$ and $R_i = 10\ \Omega$, it is guaranteed that the system low and high cutoff frequencies for compression mode segments will be around $f_L = 1.59\ Hz$ and $f_H = 26.2\ kHz$, respectively, for bending mode segments will be around $f_L = 1.59\ Hz$ and $f_H = 25.3\ kHz$, respectively, and for shear mode ones will be around $f_L = 1.59\ Hz$ and $f_H = 45.2\ kHz$, respectively, Meanwhile, OP177 which is fed by 9V batteries has been used as the operational amplifier.

Each IPMC segment fixed on its relevant structure and the standard pressure sensor, PCB116B02, are mounted on the shock tube, 54 mm diameter, at the middle holes, 310 mm distance from the membrane. Three different membranes including single layer Mylar, Aluminum sheet and double layer Mylar have been used in order to produce different shock pressures. The impulse response of each sensor has been captured 2 times for each membrane and this procedure was done 3 times: just after fabrication, 3 days after fabrication and 6 days after fabrication of IPMCs.

Among all tests conducted during 6 days, one set of impulse responses of the proposed acrylic coated IPMC for compression, bending and shear mode of deformations are presented in Figure 4.6 through Figure 4.17, and compared with the corresponding response from the standard commercial pressure sensor. The first point that can be noticed in these figures is that three different IPMC sensors have a much different transient responses than the standard sensor which is based on piezoelectric materials. In the IPMC sensor vibration damping happens much faster

than the piezoelectric one and the main reason, in addition to the different designation of structures, is the existence of diluent in the IPMC which increases the damping ratio significantly. In addition, different time responses of IPMC sensors under compression, bending and shear stimulations originate from dissimilar structures and boundary conditions of IPMC segments in their related frames.

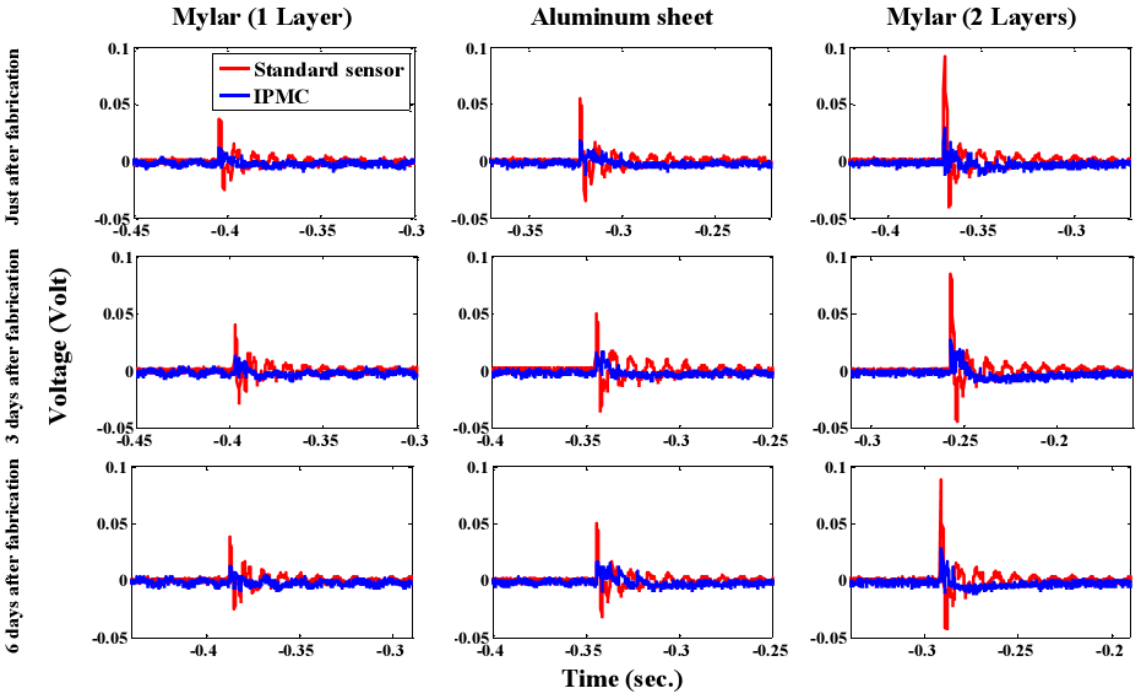

Figure 4.6. Impulse responses of the first run of acrylic coated IPMC segments under compression

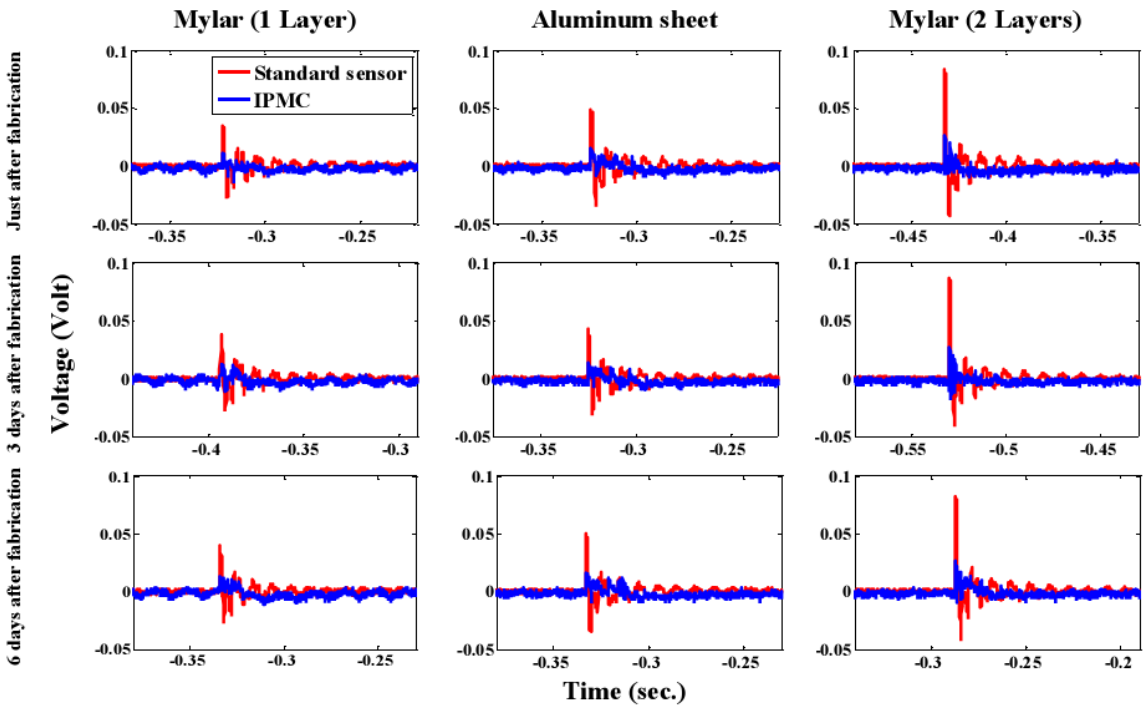

Figure 4.7. Impulse responses of the second run of acrylic coated IPMC segments under compression

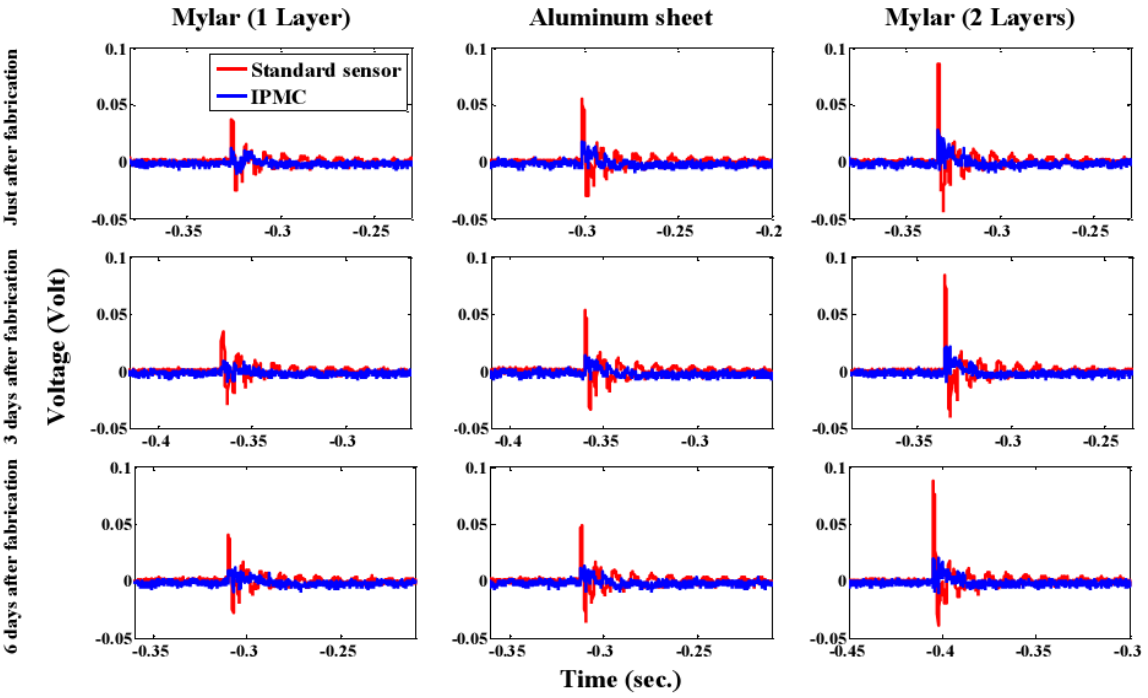

Figure 4.8. Impulse responses of the first run of uncoated IPMC segments under compression

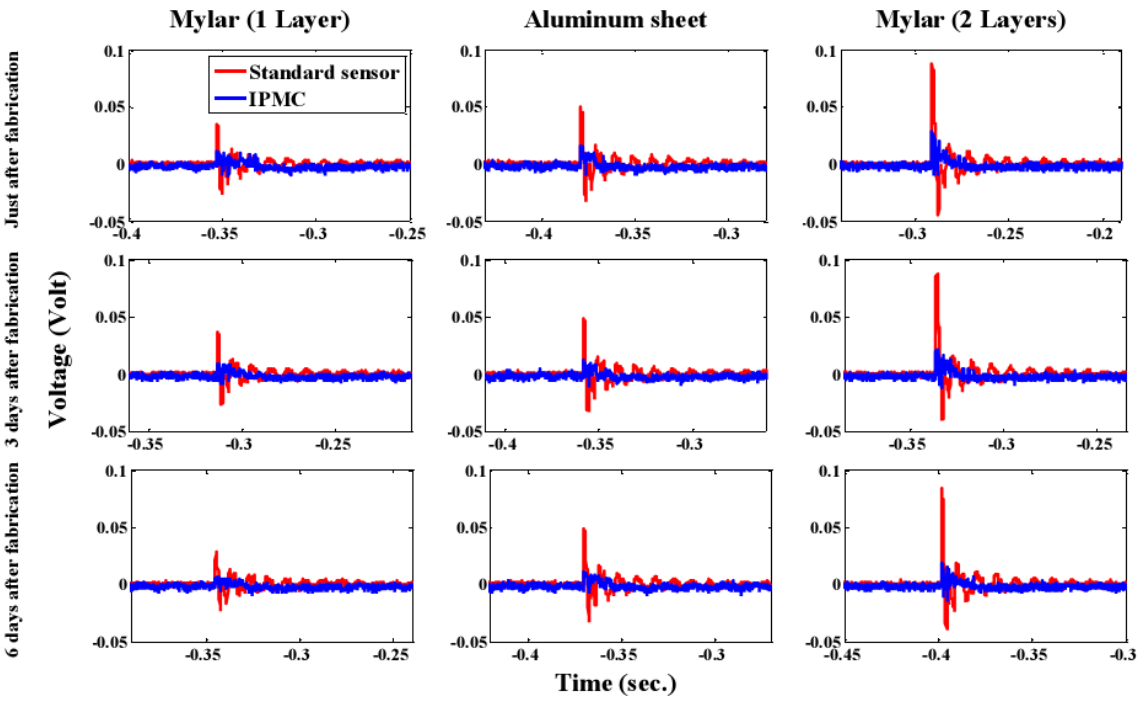

Figure 4.9. Impulse responses of the second run of uncoated IPMC segments under compression

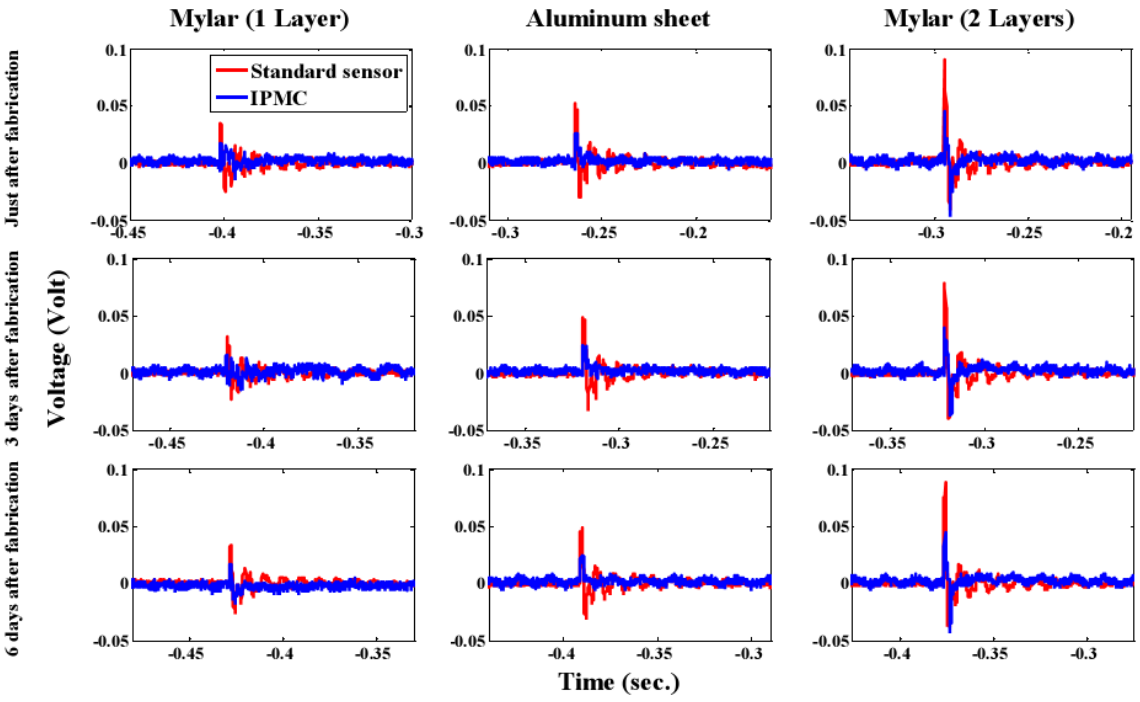

Figure 4.10. Impulse responses of the first run of acrylic coated IPMC segments under bending

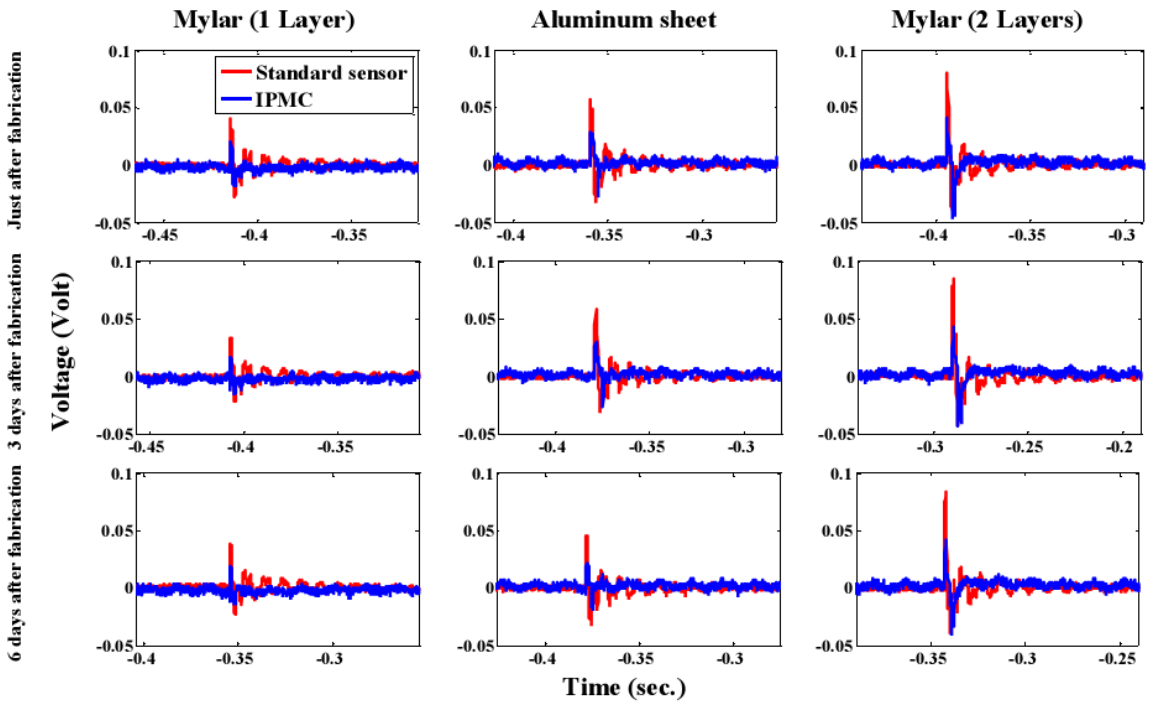

Figure 4.11. Impulse responses of the second run of acrylic coated IPMC segments under bending

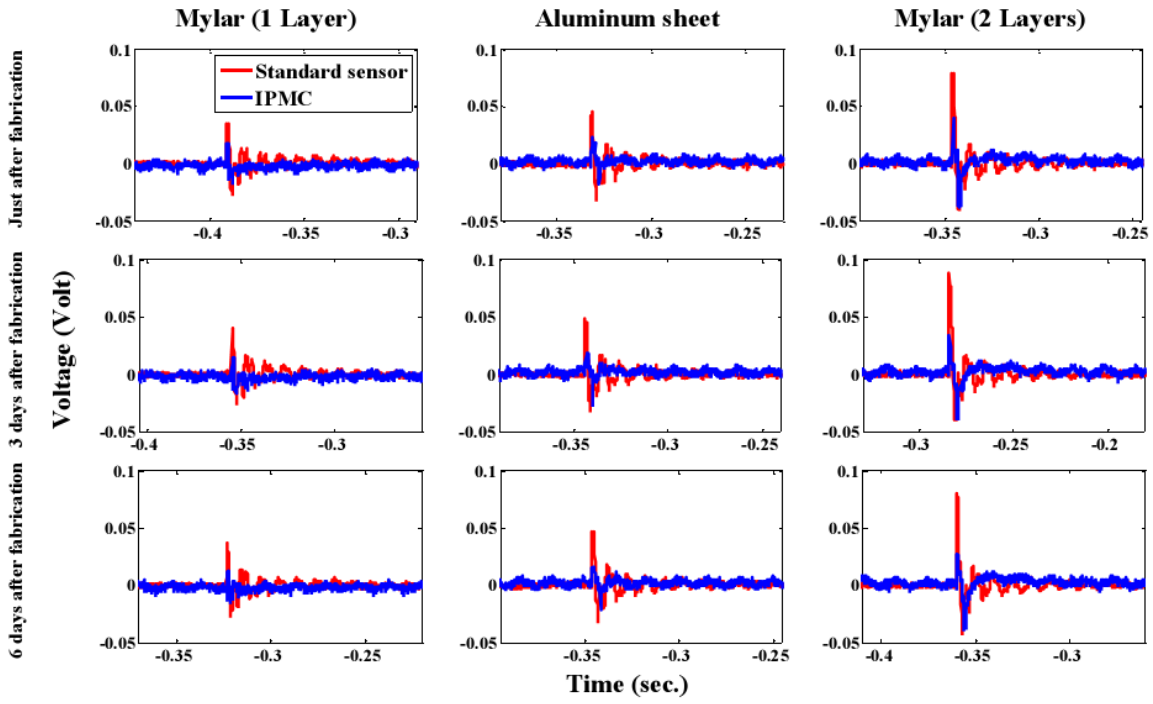

Figure 4.12. Impulse responses of the first run of uncoated IPMC segments under bending

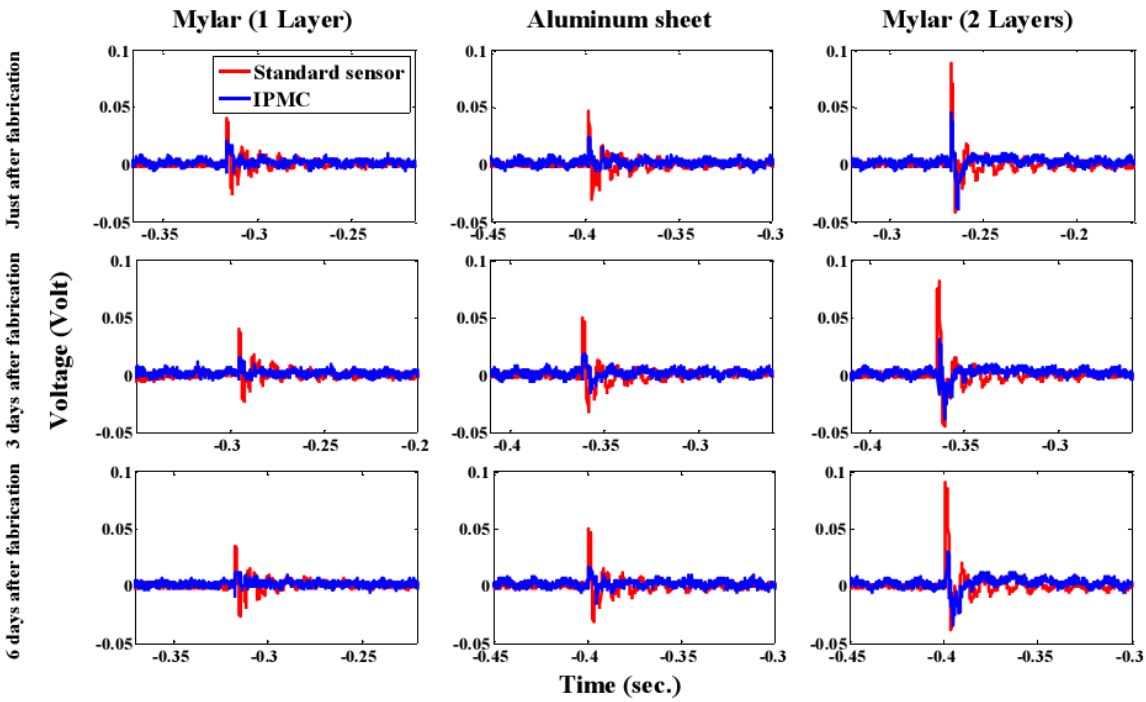

Figure 4.13. Impulse responses of the second run of uncoated IPMC segments under bending

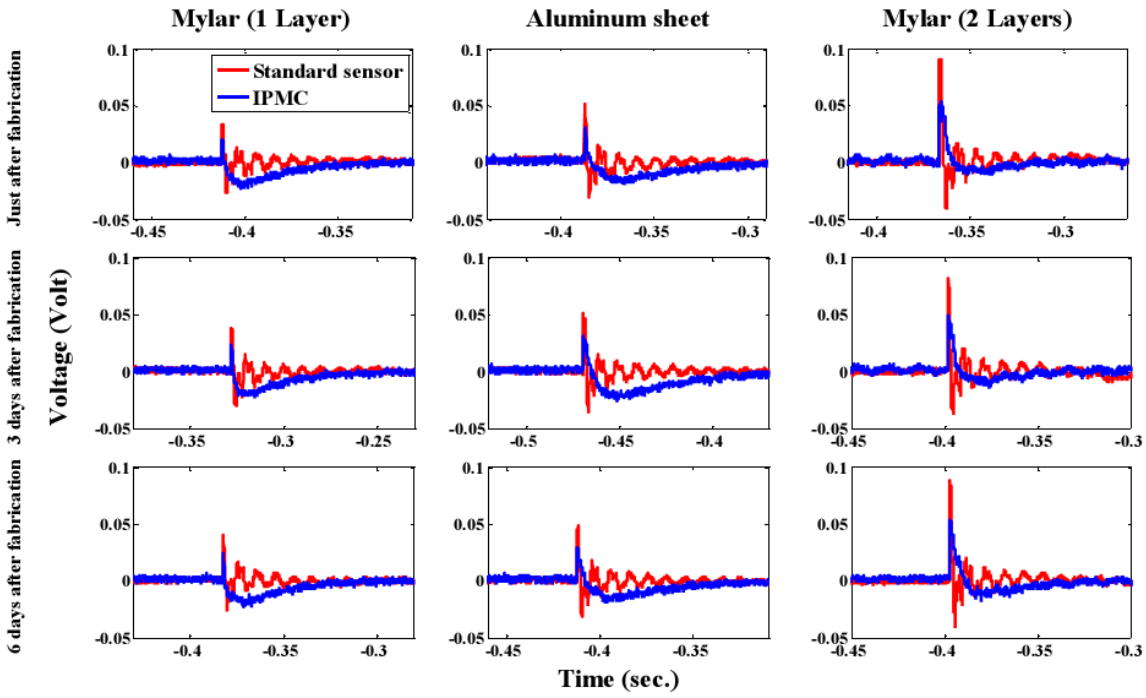

Figure 4.14. Impulse responses of the first run of acrylic coated IPMC segments under shear

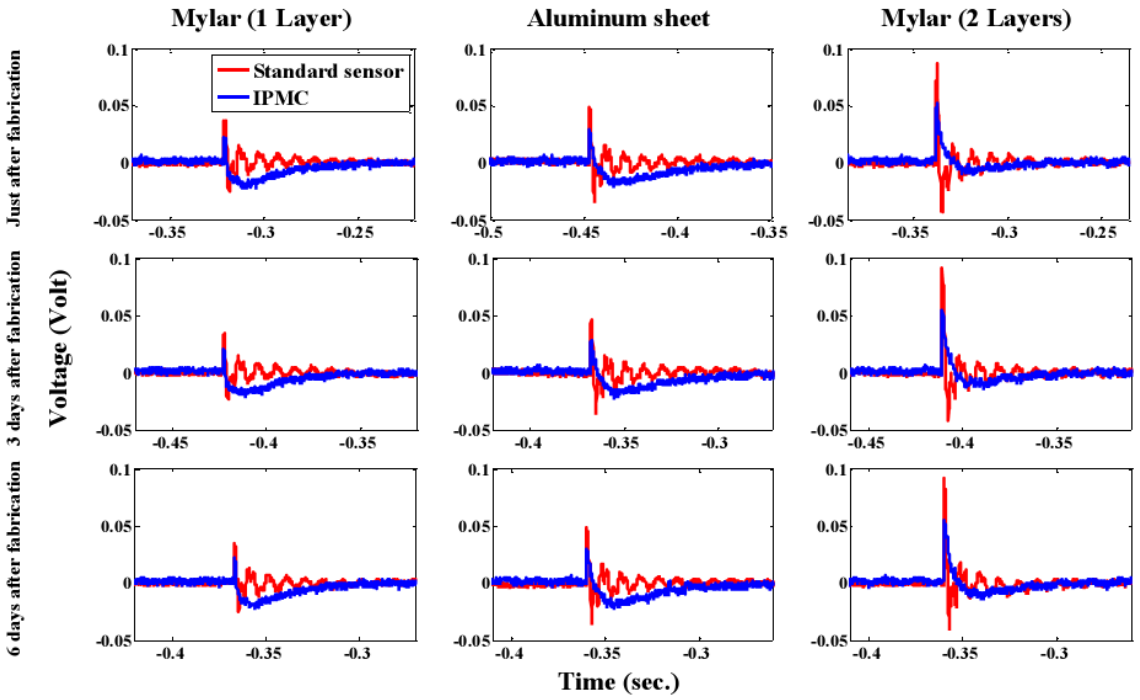

Figure 4.15. Impulse responses of the second run of acrylic coated IPMC segments under shear

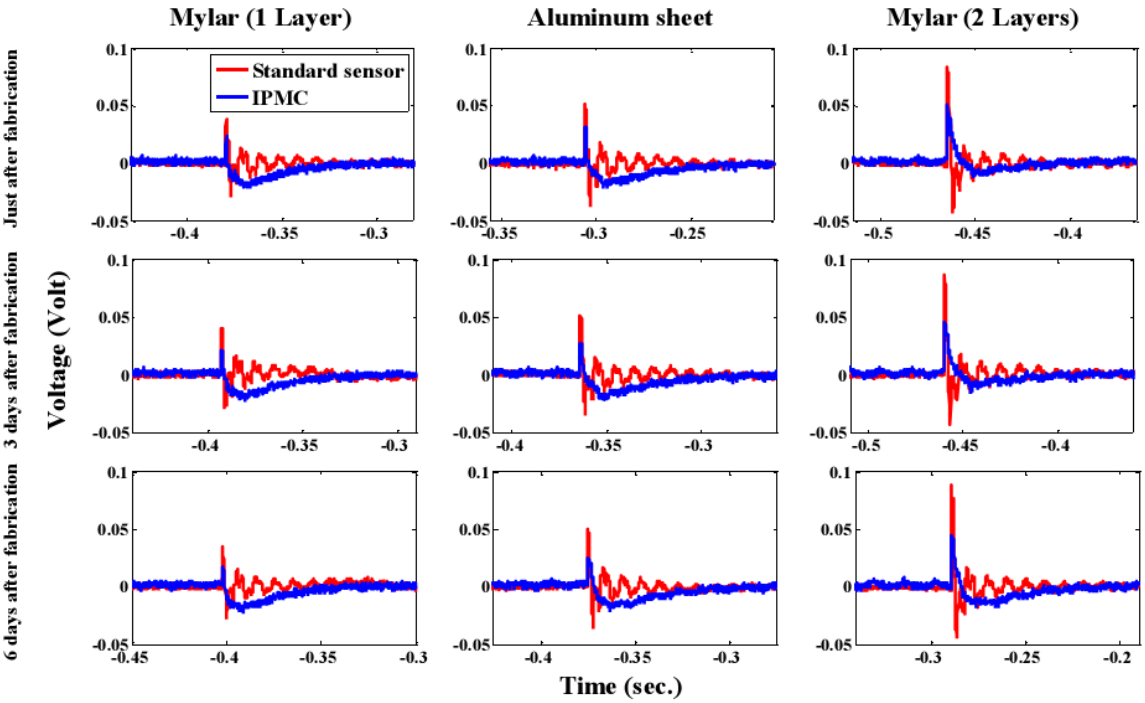

Figure 4.16. Impulse responses of the first run of uncoated IPMC segments under shear

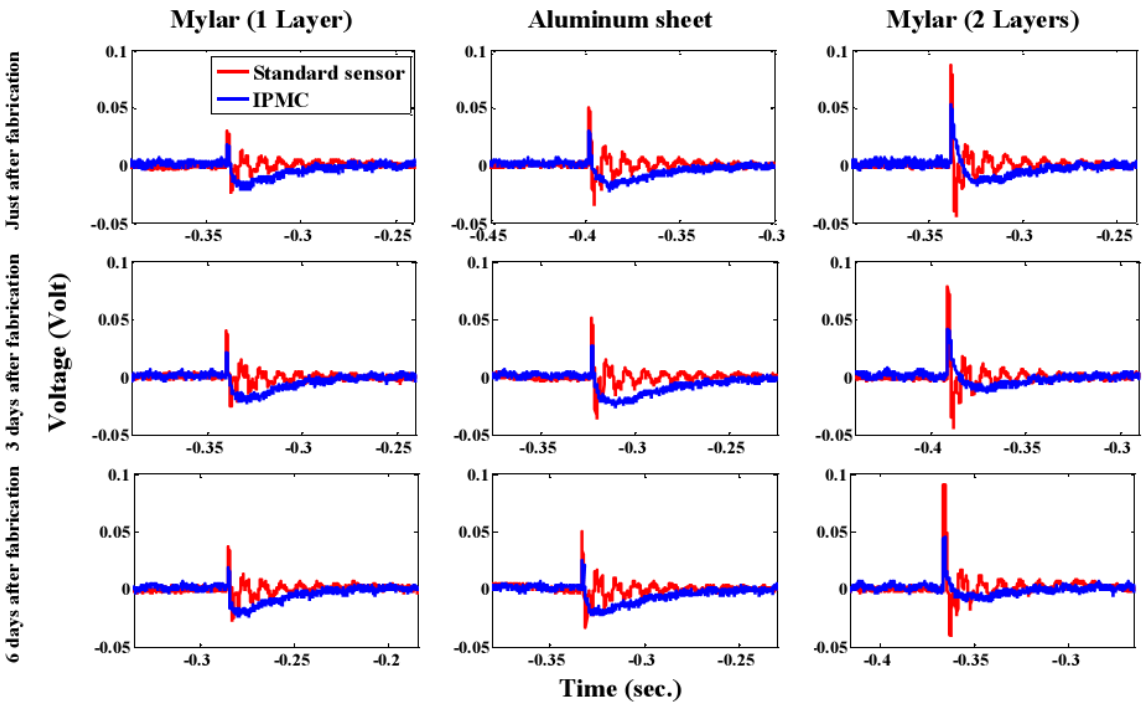

Figure 4.17. Impulse responses of the second run of uncoated IPMC segments under shear

The peak pressure data of all experiments done in 6 days for all modes of deformation, for both acrylic coated and naked IPMC segments, are given in Table 4.2, Table 4.3 and Table 4.4, respectively. These tables contain measured output voltages of different IPMC sensors and standard pressure sensor for different membrane layers. For each mode of deformation, by comparing the peak values of each sensor's output to the standard pressure sensor's signal, calibration curves can be drawn. Sensitivity calibration curve shows generated charge magnitudes with respect to reference pressures for all tests, measured by the standard sensor (PCB116B02 with the sensitivity of 0.7978 pC/kPa) which is connected to Kistler 5010B charge amplifier with a total amplification 1000 kPa/V in the performed experiments. Figure 4.18 illustrates the calibration curves for both acrylic-coated and naked compression, bending and shear mode sensors, respectively.

Table 4.2. Compression mode sensor's output voltage at the peak pressure

IPMC type/Run #	Membrane/Layer(s)	Measured voltage (mV)	Test time		
			Just after fabrication	3 days after fabrication	6 days after fabrication
Encapsulated/#1	Maylar/1	Standard sensor	36.7	40.2	38.4
		IPMC	11.7	12.9	11.6
	Aluminum sheet/1	Standard sensor	55.1	50.3	50.1
		IPMC	17.8	16.1	16.2
	Maylar/2	Standard sensor	91.9	85.3	88.6
		IPMC	29.4	27.3	27.6
Encapsulated/#2	Maylar/1	Standard sensor	35.1	38.4	40.1
		IPMC	11.3	12.4	12.8
	Aluminum sheet/1	Standard sensor	48.4	43.4	50.1
		IPMC	15.3	13.8	15.9
	Maylar/2	Standard sensor	83.6	86.9	82.5
		IPMC	26.7	27.3	26.3
Unencapsulated/#1	Maylar/1	Standard sensor	36.8	35.1	40.2
		IPMC	11.6	8.7	9.1
	Aluminum sheet/1	Standard sensor	55.1	53.5	48.4
		IPMC	17.3	13.6	10.9
	Maylar/2	Standard sensor	85.9	84.2	87.5
		IPMC	26.9	21.2	19.5
Unencapsulated/#2	Maylar/1	Standard sensor	35.0	36.7	28.3
		IPMC	10.9	9.2	6.2
	Aluminum sheet/1	Standard sensor	50.1	48.5	48.4
		IPMC	16.1	12.1	10.8
	Maylar/2	Standard sensor	87.5	87.5	84.2
		IPMC	27.2	21.6	18.8

Table 4.3. Bending mode sensor's output voltage at the peak pressure

IPMC type/Run #	Membrane/Layer(s)	Measured voltage (mV)	Test time		
			Just after fabrication	3 days after fabrication	6 days after fabrication
Encapsulated/#1	Maylar/1	Standard sensor	35.1	31.7	33.5
		IPMC	17.1	15.9	16.6
	Aluminum sheet/1	Standard sensor	51.9	48.4	48.4
		IPMC	25.8	24.3	24.1
	Maylar/2	Standard sensor	90.3	78.6	88.6
		IPMC	45.3	39.4	44.5
Encapsulated/#2	Maylar/1	Standard sensor	40.1	33.4	38.4
		IPMC	19.9	16.4	18.9
	Aluminum sheet/1	Standard sensor	56.8	58.5	45.1
		IPMC	28.3	29.7	21.9
	Maylar/2	Standard sensor	80.2	85.3	83.6
		IPMC	40.1	42.8	42.0
Unencapsulated/#1	Maylar/1	Standard sensor	35.1	40.1	36.8
		IPMC	17.7	14.8	13.6
	Aluminum sheet/1	Standard sensor	45.1	48.4	46.8
		IPMC	22.8	18.5	15.6
	Maylar/2	Standard sensor	78.6	88.6	80.2
		IPMC	39.4	33.9	27.0
Unencapsulated/#2	Maylar/1	Standard sensor	40.1	40.2	35.1
		IPMC	20.8	15.4	11.8
	Aluminum sheet/1	Standard sensor	46.8	50.1	50.1
		IPMC	23.8	18.6	16.7
	Maylar/2	Standard sensor	88.6	81.9	90.3
		IPMC	45.2	31.1	29.9

Table 4.4. Shear mode sensor's output voltage at the peak pressure

IPMC type/Run #	Membrane/Layer(s)	Measured voltage (mV)	Test time		
			Just after fabrication	3 days after fabrication	6 days after fabrication
Encapsulated/#1	Maylar/1	Standard sensor	33.5	38.4	40.2
		IPMC	20.2	23.3	24.1
	Aluminum sheet/1	Standard sensor	51.8	51.8	48.4
		IPMC	30.7	31.5	29.4
	Maylar/2	Standard sensor	90.3	81.9	88.6
		IPMC	53.9	49.6	53.4
Encapsulated/#2	Maylar/1	Standard sensor	36.7	35.0	35.1
		IPMC	21.9	20.7	21.9
	Aluminum sheet/1	Standard sensor	48.4	46.8	48.4
		IPMC	29.4	28.6	29.6
	Maylar/2	Standard sensor	86.9	91.9	91.9
		IPMC	52.1	54.7	55.3
Unencapsulated/#1	Maylar/1	Standard sensor	38.4	40.2	35.0
		IPMC	23.7	21.6	17.4
	Aluminum sheet/1	Standard sensor	51.8	51.8	50.1
		IPMC	31.5	27.3	25.3
	Maylar/2	Standard sensor	83.6	86.9	88.6
		IPMC	50.5	46.2	44.3
Unencapsulated/#2	Maylar/1	Standard sensor	30.1	40.1	36.7
		IPMC	18.2	21.2	18.4
	Aluminum sheet/1	Standard sensor	50.1	51.8	50.1
		IPMC	29.6	27.4	24.9
	Maylar/2	Standard sensor	86.9	78.6	90.4
		IPMC	52.6	41.8	44.9

The most important features that should be investigated about a material which is being used to convert mechanical energy to electrical energy in a sensor are linearity, sensitivity and reliability. For a sensor, having a linear response is favorable and the set of collected peaks is expected to have a linear correlation, then for each sensor a linear regression model was fitted using the least squares approach to get the slope between generated charge (C) and applied pressure (kPa) which is actually defined as the sensitivity of the sensor. As can be seen in Figure 4.18, all correlation coefficients for each mode of deformation and for all times of conducting the tests are close enough to 1 to be able to consider the responses as linear ones with a high accuracy in the measured range.

Furthermore, the sensitivities of acrylic coated compression mode sensor, for tests done just after fabrication, 3 days after fabrication and 6 days after fabrication, are 0.319 nC/kPa, 0.313 nC/kPa and 0.315 nC/kPa, respectively, that are around 390 times higher than the utilized commercial pressure sensor (PCB116B02 with the sensitivity of 0.7978 pC/kPa). Similarly, the sensitivities of acrylic coated bending mode pressure sensors are 0.508 nC/kPa, 0.505 nC/kPa and 0.510 nC/kPa, respectively, which are around 625 times higher than PCB116B02 [68]. And likewise, the sensitivities of acrylic coated shear mode pressure sensors are 0.596 nC/kPa, 0.596 nC/kPa and 0.595 nC/kPa, respectively, which are around 740 times higher than PCB116B02. Different pressure areas and higher sensitivity of IPMC than piezoelectric materials are two main reasons which can justify these huge differences and obviously an increase in the size of the IPMC sensor will increase its sensitivity due to absorbing more force. The effective pressure area of each IPMC segment under the external pressure is a 132.67 mm^2 surface to collect pressure and produce electrical charge, while the effective pressure area for PCB116B02 standard sensor, according to its manual, is a circle with radius of 5.5 mm which provides a 95 mm^2 surface to collect pressure

and the quartz element definitely has a smaller active area to produce electrical charge. Moreover, as it is reported in [20], the streaming potential hypothesis, the fundamental mechanism responsible for sensing, is a compelling phenomenon to explain orders of magnitude higher sensitivity of IPMCs than traditional piezoelectric material due to piezoelectricity effect in crystals with no inversion symmetricity.

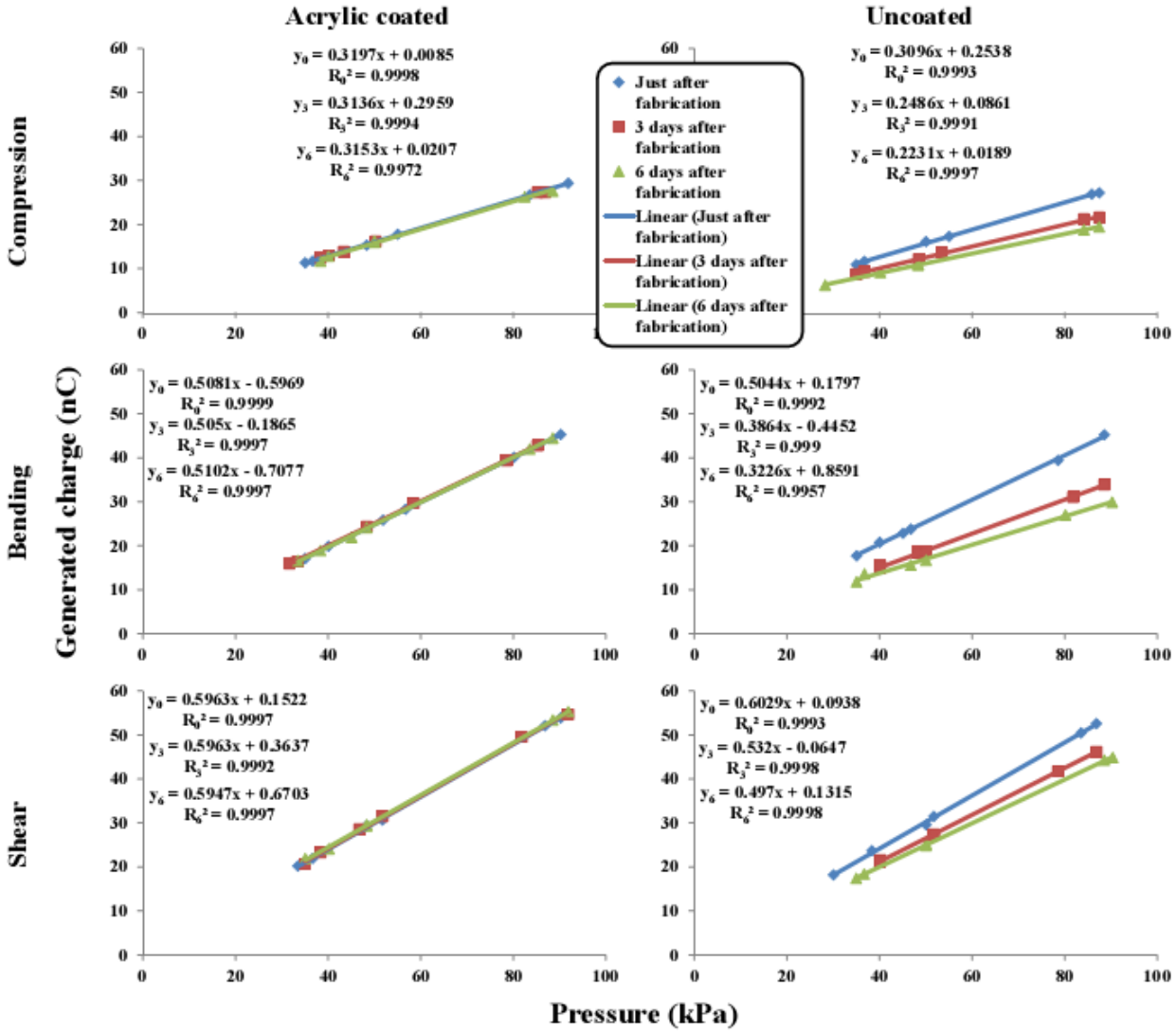

Figure 4.18. Calibration curves of all fabricated IPMC segments

Next observation to point out is that proposed IPMC have a higher sensitivity in shear mode than in bending mode by a factor of about 1.2, and have a higher sensitivity in bending mode than in compression mode by a factor of about 1.6. Note that the pressure areas for all three designed setups are the same and IPMCs have the same surfaces, thus, for similar membranes almost equal forces are applied on IPMCs and different sensitivities are only originated from different modes of deformation. In other words, although shear mode design needs more complicated manufacturing process, it offers a higher sensitivity and a greater mechanical isolation from the base than the compression and bending mode ones. The higher sensitivity of the fabricated IPMC in shear mode than bending mode and bending mode than compression mode could be explained by that more nano-channels are activated and channels' alignments are more effective in the shear mode than the bending and compression ones.

Another observation that should be mentioned is the effect of the acrylic coating. As can be seen in Figure 4.18, acrylic layer due to its high flexibility does not have any meaningful effect on the sensitivity of the IPMC sensors in all modes of deformation. And, both coated and naked sensors represent almost the same sensitivity just after fabrication. On the other hand, naked IPMC's sensitivities, the slope of the fitted linear regression line, deteriorated after 3 days and 6 days in comparison to the acrylic coated one which maintained its sensitivities for all modes of deformation. This observation shows the effect of waterproof coating on the reliability of the fabricated IPMC sensors which means maintaining the properties with the time. Finally, one can see that for the shear mode, in which the IPMC layer is the most isolated one, the sensitivity deterioration happens at a lower rate in comparison to bending and compression ones, which is another evidence for the importance of coating on the reliability of IPMCs as applicable tools.

5.0 WEARABLE IONIC POLYMER-METAL COMPOSITE (IPMC) PLANTAR PRESSURE SENSORS

Plantar pressure measurement has significant applications in diagnosis of patients with structural disorders, foot illness and pathology diseases [69] and its distribution analysis let human motion researchers estimate many parameters such as peak pressure, mean pressure and displacement speed of the pressure center [70-73]. These parameters are useful in balance analysis [69], measuring of spatiotemporal gait [74] and ground reaction forces [75] in sports and medicine which are vital not only for detecting abnormalities such as the type of foot [76], plano valgus, and clubfoot [77], but also for monitoring and diagnosing many diseases such as insensible feet [78], Parkinson, peripheral neuropathy, frailty, dementia [79] and pressure peak in diabetic foot [80, 81]. Plantar foot measurement systems are categorized into pressure platforms, imaging technologies and instrumented footwear systems. Among these three categories, the latter has been more attractive since 1963 [82] due to flexibility, mobility and its lower cost [83] and many commercial and academic groups have been developing instrumented insoles with different types of sensor technologies. In-shoe systems consist of an array of sensors within the base of shoes or in the insoles and measure the pressure interaction between the foot and the shoe [69]. To improve smart insoles' capability, many researchers are working on sensors with higher sensitivity, reliability, flexibility and faster response [84]. Consequently, pressure-sensitive materials based on the mechanism of capacitive sensing, piezoelectric sensing and piezoresistive sensing have been

utilized as pressure sensors [85, 86], while piezoelectric sensors are more attractive due to their feasible preparation, no need to an external power and easy collection of the signal. In this chapter, an insole-like wearable device which is using IPMC segments as pressure sensors to generate voltage due to deformations as the response of foot pressure distribution is introduced. Voltage generation mechanism in IPMCs due to deformation is presented based on the streaming potential hypothesis, first, and the utilized amplification circuit is developed, correspondingly. Next, in order to develop the self-powered flexible smart insole, eight circular highly flexible and acrylic coated IPMC pressure sensors are fabricated and fixed on the measuring insole at some specific anatomic areas. Subsequently, the fabricated smart insole is utilized for the real-time plantar pressure distribution analysis of a subject during static stance and gait cycle during walking and running. Produced colormaps, representing pressure distribution, based on measured signals from IPMC sensors are realistic for different phases of gait and show a good agreement with those from commercial smart insoles presented in the literature that proves the reliability of the proposed self-powered flexible smart insole.

5.1 FUNDAMENTALS

According to the streaming potential hypothesis for IPMC sensing predictions under bending, which is presentenced in section 2.1.1, top surface due to the applied distributed load is under compression and the lower surface is under tension. In other words, the stress difference between the two sides of the membrane produces an instantaneous pressure gradient in the nanochannel. And, this stress difference is a function of the applied distributed load. According to the developed model, IPMC pressure sensor, like piezoelectric materials, generates an electrical charge that is

proportional to the applied pressure. If a reciprocating force is applied, an AC voltage is seen across the terminals of the open-circuit device. Normal output voltages from IPMCs can vary from microvolts to hundreds of volts, and signal conditioning circuitry requirements vary substantially. Figure 5.1 shows the schematic structure of fabricated IPMC sensor in combination with a non-inverting voltage amplifier and the visualizing oscilloscope.

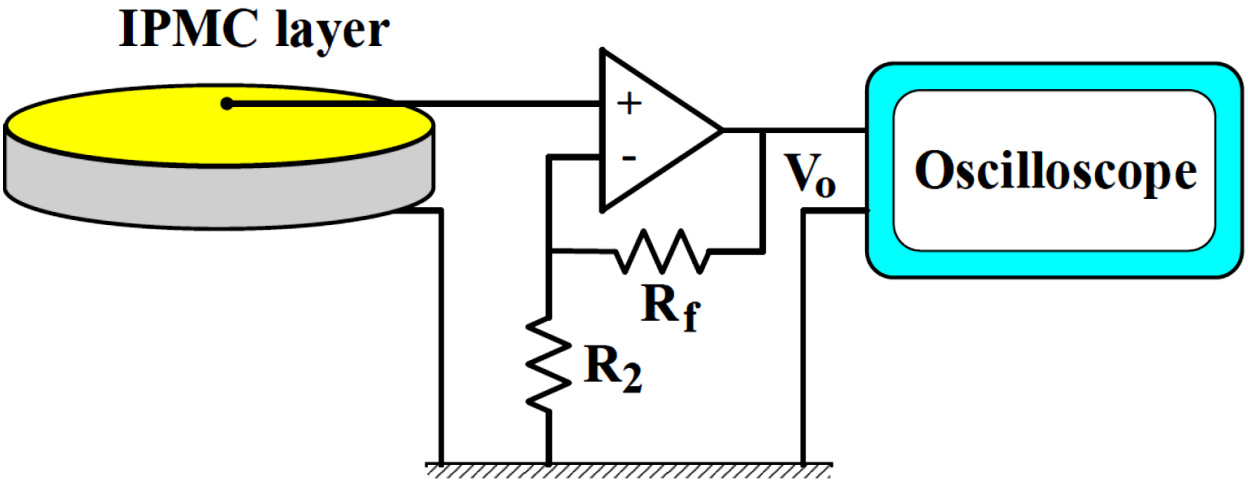

Figure 5.1. Schematic view of the IPMC pressure sensor and corresponding non-inverting voltage amplifier.

In the non-inverting amplifier's circuit, the signal is applied to the non-inverting input of the amplifier and the feedback is taken from the output via a resistor to the inverting input of the operational amplifier where another resistor is taken to ground. It is the value of these two resistors that govern the gain of the operational amplifier circuit while sensor's internal resistor has no effect on the gain. In other words, the effect of applied external pressure and exciting frequency which are changing sensor's internal resistance could be eliminated on the amplification gain. As the input to the op-amp draws no current this means that the current flowing in the resistors R_2 and R_f is the same. The voltage at the inverting input is formed from a potential divider consisting of R_2

and R_f, and as the voltage at both inputs is the same, the voltage at the inverting input must be the same as that at the non-inverting input. Hence, the voltage gain of the circuit could be calculated as

$$\frac{V_o}{V_{in}} = 1 + \frac{R_f}{R_2}. \tag{5.1}$$

The procedure which is proposed in chapter 4 is utilized for fabrication of a highly flexible IPMC layer: Nafion 117 membrane with the thickness of 170 μm is utilized as the ionic polymer layer. A layer of gold is sputtered on each side of the Nafion after cleaning, proton exchange and drying process using DC sputtering in a sputter coater (Cressington Sputter Coater 108auto). The surface resistance of fabricated IPMC is 0.9 Ω/cm on each surface. And, checking the surface of the gold sputtered polymer using Tencor Alpha-Step IQ surface profiler shows that the thickness of the gold electrode layer is about 100 nm and the thickness of the acrylic coat on the gold sputtered IPMC is about 150 nm. The picture of a fabricated circular IPMC sensor is shown in Figure 5.2(a). Agilent 4294A precision impedance analyzer is used to obtain the magnitude of equivalent parallel capacitance and resistance of fabricated IPMC sensors. The average of equivalent parallel capacitance and resistance of 8 sensors was 478 nF and 24.3 kΩ, respectively. Moreover, the time constant of each IPMC pressure sensor which is coupled with the non-inverting voltage amplifier could be defined as

$$\tau = R_s \times C_s, \tag{5.2}$$

which leads to an average time constant of 11.6 ms for each sensor. This small time constant shows the capability of proposed IPMC pressure sensors for gait analysis.

Sensors are fixed on the measuring insole using cyanoacrylates and then mounted in the shoe insole, Figure 5.2(b). The Sofcomfort®'s cushioning gel insole, which is only ~3 mm thick, is selected as the measuring insole and could be placed in any shoe, Figure 5.2(c). This commercial

insole is fabricated from advanced polymer gel which allows applied pressure to be converted into structural deformation that is then delivered to IPMC pressure sensors with every step, generates charges and is converted into electrical signal output. As it is presented in Figure 5.2(b), IPMC segments are placed at anatomic areas in accordance with a pattern which is confirmed by other studies and mathematical calculations described in the literature [42-44].

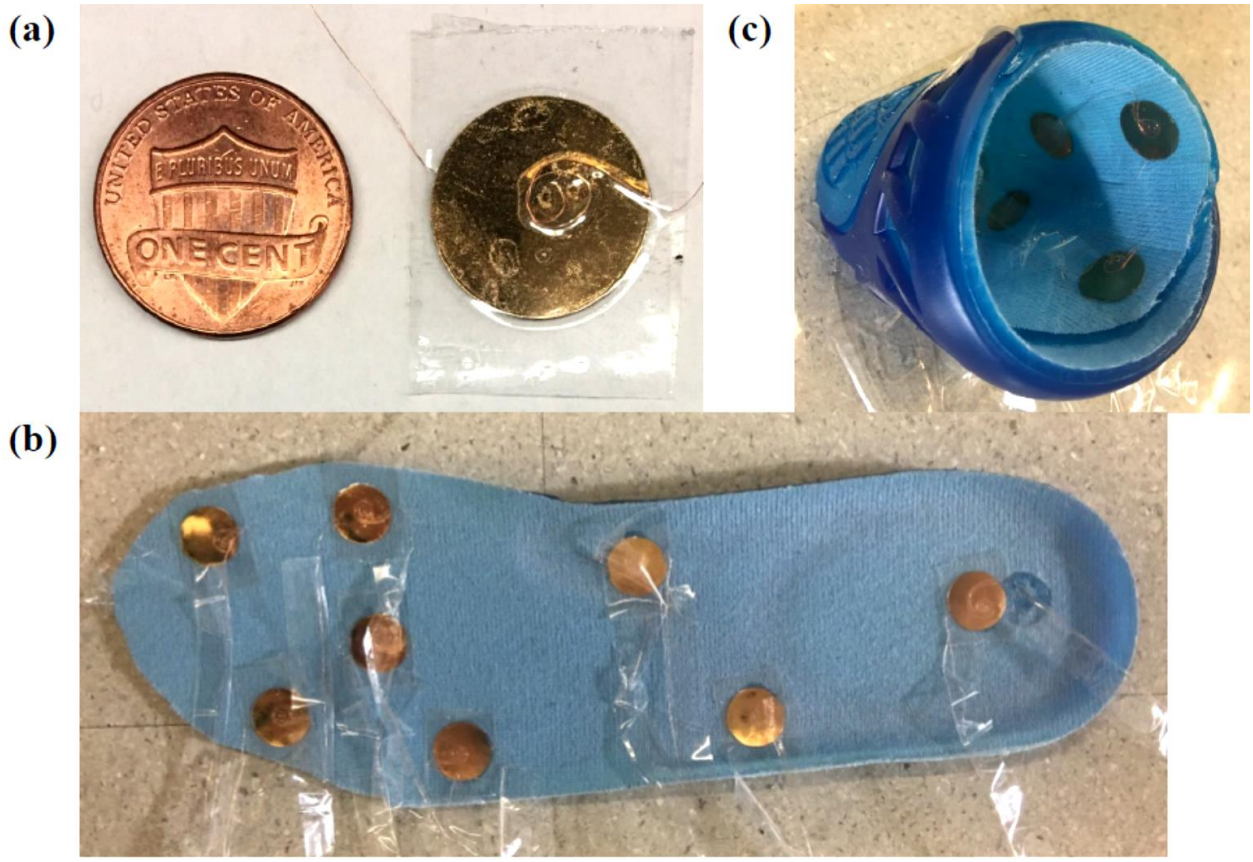

Figure 5.2. (a) Fabricated circular IPMC sensor, (b) the pattern of the 8 IPMC sensors attached to the insole, (c) flexibility of the smart insole fabricated from an advanced polymer gel and highly flexible IPMC sensors

Placement of 8 sensors, 2.01 cm^2 each, in the separate anatomical regions of a foot allows for accurate calculation of foot dynamics. Each IPMC sensor is connected to a separate voltage amplifier with two insulated wires. And, each voltage amplifier is connected to a port of the

oscilloscope (Agilent DSOX4024A Oscilloscope) for sensor output signal monitoring and recording. Such a smart insole could be a perfect solution for a widespread, affordable way to diagnose and monitor foot and posture diseases while being easy to maintain.

5.2 RESULTS AND DISCUSSIONS

Gait is the most commonly used forms of human movement during daily activity and its cycle begins when one foot makes contact with the ground and ends when that same foot makes contact with the ground again which includes stance and swing phases. Because of bearing body's weight by foot and leg, stance is considered the most important phase of the gait cycle. On the other hand, the swing phase begins with detaching toe from the ground and ends just before contacting foot with the ground again.

An insole, in universal shoe size 9 with 8 IPMC pressure sensors embedded at the base, was utilized for comparisons in gait analysis. Subject, who is a 30 years old 70 kg healthy male, was asked to stand normally 30 seconds first for data acquisition of plantar pressure distribution. Then, he was asked to walk 2 steps at a self-selected pace for gait data analysis. Finally, he was asked to run walk 2 steps at a self-selected pace. Acquired data were analyzed for each sensor and the whole foot. Generated signals from 8 IPMC sensors were recorded during normal stance, two normal walking trials and two normal running trials and are shown in Figure 5.3(a), Figure 5.3(b) and Figure 5.3(c), respectively, and the naming of 8 sensors is shown in Figure 5.3(d). In the static standing state, Figure 5.3(a), the weight of the body is distributed over the whole foot and each sensor would end up with an almost constant output voltage. On the other hand, the signals

measured by the 8 sensors during walking have different amplitudes and exhibit a periodicity, Figure 5.3(b).

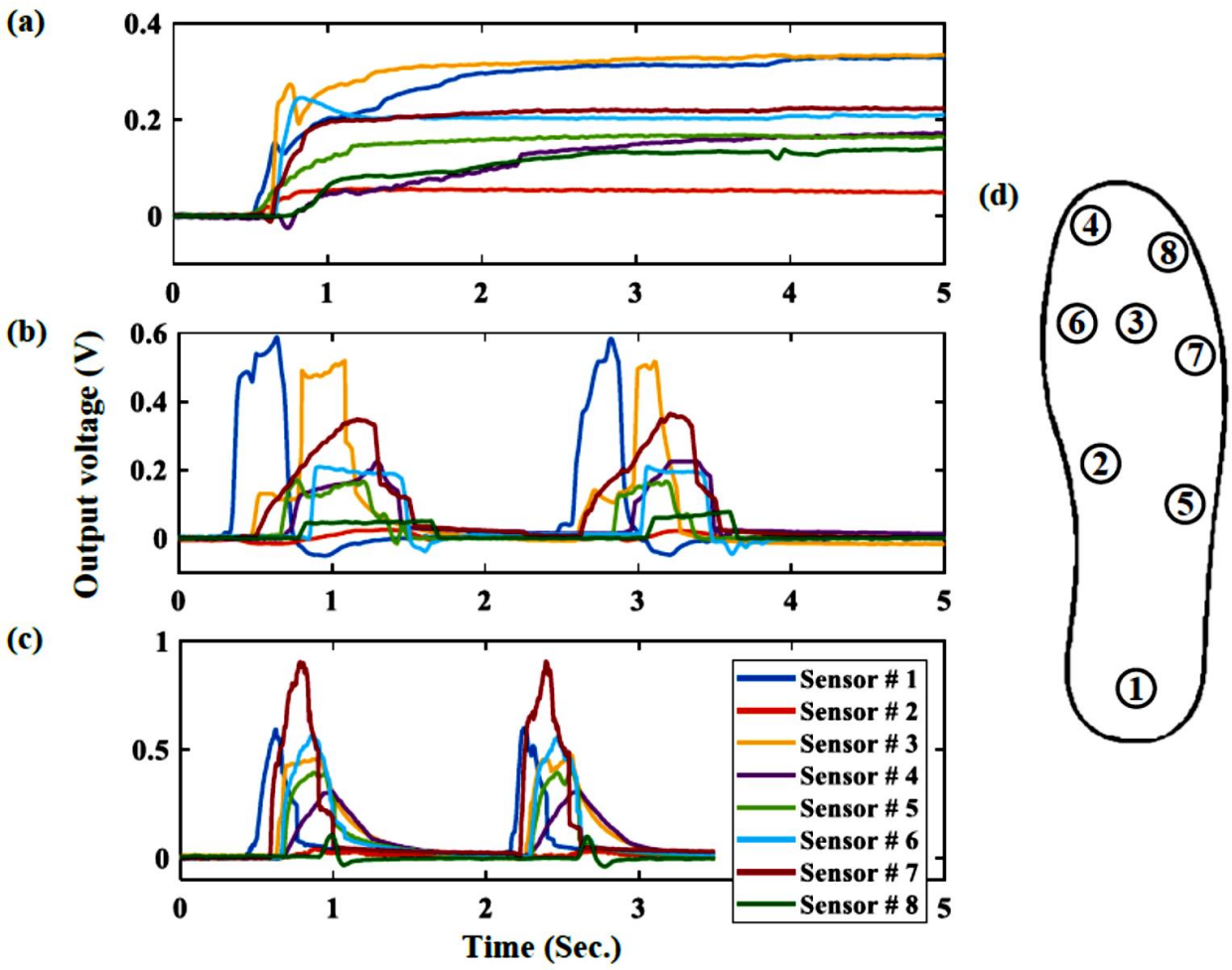

Figure 5.3. Signals obtained from sensors placed on different anatomical regions of the foot (a) static stance (b) during walking, (c) during running and (d) numbering of 8 sensors.

Different signals not only effectively reflect pressure values in the pressure insole measured at different times, but also provide the information for describing gait characteristics and performing gait analysis. The signal amplitudes of the 8 sensors at different time points correspond to the foot fall on and off the ground during walking. As can be extracted from the time series data,

the rear-foot is landing on ground firstly, then the mid-foot and fore-foot are landing with a 170 ms and 330 ms time delay, respectively. The landing time duration of fore-foot, mid-foot, and rear-foot in a gait cycle was 980 ms, 1140 ms and 1310 ms, respectively. The stance phase accounts for 63% of the total gait cycle and the swing phase comprises the remaining 37% of it. In addition, the maximum mean peak voltages generated from the fore-foot (sensors: 3, 4, 5, 7 and 8), mid-foot (sensors: 2 and 6) and rear-foot (sensor: 1) are about 0.26, 0.12 and 0.58 Volts, respectively [87]. The detailed description of the participant's time characteristics is given in Table 5.1.

Table 5.1. The participant's time characteristics obtained during walking and running trials.

Characteristics	Walking	Running
Gait cycle	2.19 s	1.72 s
Stance phase	1.37 s	0.61 s
Swing phase	0.82 s	1.11 s

Similarly, the signals measured by the 8 sensors during the running cycle have different amplitudes and show a periodicity with a higher rate, Figure 5.3(c). According to the signals of the 8 sensors at different time points during running, the rear-foot is landing on ground firstly, then the mid-foot and fore-foot are landing with a 95 ms and 190 ms time delay, respectively. The landing time durations of fore-foot, mid-foot, and rear-foot in a gait cycle are 415 ms, 510 ms and 605 ms, respectively. The stance phase accounted for 35% of the total cycle, and the swing phase comprised the remaining 65% of the gait cycle. In addition, the maximum mean peak pressures of the fore-foot (sensors: 3, 4, 5, 7 and 8), mid-foot (sensors: 2 and 6) and rear-foot (sensor: 1) are about 0.47, 0.2 and 0.62 Volts, respectively, which shows a considerably higher propulsion force during running. Description of the participant's time characteristics is shown in Table 5.1.

The plantar pressure during the major phases of a full gait cycle was measured by the developed smart insole and the distribution maps for static stance and dynamic stance phases are demonstrated by a color legend ranging from dark blue (low signal) to red (high signal) in the top row of Figure 5.4(a)-(e).

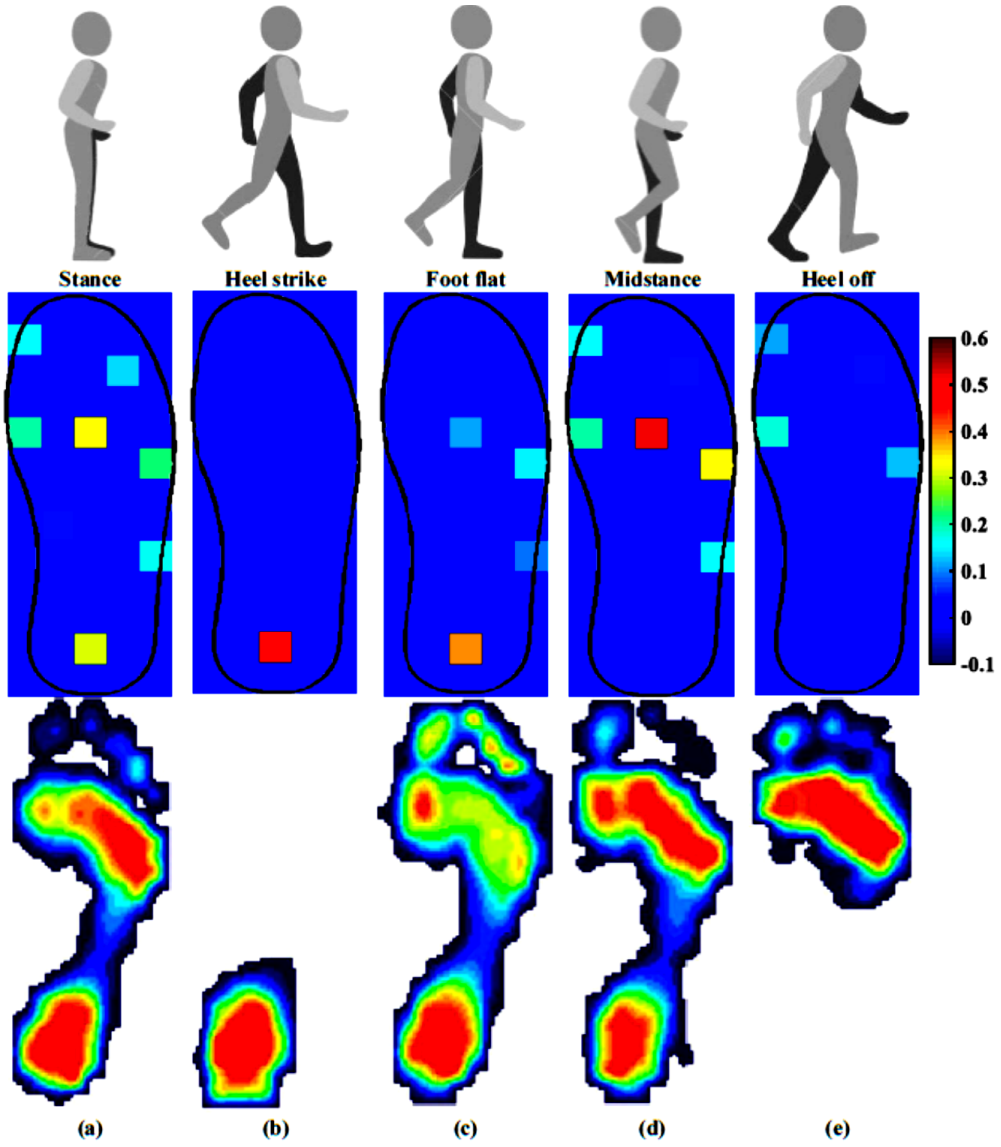

Figure 5.4. Plantar pressure distribution of one foot during (a) static stance (b)-(e) dynamic stance phase of walking. (Top row colormaps are measured by the proposed IPMC smart insole and the bottom row ones are reported in [84], which are measured by a commercial pressure measurement device)

The reliability of the proposed insole is evaluated by a commercial Matscan system which is presented in [84], the bottom row of Figure 5.4(a)-(e). In the static standing state, the weight of the body is evenly distributed over the whole foot, which is shown in Figure 5.4(a). As presented in the figure, a gait cycle during the dynamic stance phase typically consists of heel strike, foot flat, midstance and heel off. The mean generated voltages on fore-foot region obtained from the top row of Figure 5.4(b)-(e) are 0, 0.07, 0.28 and 0.16 volt, respectively, and the generated voltages on rear-foot region are 0.51, 0.39, 0 and -0.05 volt, respectively. Correspondingly, the plantar pressure distribution offers a good agreement with those obtained from the Matscan system (the bottom row of Figure 5.4(b)-(e)). It can be noted that, the plantar pressure in Figure 5.4(d) and fore-foot region in Figure 5.4(e) are much larger than the one in the static stance where the body weight is supported by both two legs. The variation is mainly due to the foot, which came into dynamic stance phases and suffered from the majority of the body weight.

Similarly, the running cycle is divided into dynamic stance and swing phases and the distribution colormaps during the stance phase, measured by the developed smart insole, are displayed by three colormaps in Figure 5.5(a)-(c). As presented in the figure, a running cycle typically consists of initial contact, midstance and propulsion. Initial contact is when the foot lands on the ground which is the cushioning phase of the running cycle. During midstance the foot provides a stable platform for the body weight to pass over and by now the foot should have stopped pronating. Propulsion, which is the final stage of the stance phase, begins immediately as the heel lifts off the ground. As the big toe turns upwards the windlass mechanism comes into play, tightening the plantar fascia and helping to raise the arch of the foot. The mean generated voltages on fore-foot region obtained from Figure 5.5(a)-(c) are 0.14, 0.37 and 0.46 volt, respectively, and the mean generated voltages on rear-foot regions are 0.59, 0.37 and 0.15 volt, respectively. It can

be noted that the plantar pressure measured by sensor # 3 in Figure 5.5(c) was much larger than the one in walking cycle which shows the higher propulsion force which is needed for running than the one which is required for walking, Figure 5.4(d).

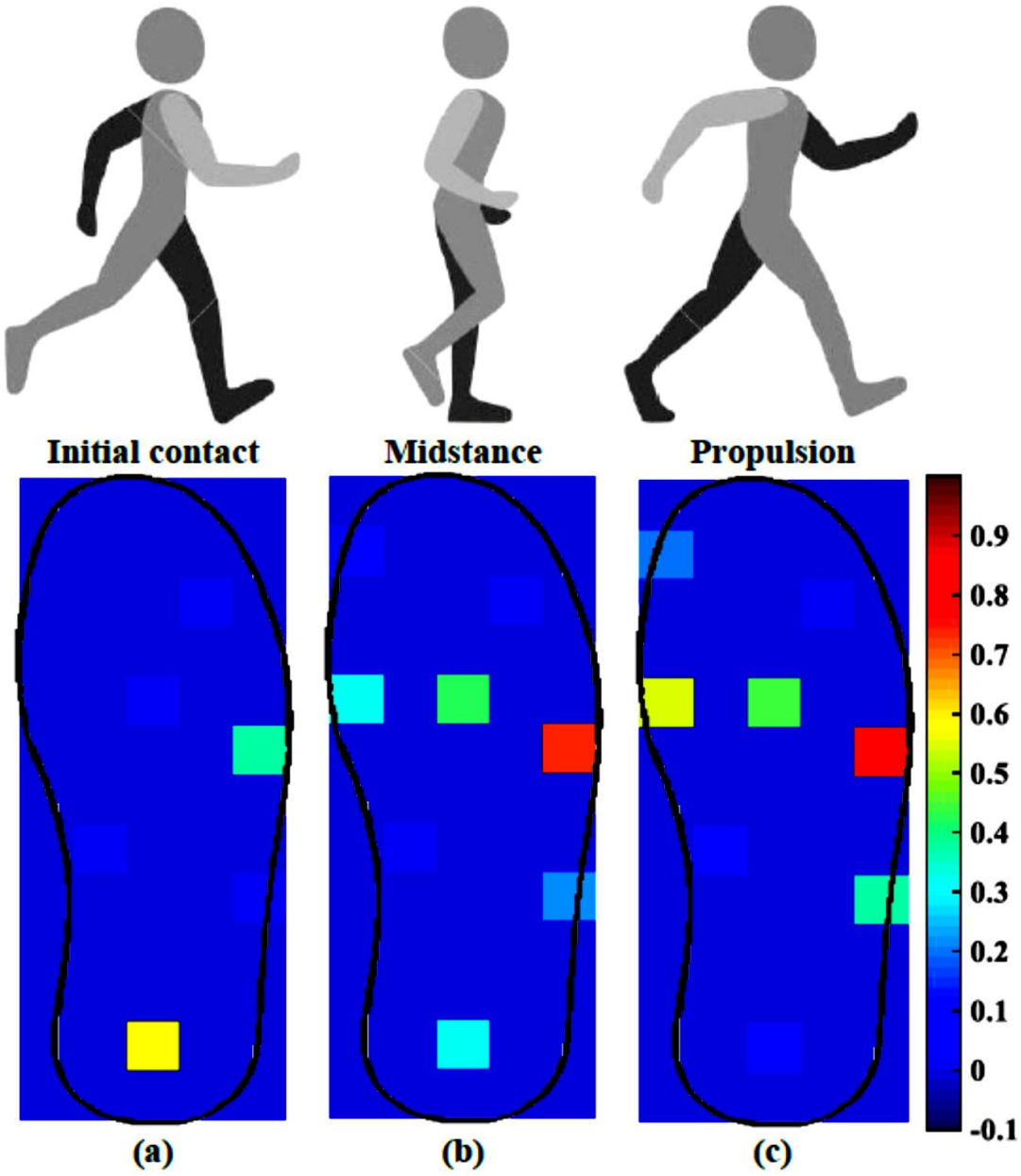

Figure 5.5. Plantar pressure distribution of one foot during the dynamic stance phase of running.

Visualized results show that the proposed self-powered wearable IPMC smart insole is reliable and through distributions of plantar pressure, some simple motions can be judged by displaying and comparison of all 8 signals of the gait: electric signal value for each individual sensor at any moment of the foot to substrate interaction; foot to ground contact time; individual anatomical areas of foot to substrate contact time. Collected data can be recorded and transferred to the computer and through analysis of distribution colormaps changes of plantar pressure distributions could be clearly detected and the combination of significant difference, peak values and the distributed pressure for different areas could be studied to diagnose common structural disorders, foot illness and pathology diseases.

6.0 IONIC POLYMER-METAL COMPOSITE (IPMC) SENSORS FOR MONITORING PHYSIOLOGICAL AND TACTILE SIGNALS

Strain sensors which can be integrated into cloth or directly attached on the human skin are fascinating for their excellent features and great potential applications in real-time monitoring of the human motions or physiological signals such as heartbeat and pulse wave [88-91]. Conventional wearable strain sensors work by detecting the resistance or capacitance change of the materials in response to the external strain. However various resistive and capacitive sensors with high sensitivity, good stability and outstanding wearable performance have been developed, the direction of the bending-induced strain cannot be identified and an additional power supply for the operation of the sensors is required [92-94]. Moreover, achieving monitoring of both the large-scale body motions and subtle physiological signals still remains a challenge for the currently wearable sensor. Therefore, it is highly desirable to develop a new type of wearable sensors to fulfill these urgent requirements. In this chapter, IPMC sensors are developed for monitoring blood pulse wave and as a flexible touch sensor. An IPMC layer is fabricated using gold electrode coating over the Nafion-117 membrane, first. This sensor is able to generate a stable electrical voltage under the externally applied deformations without the requirement of any power supply. Then, through simple encapsulation using strapping tape, the IPMC segment can be directly attached to human's skin for the real-time measurement of the human subtle pulse wave. Consequently, the amplitude, frequency and shape of the pulse wave which is visualized will be discussed.

Furthermore, for developing a self-powered soft touch sensor, a flexible IPMC disk is located on a solid cylinder filled with silicone rubber and protected by a layer of polyamide. A non-inverting voltage amplifier is utilized to amplify the generated voltage, and the effect of exciting frequency, the magnitude of applied touch force on the sensitivity and a wide range of input signals are investigated. The developed touch sensor is connected to an on-off switch circuit based on piezoelectricity to investigate its repeatability and stability. Finally, the 3D printing is hired to fabricate a designed flexible cap in order to limit the deformation of the IPMC segment and the generated voltage in a specific range and enhance the effectiveness of the proposed touch sensor for on-off switches.

6.1 METHODS AND MATERIALS

The procedure which is proposed in chapter 4 is utilized for fabrication of a highly flexible IPMC layer. To control the deformation of IPMC layer as a touch sensor and make it stable under various external forces, a disk-shaped IPMC is located on a solid circular cylinder filed with silicone rubber. The touch side of IPMC layer is protected with a thin layer of polyamide. The IPMC layer is attached to the silicone rubber and its edge is located on the solid cylinder which could be considered as a simply support circular plate on an elastic foundation.

Figure 6.1(a) and Figure 6.1(b) show schematic structures of fabricated IPMC blood pulse sensor in combination with non-inverting voltage amplifier and the visualizing oscilloscope and fabricated IPMC touch sensor switch in combination with non-inverting voltage amplifier, respectively.

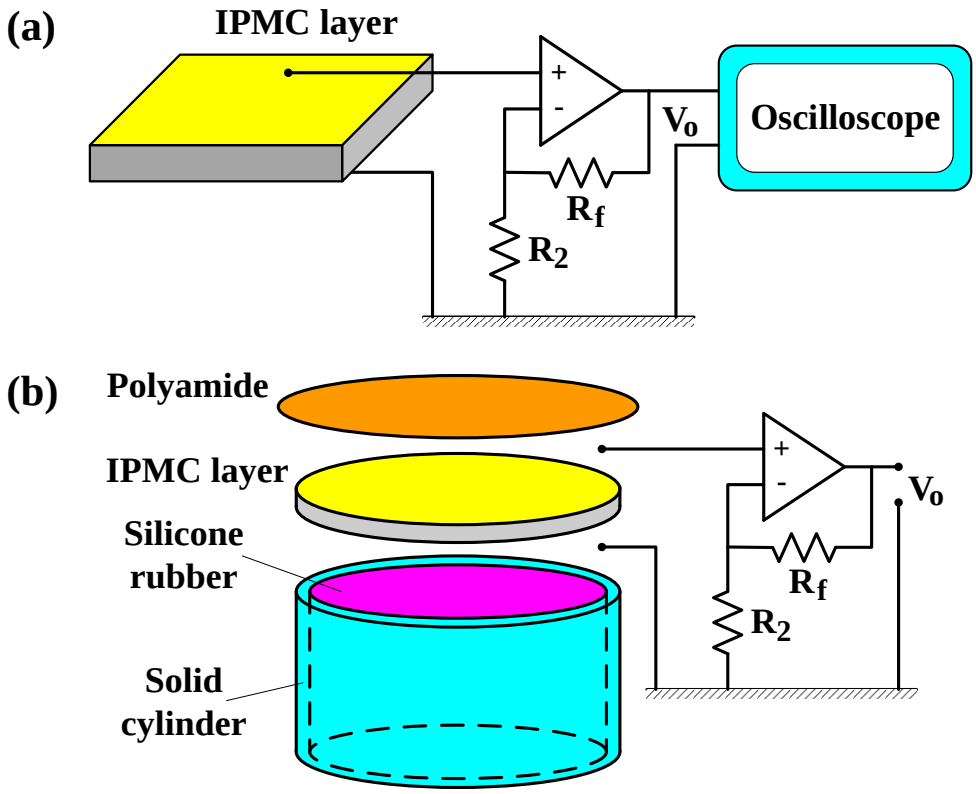

Figure 6.1. Schematic structures of (a) fabricated IPMC sensor and corresponding voltage amplifier and (b) fabricated touch sensor and corresponding voltage amplifier.

The utilized non-inverting amplifier's circuit is similar to the one presented in section 5.1 and equation (5.1) can be used to calculate the voltage gain of the circuit. To monitor the pulse wave, which is an important physiological signal for the arterial blood pressure and heart rate, the fabricated IPMC segment is attached to the wrist and the voltage signal is visualized and recorded using an oscilloscope. And, the experimental setup to apply a specific force to fabricated touch sensor at different frequencies consists of a function generator, a power amplifier, a vibration shaker, a linear spring, an optical displacement sensor and an oscilloscope. The touch sensor is located on the vibration shaker which is vibrating at different frequencies and amplitudes which could be controlled by the function generator. In other words, the signal function generator is used

to drive vibration shaker with a sinusoidal signal. The touch sensor is with contact to the linear spring from the top which leads to applying a force to it which is proportional to the deformation of the spring. And, the deformation of the spring could be measured using the optical displacement sensor's probe and is transferred to a voltage output signal. Finally, both generated voltages by the touch sensor which has been amplified by the non-inverting amplifier and the optical displacement sensor could be visualized and recorded by the oscilloscope. A schematic view of the experimental rig is given in Figure 6.2.

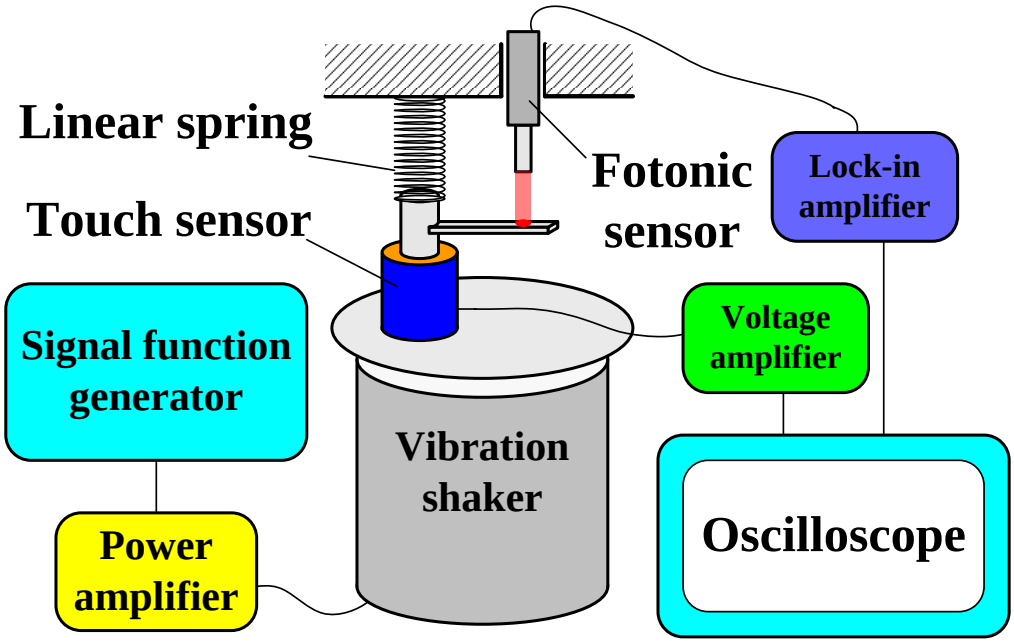

Figure 6.2. The schematic view of the experimental rig for applying an arbitrary force to the fabricated touch sensor at different frequencies.

6.2 RESULTS AND DISCUSSIONS

Nafion 117 membrane with the thickness of 170 µm is utilized as the ionic polymer layer. A layer of gold is sputtered on each side of the Nafion after cleaning, proton exchange and drying process

using DC sputtering in a sputter coater (Cressington Sputter Coater 108auto). Checking the surface of the gold sputtered polymer using Tencor Alpha-Step IQ surface profiler shows that the thickness of the gold electrode layer is about 100 nm. And, the surface resistance of fabricated IPMC is 0.9 Ω/cm on each surface. Next, for diluent uptake, the gold electrode coated Nafion is soaked in EmI-Tf for 7 hours. The IPMC segment which is being used in monitoring human pulse wave is rectangular with dimensions of 7×8 mm. This IPMC segment is attached perfectly to the wrist directly upon the radial artery using some strapping tape as shown in Figure 6.3. Attaching the IPMC segment at this position exposes it to the deformation of the wrist due to blood pulse wave.

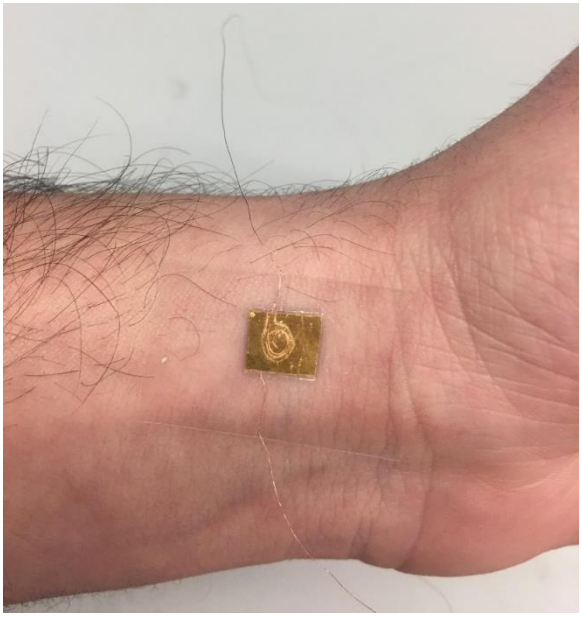

Figure 6.3. Photograph of wearable sensor directly attached to the wrist.

Generated voltage by the fabricated touch sensor amplified by a non-inverting amplifier with $R_f = 10\ k\Omega$ and $R_2 = 1\ k\Omega$, i.e. amplification gain of 11, and visualized and recorded by an oscilloscope. The equivalent parallel capacitance and resistance of the fabricated IPMC segment,

using Agilent 4294A precision impedance analyzer, was 262 nF and 41.2 kΩ, respectively. Therefore, the time constant of the strain sensor which is coupled with the non-inverting voltage amplifier is 10.8 ms, according to (5.2), which is small enough for measurement of heart beat pulse wave.

The voltage signal of the wearable blood pulse wave sensor for a 29 years old sample before and after exercise and a 56 years old sample is recorded for 6 seconds and shown in Figure 6.4. The amplitude, frequency and shape of pulse wave can be read out readily in real time. Figure 6.4 clearly shows that the normal pulse frequency of the 29-year old person is 75 beats per min with regular and repeatable pulse shape and this pulse frequency after exercise increases to 85 beats per min with a little enhancement of the amplitude. And, the normal pulse frequency of the 56-year old person is 65 beats per min with regular and repeatable pulse shape.

Another observation to point out is the shape of each blood pulse wave for two different people. As can be seen in Figure 6.4(a), there are two peaks for each pulse: a big and a small one. The bigger one is due to systole pressure and the smaller one coming from diastole pressure. In older individuals with reduced arterial compliance, early return of peripherally reflected waves increases pulse pressure, produces a late systolic pressure peak, attenuates the diastolic pressure wave and at times, distorts the smooth upstroke with an early systolic hump [95]. This medical phenomenon could clearly be seen in Figure 6.5 which compares one individual pulse bit of each sample with the theoretical pulse waves reported in the medical literature [95].

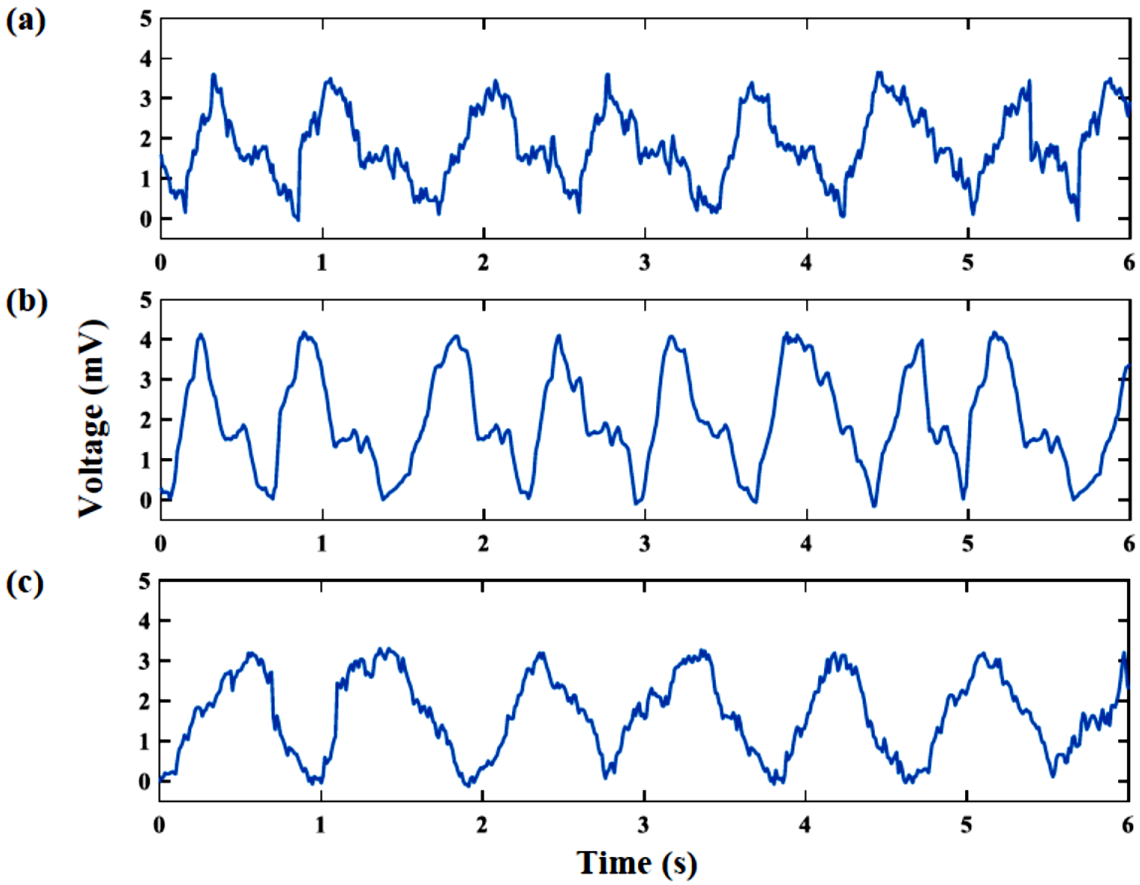

Figure 6.4. Voltage response of the wearable blood pulse wave sensor on the wrist for (a) the 29-year old sample before exercise (b), the 29-year old sample after exercise and (c) 56-year old sample.

A circular IPMC segment with a radius of 11.5 mm is used in the touch sensor. This IPMC segment is located on a solid cylinder with the same radius and 13 mm long which is filled with silicone rubber. Finally, IPMC disk is protected with a polyamide sheet with the thickness of 50 μm. The fabricated IPMC touch sensor is shown in Figure 6.6.

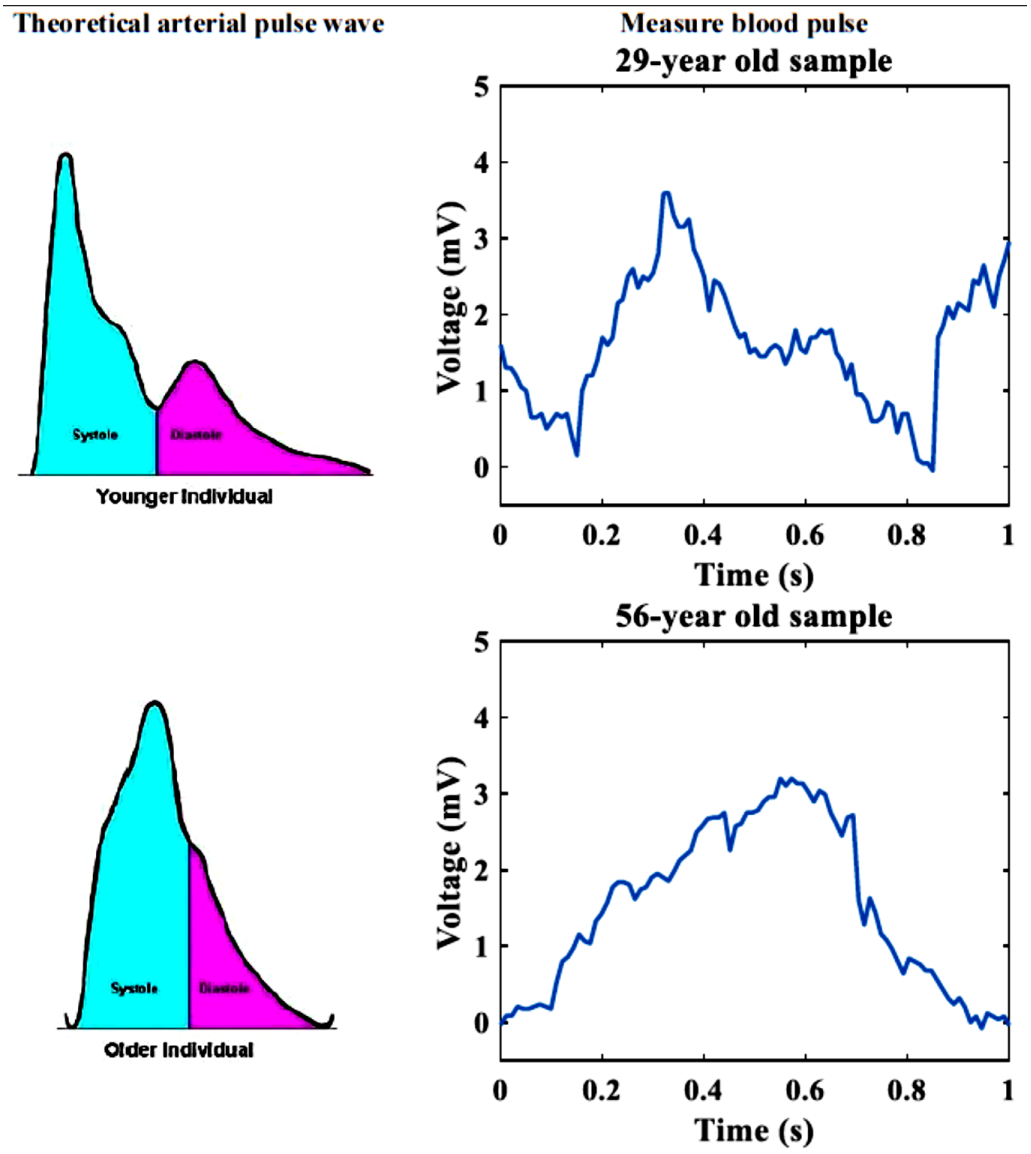

Figure 6.5. Comparison of measured blood pressure pulses with the theoretical ones.

The advantage of using silicone rubber under the IPMC disk is to make it stable and reliable under different external pressures due to touch and to let it deform linearly in an acceptable range which is the main reason of voltage generation. Figure 6.7 shows the stress-strain curves resulting from ramp tests in uniaxial and plane strain compression for silicone rubber [96]. As can be seen in this figure, there is almost a linear relationship between applied external force and compression

of silicone rubber for deformations less than 30% which makes the whole touch sensor structure behave as a circular plate on an elastic foundation. In other words, one can expect a linear relation between applied force and the generated voltage.

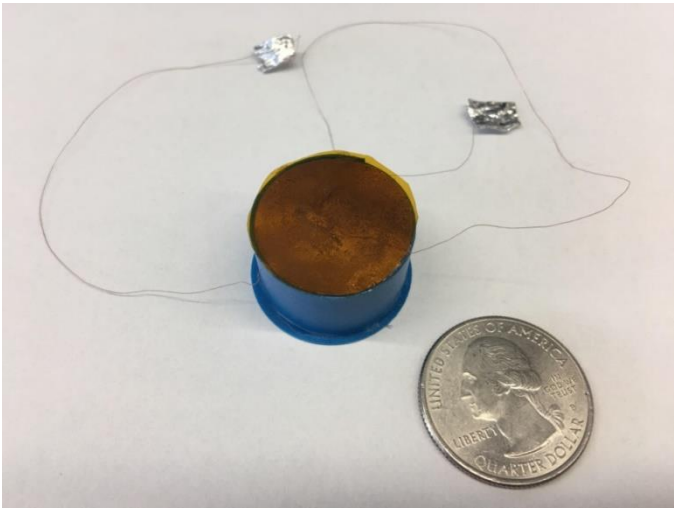

Figure 6.6. Fabricated touch sensor.

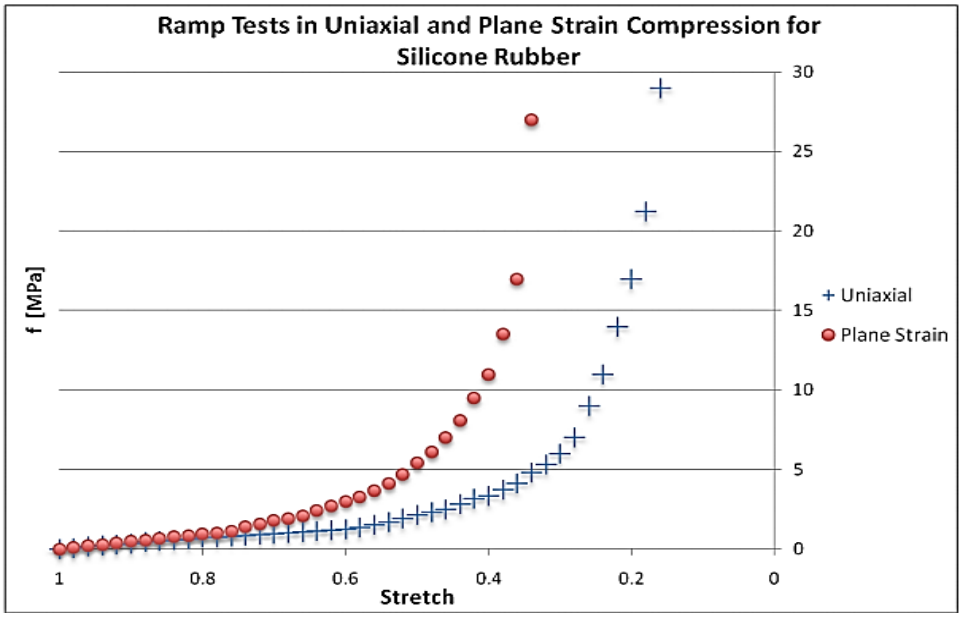

Figure 6.7. Stress-strain curve for silicon rubber [96]

To characterize the response of the fabricated touch sensor under different forces and at different frequencies, it is located on the LDS vibration shaker under a metal circular cylinder of radius 5 mm connected to a linear spring with the stiffness of 2kN/m. The displacement of the vibration shaker is controlled by an SRS model DS345 function generator and generated signal is fed to the vibration shaker through an LDS PA25E power amplifier. Displacement of the touch sensor leads to spring's deformation and consequently, a vertical force which is proportional to the spring's deformation would apply to the sensor. Spring's deformation is measured by an MTI 2000 Fotonic sensor. Generated voltage by the fabricated touch sensor amplified by a non-inverting amplifier with $R_f = 10\ k\Omega$ and $R_2 = 1\ k\Omega$, i.e. amplification gain of 11. The equivalent parallel capacitance and resistance of the utilized circular IPMC segment, using Agilent 4294A precision impedance analyzer, was 613 nF and 22.8 kΩ, respectively. Therefore, the time constant of the strain sensor which is coupled with the non-inverting voltage amplifier is 14 ms, according to (5.2), which is small enough for measurement of regular human touch signals. The experimental rig which is used for this test is shown in Figure 6.8.

The electrical response of the IPMC touch sensor due to applied vertical sinusoidal touch force of 1 N for excitation frequencies between 1 and 10 Hz is given in Figure 6.9. As one can see in this figure, increasing the frequency of touching force in the range of real applied forces does not have a meaningful effect on the sensitivity.

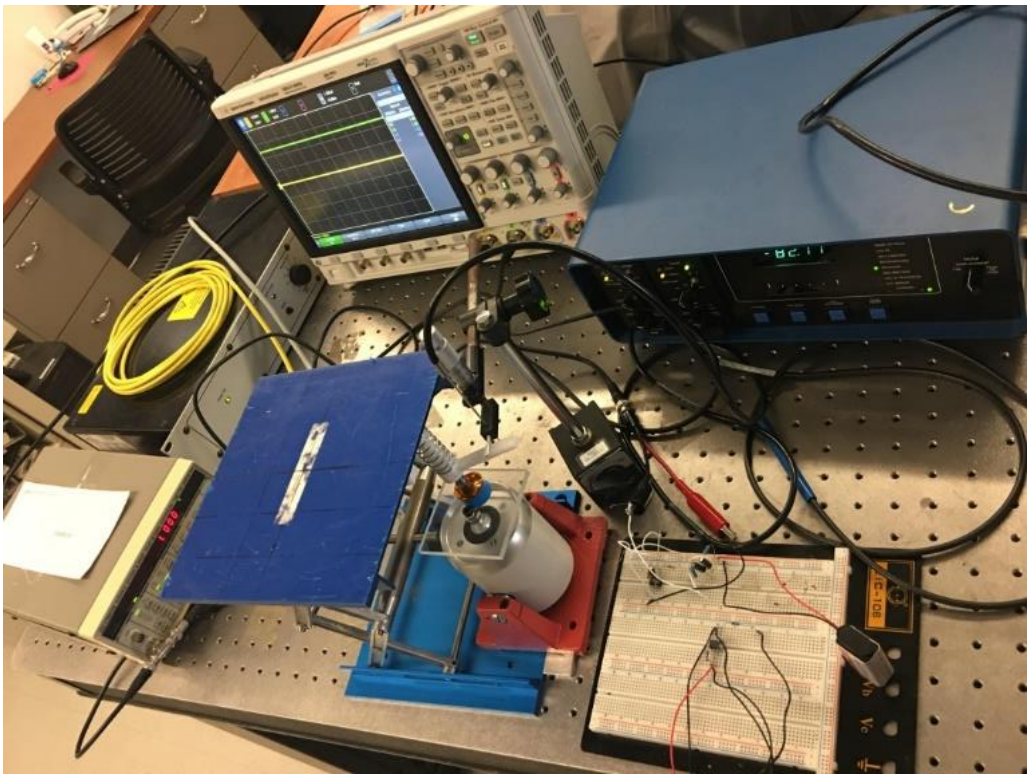

Figure 6.8. Experimental setup which is used for touch sensor sensitivity test.

Figure 6.10 shows the electrical response of the IPMC touch sensor as a function of frequency. This figure shows that the effect of frequency on sensitivity, which is meaningful for a wide range of frequencies, is negligible for a touch sensor which is working in a low-frequency rage.

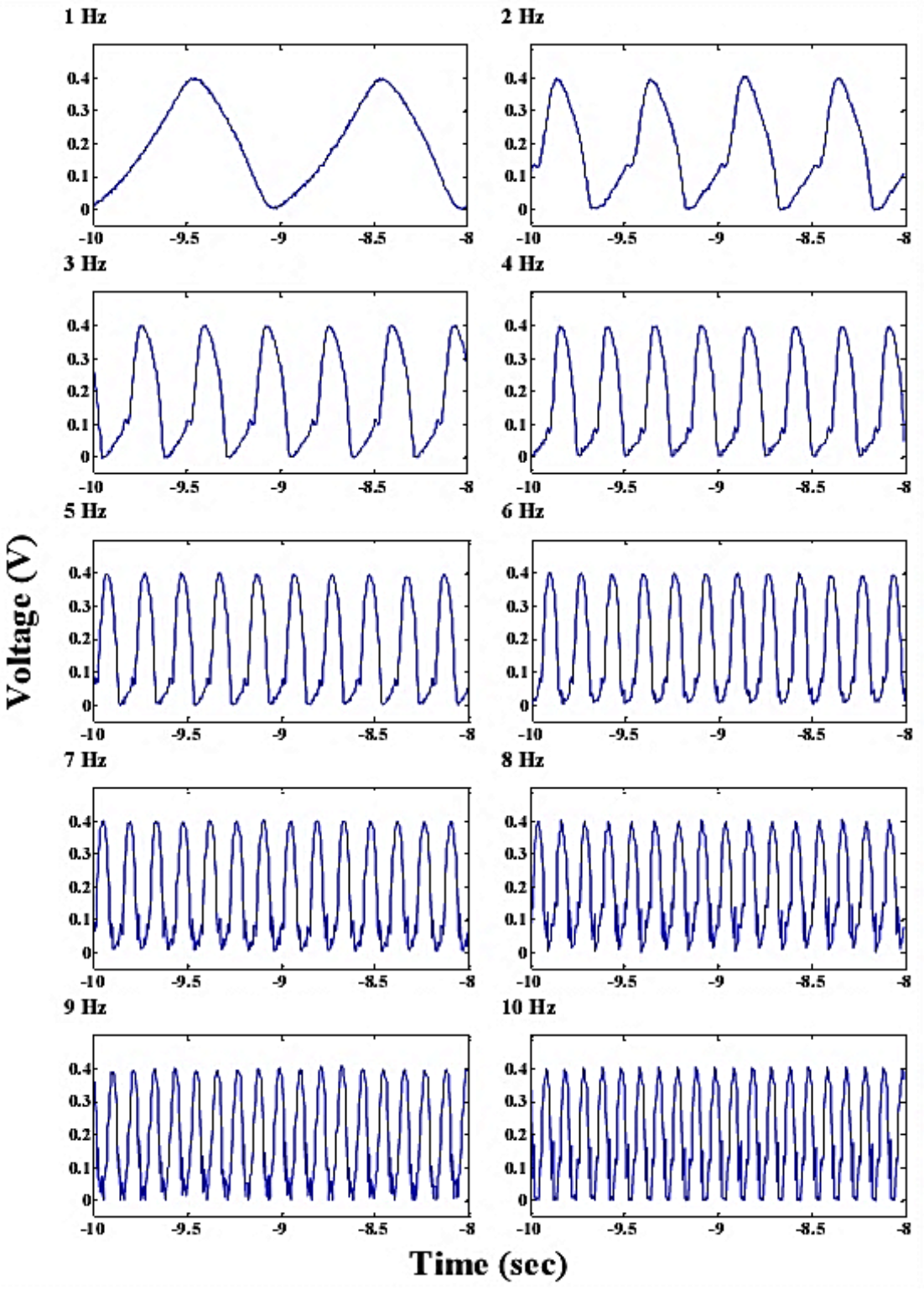

Figure 6.9. Electrical response of the IPMC touch sensor under a single sinusoidal excitation for 1 N touch force.

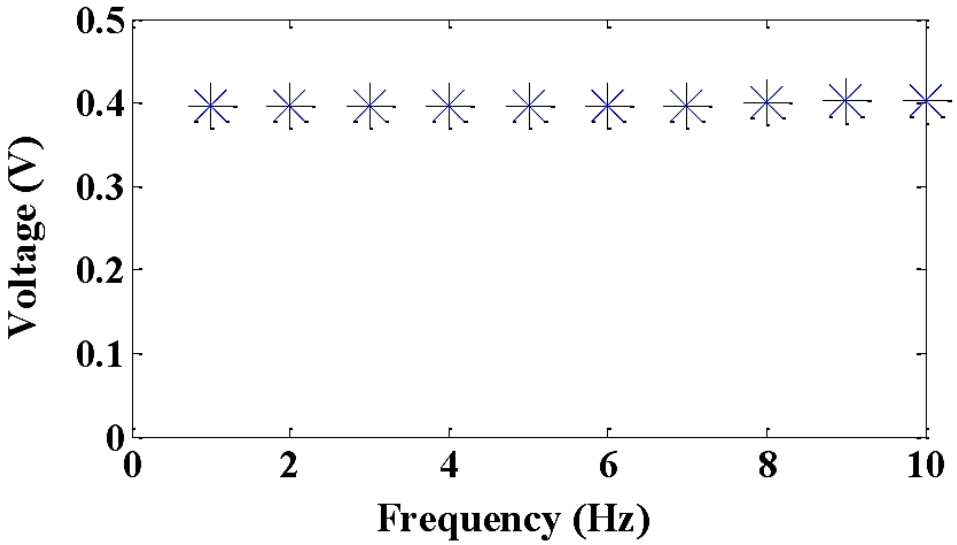

Figure 6.10. Electrical response of the IPMC touch sensor as a function of frequency.

Figure 6.11 shows the effect of applied touch force to fabricated IPMC touch sensor's generated voltage. As the touch force increases, more charges are generated and a higher voltage could be measured as the output. Based on Figure 6.11, at higher forces saturation happens and generated voltage does not increase linearly. This saturation behavior may limit the sensitivity of IPMC touch sensors. This phenomenon could be justified with two main reasons: the first one is saturation of IPMC disc under this specific deformation and the second one is the nonlinear effect of silicone substrate which has higher elastic modulus for higher deformations.

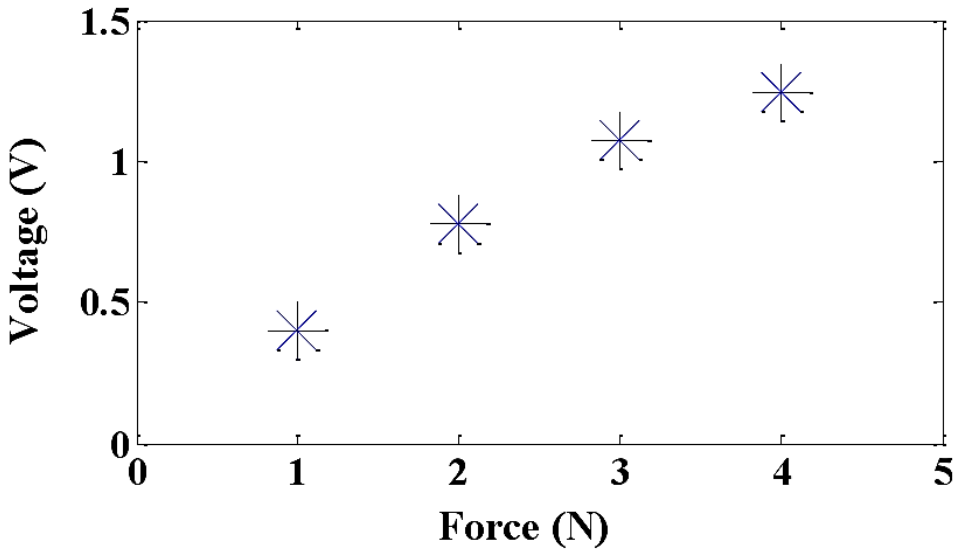

Figure 6.11. Electrical response of the IPMC touch sensor as a function of applied force.

To further understand the response of the fabricated IPMC touch sensor, the touch device was pressed at a wide range of forces and signals, as shown in Figure 6.12. According to this figure, different signals could be generated by applying different finger touch forces to the fabricated IPMC touch sensor. The other phenomenon to point out is the drain current which happens in IPMC sensors. The generated charge on electrode drains to the other side due to low internal resistance which could be easily observed in generated voltage of IPMC touch sensor for step finger touch scenario. For this reason, IPMCs are not appropriate for being used in static sensors.

According to presented results, fabricated IPMC touch sensor due to its capability to generate a reliable electrical voltage under finger pressure is an appropriate candidate to be used in a touch sensor on-off switch circuit based on piezoelectricity. For this purpose, the IPMC touch sensor is used to sense the touch action and a decade counter IC 4017 is used to toggle the output for successive touch actions, Figure 6.13.

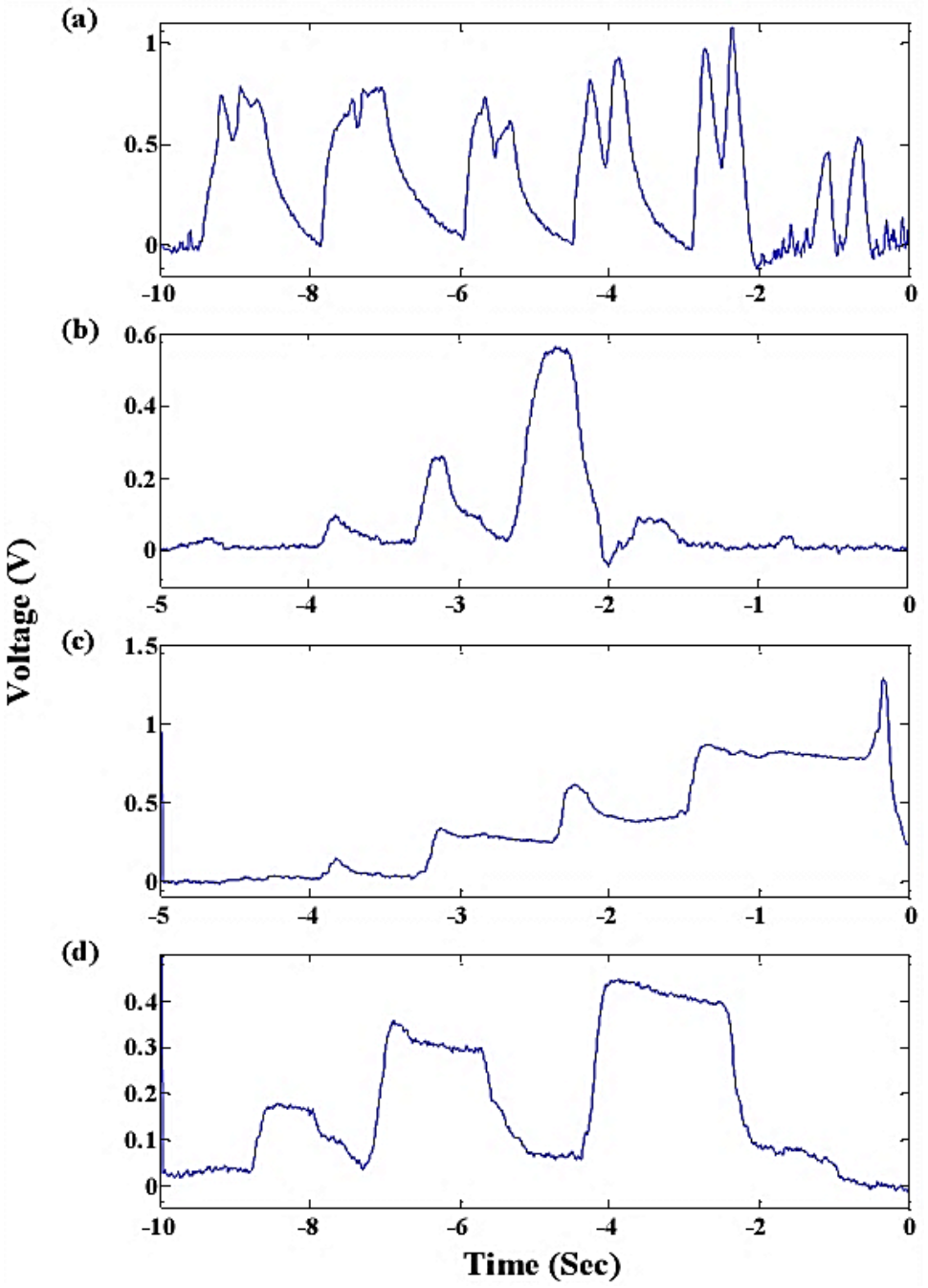

Figure 6.12. Generated voltage of IPMC touch sensor in response to (a) cyclic two times finger touch (b) cyclic single finger touch with different forces (c) step finger touch by increasing the force (d) finger touch with repetitive press/release sequences with in different forces.

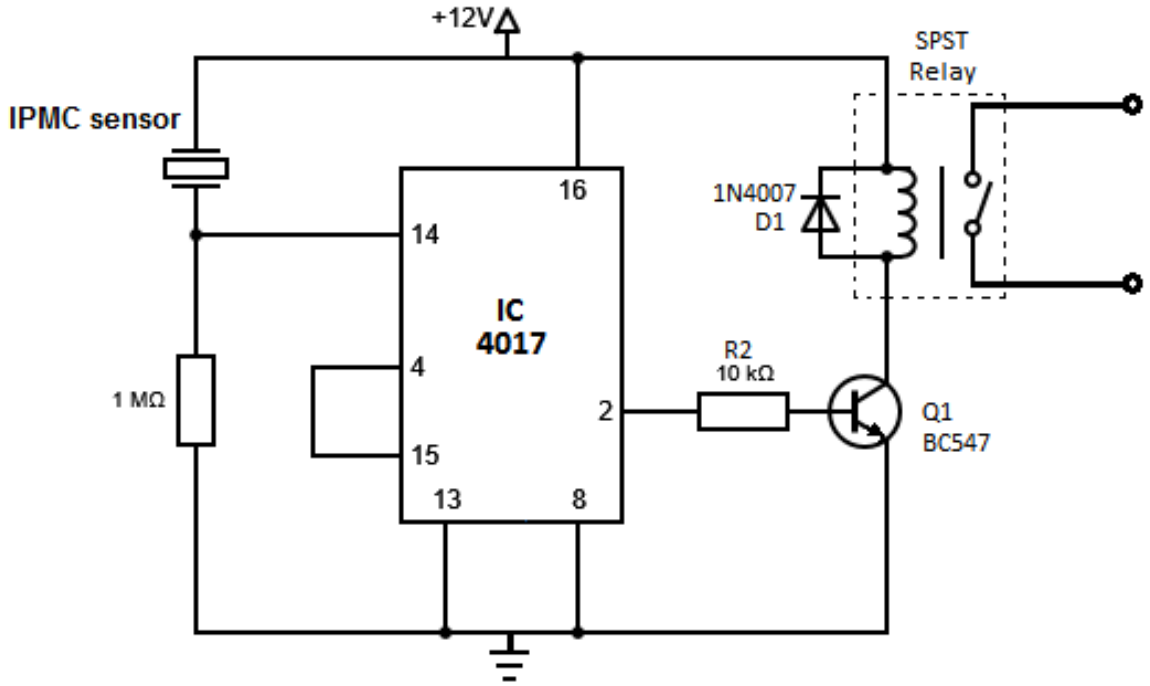

Figure 6.13. The circuit of IPMC touch sensor on-off switch.

The clock input of the Decade IC has a positive edge triggering. Thus, the output pin holds the state till another edge trigger occurs. The output pin has taken from output 2. It shifts the ON state from output 1 to output 2 on the positive edge trigger. The reset pin 15 of the IC has connected to the pin 4 (output 3 of the decade counter). So, it resets the counter on next triggering. Thus, the ON and OFF state repeats for consecutive touch actions on the sensor. Moreover, the output from the IC has connected to a transistor, which drives the Relay. The sensitivity of the touch can be adjusted by varying the resistor connected across the pin 14.

Figure 6.14 shows the developed IPMC touch sensor which is connected to the on-off switch circuit to change the state of an LED light upon each finger touch. The fabricated touch switch kept working after more than 200 cycles, revealing the high repeatability and stability.

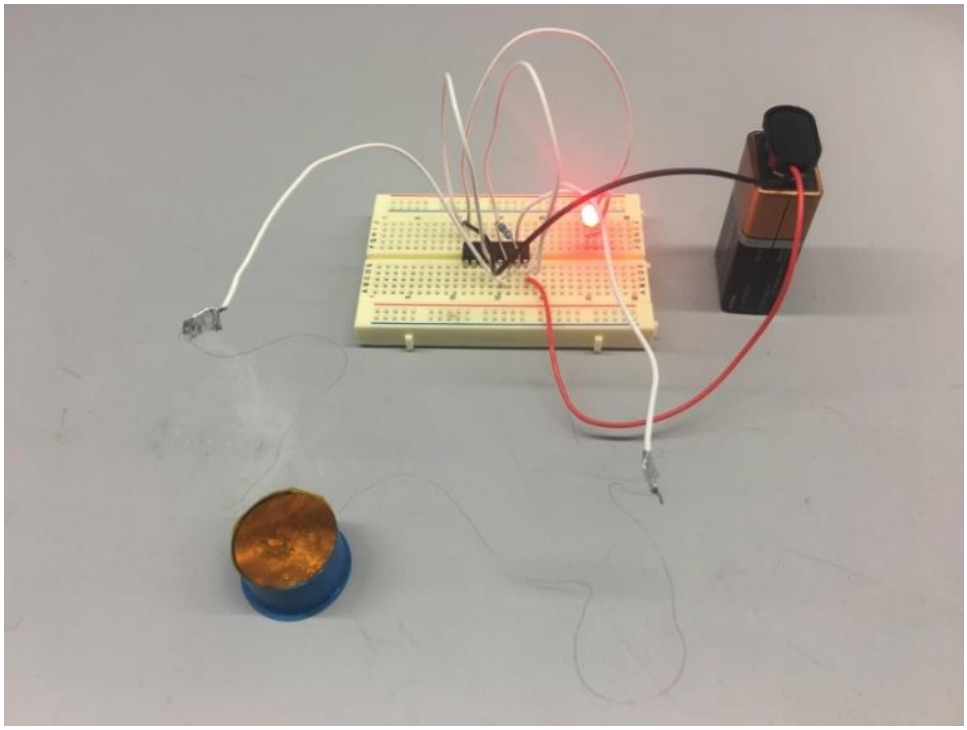

Figure 6.14. IPMC touch sensor connected to the on-off switch circuit

Furthermore, to limit the bending deformation of the IPMC sensor and consequently the generated voltage in order to be more appropriate for on-off switch application, a flexible polymer cap with the diameter of 20 mm and depth 5 mm is designed and 3D printed. A 10×15 mm rectangular IPMC segment is attached to the inner surface of the cap while it is bent normally. Soft cap and attached IPMC segment become flat due to external touching of the switch and a signal is generated while the deformation is limited to the dimension of the cap and the IPMC segment is not able to be deformed inversely. The soft polymer switch is placed in solid frame with a circular hole on it which has been fabricated by 3D printing. The schematic structure and fabricated proposed touch switch are shown in Figure 6.15(a) and Figure 6.15(b), respectively.

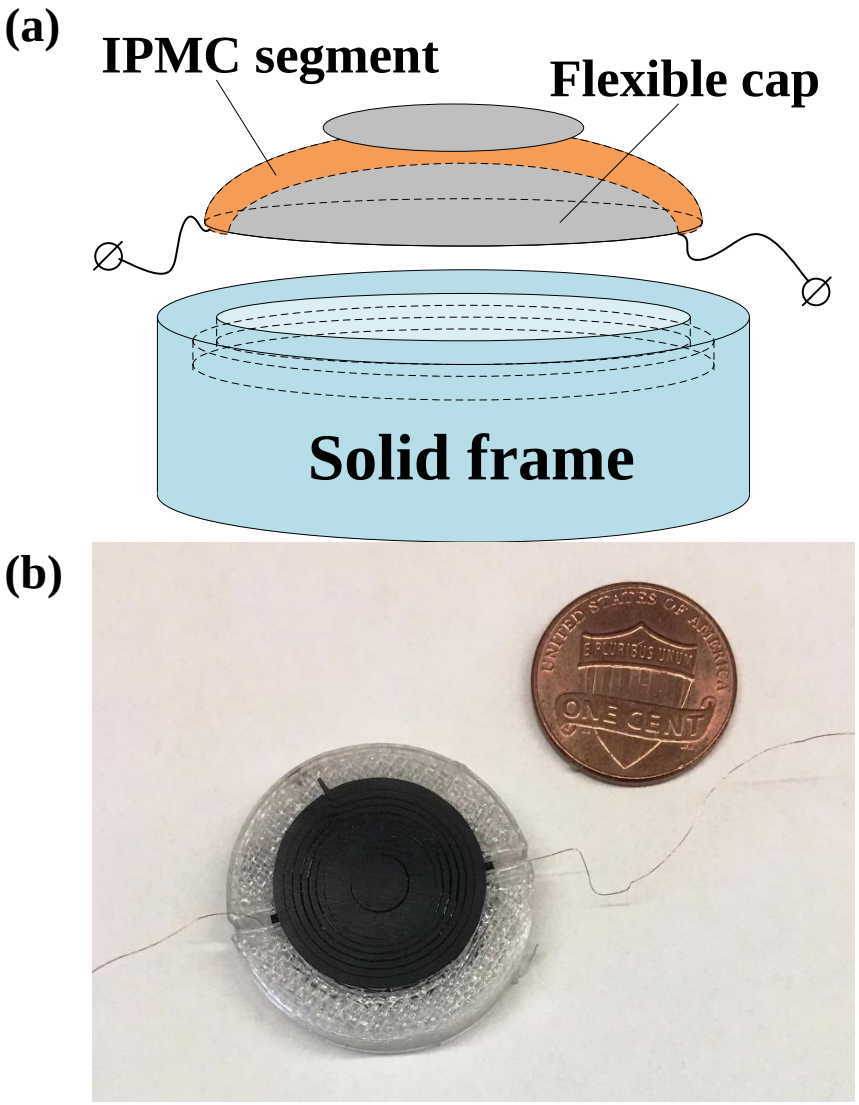

Figure 6.15. (a) The schematic structure and (b) fabricated proposed touch switch.

To make sure that the generated voltage by IPMC sensors under in-plane tension is negligible with respect to the one obtained due to bending, a 15×30 mm rectangular IPMC layer is fixed at one edge and a specific distributed step force is applied to the opposite edge, as it is given in Figure 6.16. Generated signals due to 2 N, 5 N and 10 N step forces with respect to time are illustrated in Figure 6.17.

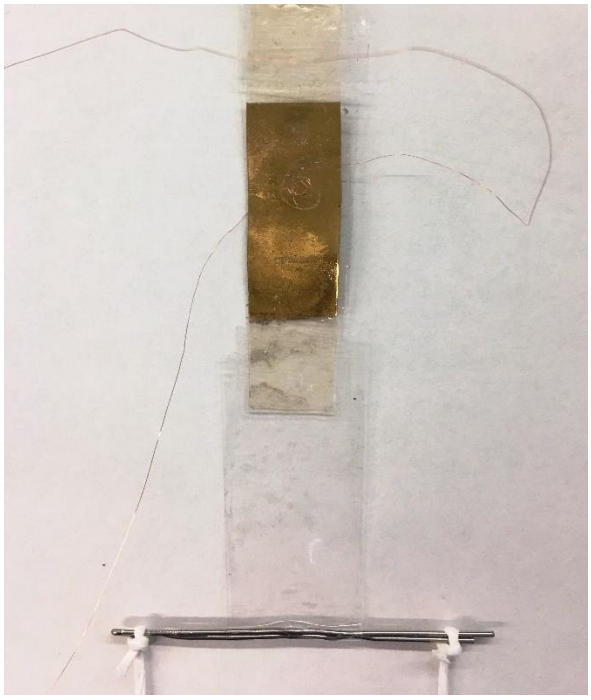

Figure 6.16. An IPMC rectangular segment under tension.

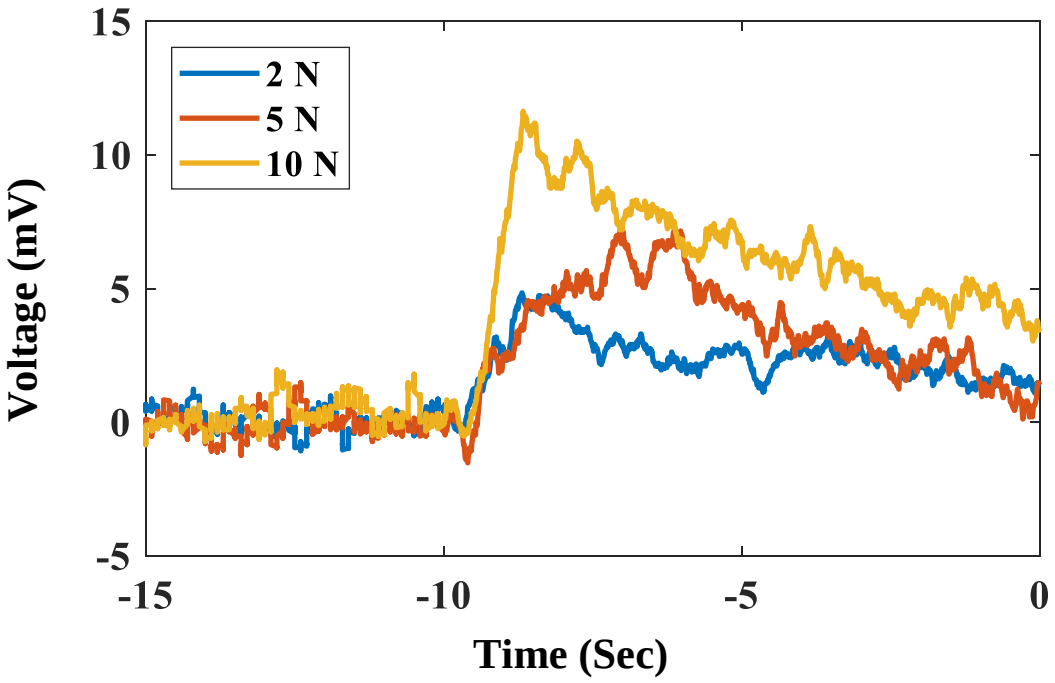

Figure 6.17. Generated voltage by the rectangular IPMC segment under tension with different forces.

As it can be seen in Figure 6.17, generated voltages due to in-plane tension are negligible in comparison with bending mode signals, even for bigger IPMC segments and higher tension forces. And, the generated voltage in the proposed touch switch is only due to the bending deformation. To illustrate the efficiency of the proposed on-off IPMC touch sensor, the touch device was pressed at a wide range of signals, as shown in Figure 6.18. According to this figure, different shapes could be generated according to the speed of the touch but all of them are located in a specific range which is about 0.4 volt after an amplification of 11 for this specific design.

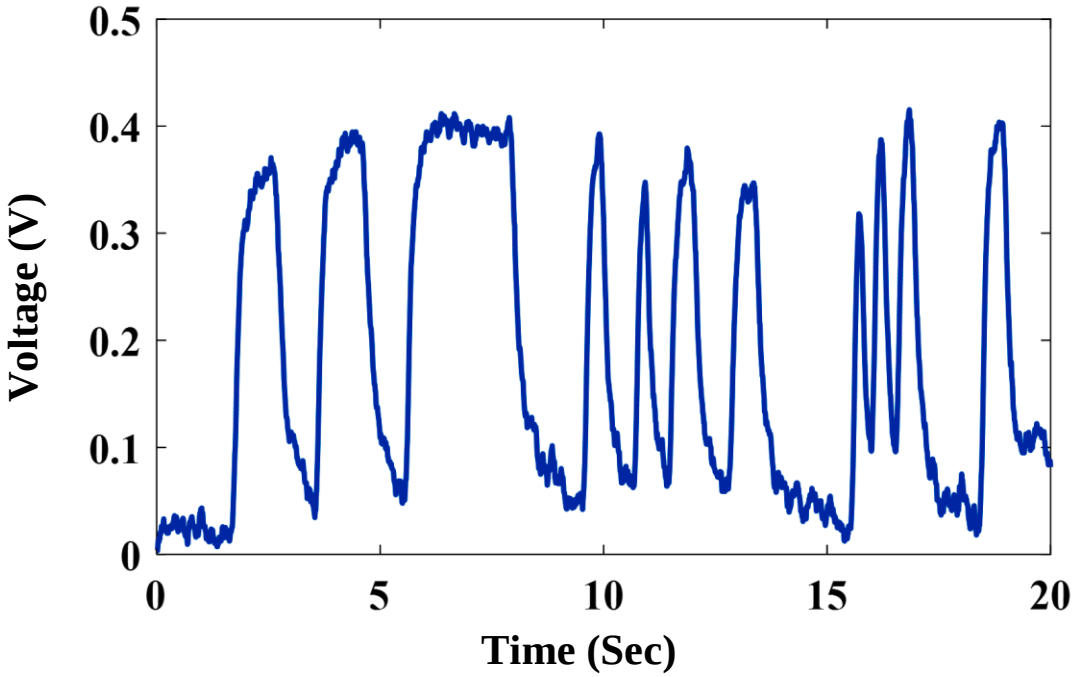

Figure 6.18. Generated voltage of IPMC touch sensor in response to different finger touches.

7.0 CONCLUSIONS

In the first part of this dissertation, IPMC transducers in bending, compression and shear modes were used to develop dynamic pressure sensors and these three types of sensor were calibrated and compared experimentally in a standard shock tube. Electric current generation on electrodes was investigated theoretically based on streaming potential hypothesis. Afterward, DAP was employed to fabricate some samples of each type of pressure sensor which were used in the impedance analyzer to estimate equivalent capacitances and resistances and to design an appropriate signal conditioner. Then, several tests using shock tube setup were done to compare the IPMCs generated voltages to ones from a commercial pressure sensor. Evaluating generated charges with respect to applied pressures for all three fabricated sensors of each type showed a decent linearity as well as a high sensitivity. In addition, comparing the results for different samples exhibits the consistency of DAP as fabrication process, respectively.

In the second part of this dissertation, three explicit, dynamic, physics-based, rational transfer functions for ionic polymer-metal composite (IPMC) pressure sensors in compression, shear and bending modes which are appropriate to be used in real-time applications were developed. IPMC governing PDE was solved for pressure sensors in different modes in the Laplace domain subject to the condition that the charge density at the boundaries is proportional to the applied stress. Obtained models not only provide a valuable insight into the sensing mechanism of IPMCs but also are suitable for analysis and design set of system-theoretic tools. Some

experiments were done to validate the proposed dynamic model for IPMC pressure sensors. Some impulse stimulations were applied by utilizing a standard shock pressure tube setup which is an appropriate source with a known amplitude of the pressure and a small raise time in experimental tests. Finally, both time and frequency responses of three types of fabricated pressure sensors were presented and compared to results obtained from derived IPMC pressure sensor model. The results show a good agreement between proposed model's predictions and measured sensing responses of corresponding fabricated sensors. Moreover, different values of proportional constants for different modes of deformation show activation of different micro-channels in the IPMC for dissimilar modes and different mechanisms of charge generations. Consequently, all transfer functions are high-pass filters that prove the fact that IPMCs are not useful for static purposes although they are appropriate for being used as dynamical sensors.

In the third part, some highly flexible acrylic coated IPMC segments were fabricated using gold sputtering and their ability to maintain sensor properties over time were investigated experimentally using a standard shock tube. Streaming potential hypothesis showed that how an external force is able to generate charge on an IPMC sensor's electrodes in any mode of deformation. Next, some IPMC segments, both acrylic coated and uncoated, were fabricated which were used in impedance analyzer to estimate equivalent capacitance and resistance and design an appropriate signal conditioner. Then, several tests using shock tube setup were done to compare IPMC's generated voltages in different modes of deformation to ones from a commercial pressure sensor during 6 days from fabrication. Analyzing generated charges with respect to applied external impulses for all modes of deformation showed a decent linearity as well as a high sensitivity. Existing diluent liquid in IPMCs led to a faster transient response damping than the commercial pressure sensor based on piezoelectric materials and different transient responses of

IPMC segments under different deformations originated from different boundary conditions. Also, different sensitivities of IPMCS in different modes could be explained by the different number of nano-channels which are activated and the effectiveness of channels' alignments. Furthermore, repeating impulse experiments over a six-day period of time after fabrication and comparing the results to the uncoated ones proved that coating IPMC segment with waterproof Sprayon EL 2000 Clear Acrylic Sealer could maintain the sensor properties efficiently.

In the fourth study, proposed highly flexible IPMC sensors were used in the fabrication of a wearable plantar pressure distribution system to detect electric signals which are proportional to the foot pressure. Eight IPMC pressure sensors were placed in the separate anatomical regions of the foot to be able to calculate foot dynamics accurately while each sensor is connected to a separate signal conditioner with two insulated wires. Examinations were carried out in a natural environment on a subject for static stance, walking and running. Acquired time series data were used for calculation of time differences, durations and the maximum mean peak signals of the landing of rear-foot, mid-foot and fore-foot as well as time percentages of stance and swing phases of both walking and running cycles. Moreover, the foot pressure distribution maps for static stance and walking and running dynamic stance phases at different time points correspond to the foot fall on and off the ground were displayed by some colormaps and the reasonability of results was discussed. Consequently, the reliability of the proposed insole was evaluated by comparing the pressure distribution results of walking cycle with a commercial Matscan system which is presented in the literature, offered a good agreement and showed the reliability of IPMCs for wearable plantar pressure measurement applications. In a word, proposed highly flexible IPMCs sensors offer high-sensitivity and dynamic range, good repeatability, flexibility and comfort which make them proper to fit on various wearable applications, such as monitoring daily activity and

exercise with motion, assessing the balance and gait disorders in older adults and outpatients after appropriate calibrations.

In the last part, proposed highly flexible IPMC layers were used as a blood pulse wave sensor as well as a touch sensor. A non-inverting voltage amplifier was used to amplify the generated voltage by the sensor and to eliminate the effect of changing of IPMC's internal resistance under deformation. Through simple encapsulation using strapping tape, the IPMC segment was directly attached to human's skin for the real-time measurement of the human subtle pulse wave. The voltage signal of the wearable blood pulse wave sensor for a 29 years old sample before and after exercise and a 56 years old sample were recorded for 6 second and the amplitude, frequency and shape of it shown a good agreement with medical expectations. Moreover, a self-powered soft touch sensor using a flexible IPMC disk is located on a solid cylinder filled with silicone rubber and protected by a layer of polyamide was developed. Investigation of the effect of exciting frequency on the sensitivity at low frequencies showed that this effect is negligible. Moreover, there is almost a linear relationship between applied touch force and the generated voltage. Likewise, the touch device was pressed at a wide range of forces and signals which demonstrated its capability to produce a various type of electrical signals. Finally, the developed touch sensor was used in a touch sensor on-off switch circuit based on piezoelectricity and showed an appropriate performance. Finally, the 3D printing was hired to fabricate a flexible cap in order to limit the deformation of the IPMC segment and the generated voltage in a specific range and enhance the effectiveness of the proposed touch sensor for on-off switches.

8.0 FUTURE WORKS

Based on the research conducted in this dissertation, following recommendations could be made as future works:

- Experimental investigation on the effect of electrodes' asymmetricity both for structure and thickness.
- Design of sensor structures which use more than one mode of deformation for sensing, e.g. Bending and shear.
- Take advantage of the unique property of IPMCs to develop sensors which are able to measure the direction of the applied force or deformation as well as its magnitude.
- Improvement of the proposed biomedical IPMC sensors for remote medical monitoring by adding a Reader of the Transceiver Telemetry System (TTS) which receives data from the sensors through RF signals.

BIBLIOGRAPHY

[1] B. Bhandari, G.-Y. Lee, and S.-H. Ahn, "A review on IPMC material as actuators and sensors: Fabrications, characteristics and applications," *International Journal of Precision Engineering and Manufacturing*, vol. 13, no. 1, pp. 141–163, 2012.

[2] D. N. C. Nam and A. K. Kwan, "Ionic Polymer Metal Composite Transducer and Self-Sensing Ability," in *Smart Actuation and Sensing Systems-Recent Advances and Future Challenges*: InTech, 2012, pp. 203-222.

[3] Y. Bar-Cohen, *Electroactive polymer (EAP) actuators as artificial muscles: reality, potential, and challenges*. Bellingham: SPIE Press, 2004.

[4] Z. Min, M. Gudarzi, and Q.-M. Wang, "Modeling, fabrication and analysis of a flexible PZT-polymer laminated composite cantilever beam in sensing and actuation modes," in *2017 IEEE International Ultrasonics Symposium (IUS)*, Washington, DC, USA, 2017: IEEE.

[5] K. Oguro, Y. Kawami, and H. Takenaka, "Bending of an ion-conducting polymer film-electrode composite by an electric stimulus at low voltage," *Journal of Micromachine Society*, vol. 5, pp. 27-30, 1992.

[6] M. Shahinpoor, "Conceptual design, kinematics and dynamics of swimming robotic structures using ionic polymeric gel muscles," *Smart Materials and Structures*, vol. 1, no. 1, p. 91, 1992.

[7] K. Sadeghipour, R. Salomon, and S. Neogi, "Development of a novel electrochemically active membrane and 'smart' material based vibration sensor/damper," *Smart Materials and Structures*, vol. 1, p. 172, 1992.

[8] Z. Chen, Y. Shen, N. Xi, and X. Tan, "Integrated sensing for ionic polymer-metal composite actuators using PVDF thin films," *Smart Materials and Structures*, vol. 16, pp. S262–S271, 2007.

[9] S. Tadokoro, S. Yamagami, and M. Ozawa, "Soft micromanipulation device with multiple degrees of freedom consisting of high polymer gel actuators," in *Technical Digest. IEEE International MEMS 99 Conference. Twelfth IEEE International Conference on Micro Electro Mechanical Systems*, Orlando, FL, USA, 1999, pp. 37-42: IEEE.

[10] Z. Chen, S. Shatara, and X. Tan, "Modeling of biomimetic robotic fish propelled by an ionic polymer-metal composite caudal fin," *IEEE/ASME Transactions on Mechatronics,* vol. 15, no. 3, pp. 448-459, 2010.

[11] M. Aureli, V. Kopman, and M. Porfiri, "Free-locomotion of underwater vehicles actuated by ionic polymer metal composites," *IEEE/ASME Transactions on Mechatronics,* vol. 15, no. 4, pp. 603 - 614, 2010.

[12] C. Bonomo, L. Fortuna, P. Giannone, S. Graziani, and S. Strazzeri, "A resonant force sensor based on ionic polymer metal composites," *Smart Materials and Structures,* vol. 17, no. 1, p. 015014, 2007.

[13] U. Zangrilli and L. M. Weiland, "Prediction of the ionic polymer transducer sensing of shear loading," *Smart Materials and Structures,* vol. 20, no. 9, p. 094013, 2011.

[14] Y. Bahramzadeh and M. Shahinpoor, "Dynamic curvature sensing employing ionic-polymer–metal composite sensors," *Smart Materials and Structures,* vol. 20, no. 9, p. 094011, 2011.

[15] M. Aureli, C. Prince, M. Porfiri, and S. D. Peterson, "Energy harvesting from base excitation of ionic polymer metal composites in fluid environments," *Smart Materials and Structures,* vol. 19, no. 1, p. 015003, 2009.

[16] S. D. Peterson and M. Porfiri, "Energy exchange between a vortex ring and an ionic polymer metal composite," *Applied Physics Letters,* vol. 100, no. 11, p. 114102, 2012.

[17] M. Shahinpoor, Y. Bar-Cohen, J. O. Simpson, and J. Smith, "Ionic polymer-metal composites (IPMCs) as biomimetic sensors, actuators and artificial muscles - a review," *Smart Materials and Structures,* vol. 7, no. 6, pp. R15-30, 1998.

[18] K. M. Newbury and D. J. Leo, "Electromechanical modeling and characterization of ionic polymer benders," *Journal of Intelligent Material Systems and Structures,* vol. 13, no. 1, pp. 51-60, 2002.

[19] C. Bonomo, L. Fortuna, P. Giannone, S. Graziani, and S. Strazzeri, "A model for ionic polymer metal composites as sensors," *Smart Materials and Structures,* vol. 15, no. 3, pp. 749-758, 2006.

[20] F. Gao and L. M. Weiland, "The streaming potential method for modeling the electromechanical responses of ionic polymer transducers," in *Sensors and Smart Structures Technologies for Civil, Mechanical, and Aerospace Systems 2009*, 2009, p. 72924H: SPIE.

[21] B. Kocer and L. M. Weiland, "Experimental investigation of the streaming potential hypothesis for ionic polymer transducers in sensing," *Smart Materials and Structures,* vol. 22, no. 3, p. 035020, 2013.

[22] B. Kocer, U. Zangrilli, B. Akle, and L. Weiland, "Experimental and theoretical investigation of ionic polymer transducers in shear sensing," *Journal of Intelligent Material Systems and Structures,* vol. 26, no. 15, pp. 2042-2054, 2014.

[23] G. D. Pasquale, S. Graziani, A. Pollicino, and S. Strazzeri, "A vortex-shedding flowmeter based on IPMCs," *Smart Materials and Structures,* vol. 25, no. 1, p. 015011, 2015.

[24] I. Dominik, J. Kwaśniewski, and F. Kaszuba, "Ionic polymer-metal composite displacement sensors," *Sensors and Actuators A: Physical,* vol. 240, pp. 10-16, 2016.

[25] V. Volpini, L. Bardella, A. Rodella, Y. Cha, and M. Porfiri, "Modelling compression sensing in ionic polymer metal composites," *Smart Materials and Structures,* vol. 26, no. 3, p. 035030, 2017.

[26] W. Hong, A. Almomani, and R. Montazami, "Electrochemical and morphological studies of ionic polymer metal composites as stress sensors," *Measurement,* vol. 95, pp. 128-134, 2017.

[27] P. Brunetto, L. Fortuna, P. Giannone, S. Graziani, and S. Strazzeri, "Characterization of the temperature and humidity influence on ionic polymer-metal composites as sensors," *IEEE Transactions on Instrumentation and Measurement,* vol. 60, no. 8, pp. 2951-2959, 2011.

[28] H. Lei, C. Lim, and X. Tan, "Humidity-dependence of IPMC sensing dynamics: Characterization and modeling from a physical perspective," *Meccanica,* vol. 50, no. 11, pp. 2663-2673, 2015.

[29] F. Bauer, S. Denneler, and M. Willert-Porada, "Influence of temperature and humidity on the mechanical properties of Nafion® 117 polymer electrolyte membrane," *Journal of Polymer Science Part B: Polymer Physics,* vol. 43, no. 7, pp. 786-795, 2005.

[30] E. Shoji and D. Hirayama, "Effects of humidity on the performance of ionic polymer-metal composite actuators: experimental study of the back-relaxation of actuators," *Journal of Physical Chemistry B,* vol. 111, no. 41, pp. 11915-11920, 2007.

[31] P. Brunetto, L. Fortuna, P. Giannone, S. Graziani, and S. Strazzeri, "Static and dynamic characterization of the temperature and humidity influence on IPMC actuators," *IEEE Transactions on Instrumentation and Measurement,* vol. 59, no. 4, pp. 893-908, 2010.

[32] K. Park, "Characterization of the solvent evaporation effect on ionic polymer-metal composite sensors," *Journal of the Korean Physical Society,* vol. 59, no. 6, pp. 3401-3409, 2011.

[33] Z. Zhu, T. Horiuchi, K. Takagi, J. Takeda, L. Chang, and K. Asaka, "Effects of cation on electrical responses of ionic polymer-metal composite sensors at various ambient humidities," *Journal of Applied Physics,* vol. 120, p. 084906, 2016.

[34] Z. Zhu, T. Horiuchi, K. Kruusamäe, L. Chang, and K. Asaka, "The effect of ambient humidity on the electrical response of ion-migration-based polymer sensor with various cations," *Smart Materials and Structures*, vol. 25, no. 5, p. 055024, 2016.

[35] Z. Zhu, T. Horiuchi, K. Kruusamäe, L. Chang, and K. Asaka, "Influence of ambient humidity on the voltage response of ionic polymer-metal composite sensor," *Journal of Physical Chemistry B*, vol. 120, no. 12, pp. 3215-3225, 2016.

[36] B. Akle and D. J. Leo, "Electromechanical transduction in multilayer ionic transducers," *Smart Materials and Structures*, vol. 13, no. 5, p. 1081, 2004.

[37] J. Barramba, J. Silva, and P. J. C. Branco, "Evaluation of dielectric gel coating for encapsulation of ionic polymer–metal composite (IPMC) actuators," *Sensors and Actuators A: Physical*, vol. 140, no. 2, pp. 232-238, 2007.

[38] S. J. Kim, I. T. Lee, H.-Y. Lee, and Y. H. Kim, "Performance improvement of an ionic polymer–metal composite actuator by parylene thin film coating," *Smart Materials and Structures*, vol. 15, no. 6, p. 1540, 2006.

[39] HongLei, WenLi, and X. Tan, "Encapsulation of ionic polymer-metal composite (IPMC) sensors with thick parylene: Fabrication process and characterization results," *Sensors and Actuators A: Physical*, vol. 217, pp. 1-12, 2014.

[40] R. Kanno, S. Tadokoro, T. Takamori, M. Hattori, and K. Oguro, "Linear approximate dynamic model of ICPF (ionic conducting polymer gel film) actuator," in *Proceedings of IEEE International Conference on Robotics and Automation*, Minneapolis, MN, USA, 1996: IEEE.

[41] R. Kanno, S. Tadokoro, T. Takamori, M. Hattori, and K. Oguro, "Modeling of ICPF (ionic conducting polymer film) actuator-modeling of electrical characteristics," in *Proceedings of IECON '95 - 21st Annual Conference on IEEE Industrial Electronics*, Orlando, FL, USA, 1995: IEEE.

[42] P. G. d. Gennes, K. Okumura, M. Shahinpoor, and K. J. Kim, "Mechanoelectric effects in ionic gels," *Europhysics Letters*, vol. 50, no. 4, pp. 513-518, 2000.

[43] S. Tadokoro, S. Yamagami, T. Takamori, and K. Oguro, "Modeling of Nafion-Pt composite actuators (ICPF) by ionic motion," in *Smart Structures and Materials 2000: Electroactive Polymer Actuators and Devices (EAPAD)*, Newport Beach, CA, USA, 2000: SPIE.

[44] S. Nemat-Nasser and J. Y. Li, "Electromechanical response of ionic polymer-metal composites," *Journal of Applied Physics*, vol. 87, no. 7, pp. 3321-3331, 2000.

[45] S. Nemat-Nasser, "Micromechanics of actuation of ionic polymer-metal composites," *Journal of Applied Physics*, vol. 92, no. 5, pp. 2899-2915, 2002.

[46] K. Farinholt and D. J. Leo, "Modeling of electromechanical charge sensing in ionic polymer transducers," *Mechanics of Materials,* vol. 36, no. 5-6, pp. 421-433, 2004.

[47] Z. Chen, X. Tan, A. Will, and C. Ziel, "A dynamic model for ionic polymer–metal composite sensors," *Smart Materials and Structures,* vol. 16, no. 4, p. 1477, 2007.

[48] A. Badri and P. Pouladsaz, "Highly selective and sensitive thiocyanate PVC membrane electrodes based on modified Zeolite ZSM-5," *International Journal of Electrochemical Science,* vol. 6, pp. 3178-3195, 2011.

[49] S. Downes, A. Knott, and I. Robinson, "Towards a shock tube method for the dynamic calibration of pressure sensors," *Philosophical Transactions of The Royal Society A Mathematical Physical and Engineering Sciences,* vol. 372, p. 20130299, 2014.

[50] F. Gao and L. M. Weiland, "Ionic polymer transducers in sensing: Implications of the streaming potential hypothesis for varied electrode architecture and loading rate," *Journal of Applied Physics,* vol. 108, p. 034910, 2010.

[51] F. Gao and L. M. Weiland, "Streaming potential hypothesis for ionic polymer transducers in sensing: roles of ionomer state and morphology," *Journal of Intelligent Material Systems and Structures,* vol. 22, no. 14, pp. 1623-1630, 2010.

[52] F. H. v. d. Heyden, D. Stein, and C. Dekker, "Streaming currents in a single nanofluidic channel," *Physical Review Letters,* vol. 95, no. 11, p. 116104, 2005.

[53] L. M. Weiland and B. Akle, "Ionic polymer transducers in sensing: the streaming potential hypothesis," *Smart Structures and Systems,* vol. 6, pp. 211-223, 2010.

[54] W. Q. Liu, Z. H. Fenga, R. B. Liu, and J. Zhang, "The influence of preamplifiers on the piezoelectric sensor's dynamic property," *Review of Scientific Instruments,* vol. 78, no. 12, p. 125107, 2007.

[55] B. J. Akle, M. D. Bennett, D. J. Leo, K. B. Wiles, and J. E. McGrath, "Direct assembly process: a novel fabrication technique for large strain ionic polymer transducers," *Journal of Materials Science,* vol. 42, no. 16, pp. 7031-7041, 2007.

[56] M. D. Bennett and D. J. Leo, "Ionic liquids as stable solvents for ionic polymer transducers," *Sensors and Actuators A: Physical,* vol. 115, no. 1, pp. 79-90, 2004.

[57] R. Liang and Q.-M. Wang, "High sensitivity piezoelectric sensors using flexible PZT thick-film for shock tube pressure testing," *Sensors and Actuators A: Physical,* vol. 235, pp. 317-327, 2015.

[58] M. Gudarzi, P. Smolinski, and Q.-M. Wang, "Bending mode ionic polymer-metal composite (IPMC) pressure sensors," *Measurement,* vol. 103, pp. 250-257, 2017.

[59] M. Gudarzi, P. Smolinski, and Q.-M. Wang, "Compression and shear mode ionic polymer-metal composite (IPMC) pressure sensors," *Sensors and Actuators A: Physical,* vol. 260, pp. 99-111, 2017.

[60] M. Shahinpoor and K. J. Kim, "Ionic polymer–metal composites: I. Fundamentals," *Smart Materials and Structures,* vol. 10, no. 4, pp. 819-833, 2001.

[61] A. Punning, M. Kruusmaa, and A. Aabloo, "Surface resistance experiments with IPMC sensors and actuators," *Sensors and Actuators A: Physical,* vol. 133, no. 1, pp. 200-209, 2007.

[62] H.-j. Ding, X.-y. Lee, and W.-q. Chen, "Analytical solutions for a uniformly loaded circular plate with clamped edges," *Journal of Zhejiang University-SCIENCE A,* vol. 6, no. 10, pp. 1163–1168, 2005.

[63] G. F. Franklin, J. D. Powell, and A. Emami-Naeini, *Feedback Control of Dynamic Systems*. Upper Saddle River, NJ: Pearson Education, 2006.

[64] F. Durbin, "Numerical inversion of Laplace transforms: an effective improvement of Dubner and Abate's method," *Computer Journal,* vol. 17, pp. 371–376, 1973.

[65] S. C. Fan, S. M. Li, and G. Y. Yu, "Dynamic fluid-structure interaction analysis using boundary finite element method–Finite element method," *Journal of Applied Mechanics,* vol. 72, no. 4, pp. 591-598, 2004.

[66] S. M. Hasheminejad and M. Gudarzi, "Active sound radiation control of a submerged piezocomposite hollow sphere," *Journal of Intelligent Material Systems and Structures,* vol. 26, no. 15, pp. 2073-2091, 2015.

[67] M. Gudarzi, P. Smolinski, and Q.-M. Wang, "Modeling and fabrication of humidity insensitive ionic polymer-metal composite pressure sensors," in *Proceedings of the ASME 2017 Conference on Smart Materials, Adaptive Structures and Intelligent Systems (SMASIS2017),* Snowbird, UT, USA, 2017: ASME.

[68] M. Gudarzi, P. Smolinski, and Q.-M. Wang, "Experimental characterization of the diluent effect on highly-flexible IPMC dynamic pressure sensors," in *Proceedings of the ASME 2017 Conference on Smart Materials, Adaptive Structures and Intelligent Systems (SMASIS2017),* Snowbird, UT, USA, 2017: ASME.

[69] A. M. Tan, F. K. Fuss, Y. Weizman, Y. Woudstra, and O. Troynikov, "Design of low cost smart insole for real time measurement of plantar pressure," *Procedia Technology,* vol. 20, pp. 117-122, 2015.

[70] J. A. Ramirez-Bautista, J. A. Huerta-Ruelas, S. L. Chaparro-Cárdenas, and A. Hernández-Zavala, "A Review in Detection and Monitoring Gait Disorders Using In-Shoe Plantar Measurement Systems," *IEEE Reviews in Biomedical Engineering,* vol. 10, pp. 299-309, 2017.

[71] H. Zamanian, "Toward Creating Normal Ankle Joint Behavior for Drop Foot Patients Using an Ankle Foot Orthosis (AFO) with Superplastic NiTi Springs," Diss. University of Toledo, Toledo2017.

[72] A. Amerinatanzi, H. Zamanian, N. S. Moghaddam, A. Jahadakbar, and M. Elahinia, "Application of the Superelastic NiTi Spring in Ankle Foot Orthosis (AFO) to Create Normal Ankle Joint Behavior," *Bioengineering*, vol. 4, no. 4, p. 95, 2017.

[73] H. Zamanian, "Application of Superplastic Materials in Ankle Foot Orthosis," *JSM Foot & Ankle*, vol. 3, no. 1, p. 1045, 2018.

[74] B. Horsak *et al.*, "A wireless instrumented insole device for real-time sonification of gait," in *21st International Conference on Auditory Display (ICAD 2015)*, Graz, Styria, Austria, 2015, pp. 94-101: ICAD.

[75] J. Park, Y. Na, G. Gu, and J. Kim, "Flexible insole ground reaction force measurement shoes for jumping and running," in *6th IEEE International Conference on Biomedical Robotics and Biomechatronics (BioRob)*, Singapore, Singapore, 2016: IEEE.

[76] F. Pineda-Lopez, A. Guerra, E. Montes, and D. S. Benitez, "A Low Cost Baropodometric System for Children's Postural and Gait Analysis," in *IEEE Colombian Conference on Communications and Computing (COLCOM)*, Cartagena, Colombia, 2016, pp. 1-4: IEEE.

[77] J. Pauk, K. Daunoraviciene, M. Ihnatouski, J. Griskevicius, and J. V. Raso, "Analysis of the plantar pressure distribution in children with foot deformities," *Acta of Bioengineering and Biomechanics*, vol. 12, no. 1, pp. 29-34, 2010.

[78] J. Torres, A. García, C. Villarraga, A. Egel, and R. Polanía, "Desarrollo de un Sistema Electrónico para Medir Ambulatoriamente Presiones en la Planta del Pie Insensible," in *Proc. Iberoamerican Workshop IBERCHIP*, 2007, pp. 1-4.

[79] I. González, J. Fontecha, R. Hervás, and J. Bravo, "An ambulatory system for gait monitoring based on wireless sensorized insoles," *Sensors*, vol. 15, no. 7, pp. 16589-16613, 2015.

[80] L. Shu *et al.*, "Monitoring diabetic patients by novel intelligent footwear system," in *International Conference on Computerized Healthcare (ICCH)*, Hong Kong, China, 2012: IEEE.

[81] K. Kong, J. Bae, and M. Tomizuka, "Detection of abnormalities in a human gait using smart shoes," in *Sensors and Smart Structures Technologies for Civil, Mechanical, and Aerospace Systems*, 2008, p. 69322G: SPIE.

[82] J. H. Bauman and P. W. Brand, "Measurement of pressure between foot and shoe," *The Lancet*, vol. 281, no. 7282, pp. 629-632, 1963.

[83] A. H. A. Razak, A. Zayegh, R. K. Begg, and Y. Wahab, "Foot plantar pressure measurement system: A review," *Sensors,* vol. 12, no. 7, pp. 9884-9912, 2012.

[84] C. Lou *et al.*, "A Graphene-Based Flexible Pressure Sensor with Applications to Plantar Pressure Measurement and Gait Analysis," *Materials,* vol. 10, no. 9, p. 1068, 2017.

[85] Y.-K. Fuh, S.-C. Li, and C.-Y. Chen, "Piezoelectrically and triboelectrically hybridized self-powered sensor with applications to smart window and human motion detection," *APL Materials,* vol. 5, p. 074202, 2017.

[86] B. Zhu *et al.*, "Microstructured graphene arrays for highly sensitive flexible tactile sensors," *Small,* vol. 10, no. 18, pp. 3625-3631, 2014.

[87] M. Gudarzi, P. Smolinski, and Q.-M. Wang, "Application of soft IPMC sensors in real-time foot pressure mapping and gait analysis," in *Proceedings of the ASME's International Mechanical Engineering Congress and Exposition (IMECE2018)*, Pittsburgh, PA, USA, 2018: ASME.

[88] W. Zeng, L. Shu, Q. Li, S. Chen, F. Wang, and X. M. Tao, "Fiber-based wearable electronics: a review of materials, fabrication, devices, and applications," *Advanced Materials,* vol. 26, no. 31, pp. 5310-5336, 2014.

[89] C. Pang *et al.*, "A flexible and highly sensitive strain-gauge sensor using reversible interlocking of nanofibers," *Nature Materials,* vol. 11, no. 9, pp. 795-801, 2012.

[90] S. Jung, J. Lee, T. Hyeon, M. Lee, and D. H. Kim, "Fabric-based integrated energy devices for wearable activity monitors," *Advanced Materials,* vol. 26, no. 36, pp. 6329-6334, 2014.

[91] S. Gong *et al.*, "A wearable and highly sensitive pressure sensor with ultrathin gold nanowires," *Nature Communications,* vol. 5, p. 3132, 2014.

[92] C. M. Boutry, A. Nguyen, Q. O. Lawal, A. Chortos, S. Rondeau-Gagné, and Z. Bao, "A sensitive and biodegradable pressure sensor array for cardiovascular monitoring," *Advanced Materials,* vol. 27, no. 43, pp. 6954-6961, 2015.

[93] S. Y. Kim, S. Park, H. W. Park, D. H. Park, Y. Jeong, and D. H. Kim, "Highly Sensitive and Multimodal All-Carbon Skin Sensors Capable of Simultaneously Detecting Tactile and Biological Stimuli," *Advanced Materials,* vol. 27, no. 28, pp. 4178-4185, 2015.

[94] X. Liao *et al.*, "Flexible and highly sensitive strain sensors fabricated by pencil drawn for wearable monitor," *Advanced Functional Materials,* vol. 25, no. 16, pp. 2395-2401, 2015.

[95] M. L. Muiesan *et al.*, "Central blood pressure assessment using 24-hour brachial pulse wave analysis," *Journal of Vascular Diagnostics and Interventions,* vol. 2, no. 141, p. e8, 2014.

[96] G. Z. Voyiadjis and P. I. Kattan, "On the theory of elastic undamageable materials," *Journal of Engineering Materials and Technology*, vol. 135, no. 2, p. 021002, 2013.